Methods to Improve the Efficiency of Hydrostatic Transmissions in Wind Turbines

A Thesis
SUBMITTED TO THE FACULTY OF THE
UNIVERSITY OF MINNESOTA
BY

Daniel Escobar-Naranjo

IN PARTIAL FULFILLMENT OF THE REQUIREMENTS
FOR THE DEGREE OF
DOCTOR OF PHILOSOPHY

Professor Kim A. Stelson

December 2022

© Daniel Escobar-Naranjo 2022
ALL RIGHTS RESERVED

Acknowledgments

I want to start by thanking my family. They encouraged me to go through this challenging but fulfilling journey that is a Ph.D. My wife Catalina has been my biggest support throughout every event and gave us our biggest motivation: our daughter Olivia. My parents never stopped believing in me and always supported my education, even though it meant having to be away from them. My siblings inspired me to become better at everything I do, regardless of my choice.

I am incredibly thankful to my adviser Prof. Stelson. His guidance through failures and successes was always more than I expected from an academic adviser. He always encouraged me to follow my teaching career and helped me throughout the Ph.D. to become better at it. His technical knowledge was always of great help without discouraging my curiosity.

I am very thankful to Dr. Biswaranjan Mohanty. He became a “co-adviser” for my Ph.D. work. Without his input, long discussions, and fantastic test stand, my Ph.D. would have been much more complicated to complete than it already was.

I am incredibly thankful to my friend Ankit Saini, who has been there, struggling, celebrating, and accompanying me throughout the process.

I am also thankful to all the other graduate and undergraduate students who worked with me in the lab, Eric, John, Yuhao, Neil, Mark, Justin, Yingkun, Luuk, and many others; thanks for your input and constant inspiring curiosity throughout the years.

Dedication

This thesis is dedicated to my Family!

Esta tesis está dedicada a mi Familia!

Abstract

Our research group has previously proposed using Hydrostatic Transmissions (HST) for wind turbines. The results have been encouraging, but the system's efficiency has always been a concern compared to a conventional gearbox. This work aims to approach the problem through three different formulations, including blade pitch oscillations, HST wind turbine control using Extremum Seeking Control (ESC), and dynamic temperature control to optimize the efficiency of the HST.

The first approach involves oscillating the blades of the turbine to increase the lift coefficient and, in turn, improve power capture. A series of CFD simulations and optimizations were performed on a simplified blade model to evaluate if this is beneficial for power capture in horizontal-axis wind turbines. The results show that the optimal conditions are the same as the static blade conditions. These results happen because the drag coefficient rises exponentially as the lift coefficient rises. Also, there is a power loss due to the power required to oscillate the three blades.

The second approach involves using extremum seeking control (ESC) to continuously adapt the torque gain in a modified $k\omega^2$ control law. The k gain is a constant value that highly depends on wind turbine parameters, the C_p vs. λ curve, and uncertain wind conditions. The turbine will not operate under optimal conditions if these parameters change over time. Adapting k by using ESC allows for optimal operation under any conditions. For the conditions considered, simulations and experiments showed that ESC improves power capture by 2.8% to 12.3%.

The third approach involves controlling the temperature of the hydraulic oil to optimize the viscosity, which improves efficiency. A simplified model based on the friction and leakage losses of a hydraulic pump and a hydraulic motor is used to find the optimum operating point. Two control strategies are evaluated through simulations, classic proportional plus integral control (PI) and Sliding Mode Control (SMC). SMC is chosen due to its quick and robust response and low computational needs. Experimental validations showed that this approach leads to a 0.8% to 0.9% efficiency improvement compared to constant temperature control, although the improvement depends on operating conditions.

Overall, these three approaches show potential for improving the efficiency of HSTs in wind turbines, with the second and third approaches showing the most promise. However, further research and experimentation will be needed to fully understand and optimize the use of HSTs in wind turbines.

Table of Contents

List of Tables

List of Figures

Chapter 1

Introduction & Motivation

The earth is undergoing an unprecedented climate crisis. Burning fossil fuels is destroying the planet, but there is hope in renewable energy sources. Wind energy and solar are the fastest-growing energy sources across the world. As climate changes and irreversible environmental damage rises, wind energy is seen as a clean alternative to greenhouse gas-emitting fossil fuels. It currently accounts for 6.3% of U.S. energy production and 5% worldwide [1]. Wind energy will continue to grow significantly in the next decade. The Department of Energy (DOE) had set the goal for wind energy to comprise 10% of domestic power production by 2020, 20% by 2030, and 35% by 2050 [2]. Although we failed the goal for 2020, we are confident that we will significantly exceed the goal for 2030 and achieve the goal for 2050 because of the exponential growth trend of wind power production, Figure 1.

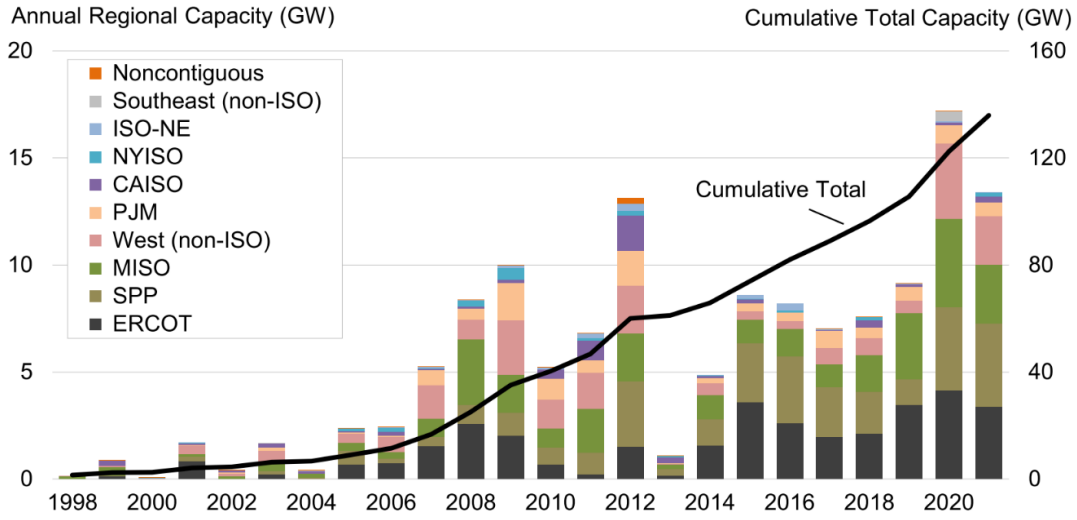

Figure 1: Annual and cumulative growth in U.S. wind power capacity [3]

There are many challenges associated with wind energy production; a major one is its energy efficiency. Most wind turbines capture roughly 0.35 to 0.45 of the energy in the wind, a ratio known as the power coefficient, C_p. A well-known theory developed in 1919 by Albert Betz [4], [5] sets the theoretical maximum limit of C_p as 0.593, [6]. Our wind turbine research aims to reduce wind turbine losses and raise efficiencies to be as high as possible by implementing hydraulic systems and intelligent controls. Increasing the efficiency of wind turbines will reduce the overall cost of wind energy and further expand its implementation worldwide.

1.1. Hydrostatic Transmissions as a Solution for Midsize Wind Turbines

This research is focused on the distributed wind market, which includes midsize wind turbines (100 kW to 1 MW).

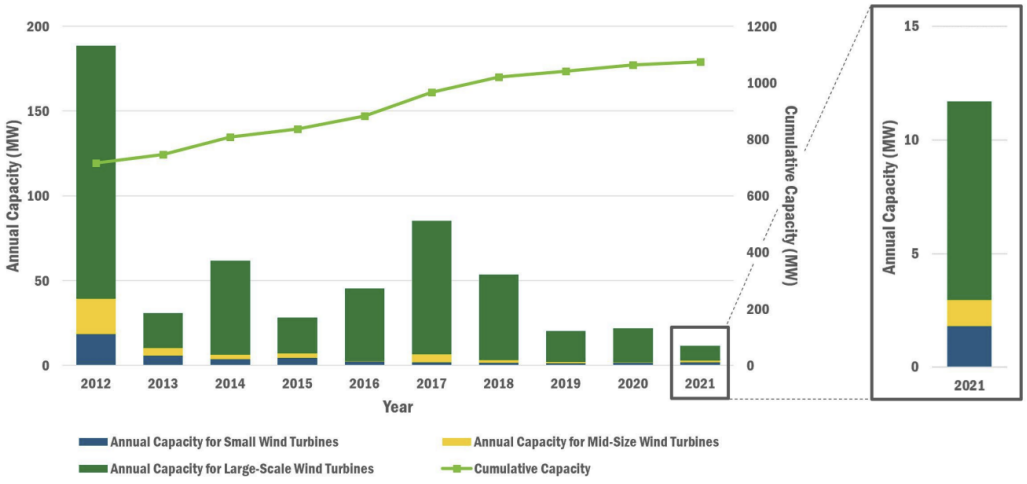

Figure 2: U.S. distributed wind capacity [7]

The distributed wind market is underrepresented, and has declined in the last decade, especially for midsize turbines, Figure 2. However, the Distributed Wind Energy

Association (DWEA) recently stated that the distributed wind market of all sizes has potential comparable to offshore wind, with an economic potential in the U.S. alone of $1400\ GW$, before the new legislation, which is a $6 trillion market potential.

Wind turbines require cost-effective, high-power density, and reliable drivetrains that operate efficiently. Hydraulic drivetrains are an attractive option to achieve these conditions. Industry and academia have proposed hydrostatic transmissions (HSTs) for wind turbines. HSTs use fluid flow to transmit power. A fixed amount of fluid is delivered for each revolution of a positive displacement pump. Similarly, for each revolution of a motor, there is a fixed amount of fluid received. Continuously variable transmission can be achieved by varying the displacement of the pump or motor. For wind turbines, HSTs work as speed-up transmissions, where the pump's displacement must be bigger than the motor's displacement. An example of a variable displacement HST architecture, can be seen in Figure 3.

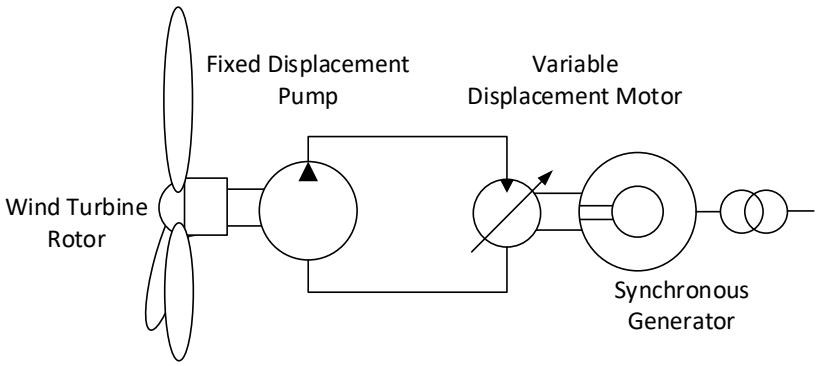

Figure 3: Schematic of an example hydrostatic transmission for wind turbine applications

HSTs are a reliable, proven technology extensively used for demanding duty cycles in mining, fishing, forestry, construction, and agriculture. HSTs are an attractive option for midsize wind turbines because there are commercially available components in the same

power range ($100\ kW\ –\ 1\ MW$). These turbines can operate in local niches, eliminating the need for costly electric power transmission upgrades. Also, distributed wind makes the power grid more stable and reliable. A disadvantage of conventional gearbox turbines is that they intentionally limit energy extraction above the rated wind speed [8]. An advantage of HSTs, for example, is that they can enable hybridization by storing energy in an accumulator when the wind power is above rated power and releasing it when it drops below rated power.

It is well-known that the efficiency of gearbox transmissions is higher than the efficiency of HSTs, making HSTs unattractive at first sight. However, when comparing the total wind turbine efficiency, it can be shown that they are comparable. This similarity is achievable mainly due to the variable speed capabilities of the HST and the power-to-weight ratio that can be achieved by using hydraulics to transmit the power. The research question is how to improve the turbine's efficiency using smart controls and more efficient HSTs.

The standard way to assess if these systems are improving is to evaluate the Levelized Cost of Electricity (LCOE) [9]. The LCOE measures the lifetime costs of the system divided by energy production. This allows different technologies (e.g., wind, solar, natural gas) of unequal life spans, project size, capital cost, risks, return, and capacities to be compared under realistic conditions. If the LCOE is lower, the system is more desirable and more likely to be implemented. Using smart control strategies is essential for improving midsize wind turbines. Implementing new control strategies does not require a large capital investment, and it helps improve energy production, reducing the LCOE of the system.

In [10], Sheng and Stelson present a study showing a comparison between a gearbox wind turbine and two configurations of HST wind turbines. The main conclusion is that the LCOE is higher for HST wind turbines because the hydraulic components cost around $\$8/kg$ while the gearbox costs around $\$1/kg$. If the price per kilogram of the hydraulic components does not decrease, they will not be competitive with gearbox designs.

1.1.1. Wind Turbine Controls

A wind turbine has four control regions, Figure 4. Region 1 is where the wind speed is below the turbine's cut-in speed, and the turbine is in standby mode. Region 2 is where the wind speed varies between the cut-in and rated speeds. Here, the turbine is controlled to maximize the power. Region 3 is where the wind speed is above the rated speed but below the cut-out speed. Here, the turbine is regulated to limit the power. Region 4 is where the wind speed is above the cut-out speed, and the turbine is shut down to avoid damage.

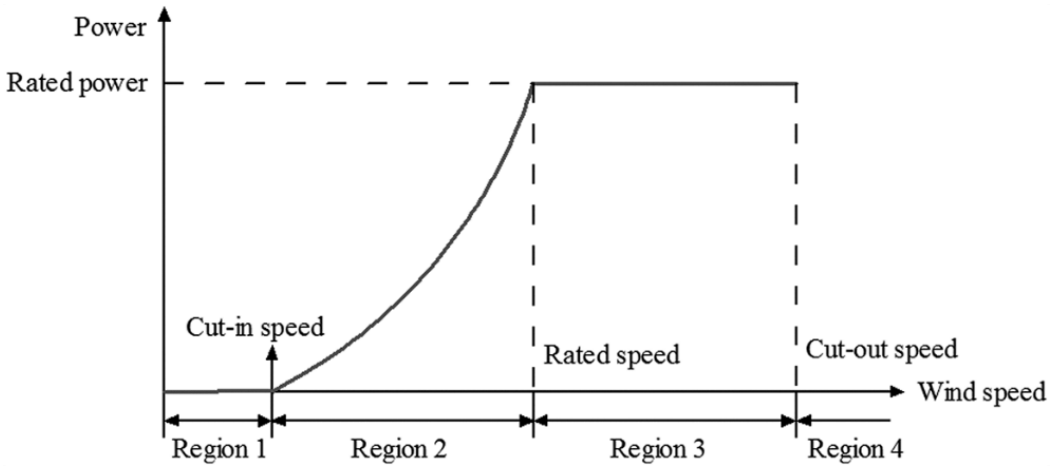

Figure 4: Control regions of Horizontal Axis Wind Turbines

For a variable-speed horizontal axis wind turbine (HAWT), the control objective is to maximize power by operating the turbine at the peak of the C_p-TSR-Pitch curve, Figure 5.

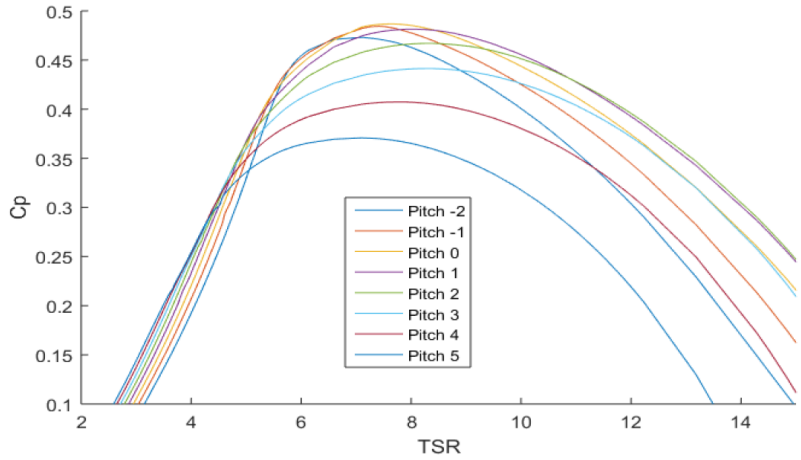

Figure 5: $C_p - TSR - Pitch$ curve for the rotor of a traditional HAWT.

The power coefficient (C_p) of a turbine is defined as the fraction of the power from kinetic energy in the wind captured by the turbine's rotor. It is a function of blade pitch angle (β) and TSR (λ), equation (1).

$$C_p = \frac{P_r}{P_w} = C_p(\lambda, \beta) \tag{1}$$

The power in the wind P_w is:

$$P_w = \frac{1}{2} A \rho U^3 \tag{2}$$

Where P_w is the power in the wind, A is the blade-swept area, and U is the wind speed.

Figure 5 shows the curve of the simulated rotor power coefficient as a function of λ and β for NREL's Controls Advanced Research Turbine (CART).

The well-known $k\omega^2$ control law, equation (3), takes the turbine to maximum power operation point in steady-state by varying the torque of the generator [8].

$$\tau = k\omega^2 \tag{3}$$

However, this law only performs well under slowly varying wind conditions, and relies on accurately knowing the torque control gain, k, equation (4),

$$k = 0.5\rho\pi R^5 \frac{C_{pmax}}{\lambda_*^3} \tag{4}$$

Where ρ is the air density, R is the radius of the blade, and λ_* is the optimum TSR at which the maximum power coefficient C_{pmax} occurs, Figure 6. A graphical representation of C_p as a function of TSR at a specific pitch angle is shown in Figure 6 [11]. λ and C_p vary with wind velocity. From Figure 6 it is evident that C_p is maximum at around $\lambda = 8$ (optimum operating point, λ_*). To maximize the amount of power being captured by the turbine, it should always operate at the maximum possible C_p value.

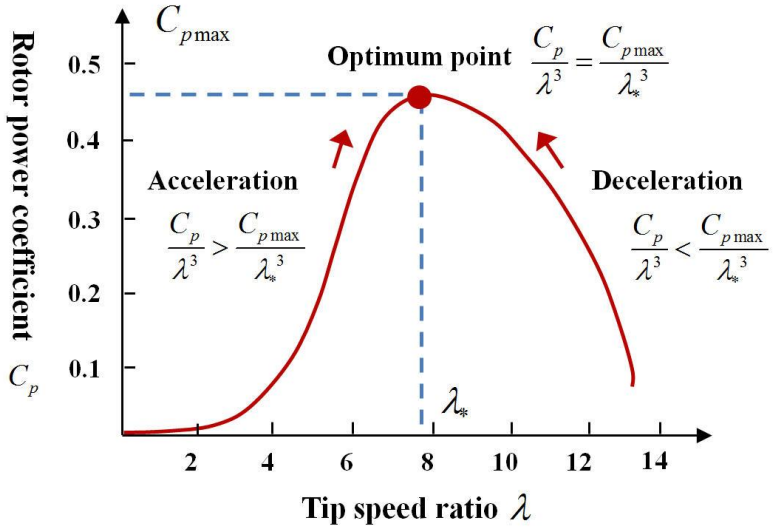

Figure 6: C_p as a function of λ. λ_* is shown where C_p is max.

Simulations of a turbine operating under unsteady wind show that it does not stay at the optimal operation point when using this control strategy, for two reasons. First, fast and continuous changes in wind speed combined with the large inertia of the blade prevent fast reactions on the rotor. Second, torque control is based on rotor speed, not on actual wind speed, delaying the response.

Most research approaches for improving power capture of wind turbines consist of maximum power point tracking (MPPT) in region 2. MPPT is achieved by controlling the rotor torque or the rotor speed. Multiple approaches have been proposed and are summarized in [8], [12] and [13]. These approaches are exclusive to traditional fixed-gearbox turbine transmissions, opening opportunities to investigate the hydraulic transmissions' performance for wind turbines.

1.1.2. Wind Turbine Controls with an HST

In an HST, the rotor torque is controlled using a command pressure, p_c, as shown in equation (5).

$$p_c = \frac{\tau_c \eta_{mp} 2\pi}{D_p} \tag{5}$$

where η_{mp} is the mechanical efficiency of the pump and D_p is the displacement of the pump. This control pressure is used to control the HST pressure by changing the swash plate angle of the motor, Figure 7.

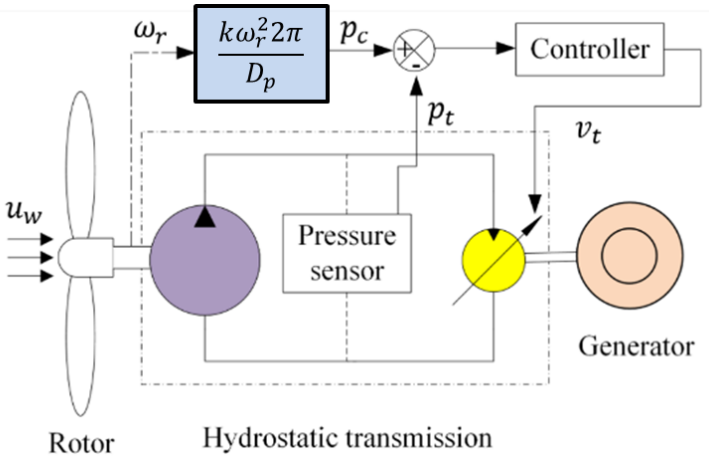

Figure 7: HST control schematic. Figure modified from [14]

This thesis presents three strategies to improve hydrostatic transmission efficiency in wind turbines. Before introducing them, a short review of the work on HST wind turbines is presented.

1.2. Industrial and Academic Applications

Industry and academia have made efforts to establish HSTs as viable replacements for wind turbine gearboxes. A full review of all the systems that have been set in place until 2020 can be found in [15]. The following are notable examples.

1.2.1. Industrial Research and Development

In 2007 Kovach et al. [16] from Parker Hannifin patented the idea of using a fixed ratio HST, power electronics, and an induction generator in a wind turbine. The same year Chapple et al. [17] from ChapDrive patented a continuously variable HST with a fixed displacement pump, a variable displacement motor, and a synchronous generator. In 2011, in Germany, Meuser et al. [18] patented an HST with a fixed displacement hydraulic pump

connected to a combination of multiple fixed displacement hydraulic motors, a variable displacement hydraulic motor, and a synchronous generator. In 2013 wind industry giant Mitsubishi Heavy Industries [19] field-tested a 7 MW utility-scale HST wind turbine (Sea Angel) using Artemis' Digital Displacement technology, Figure 8.

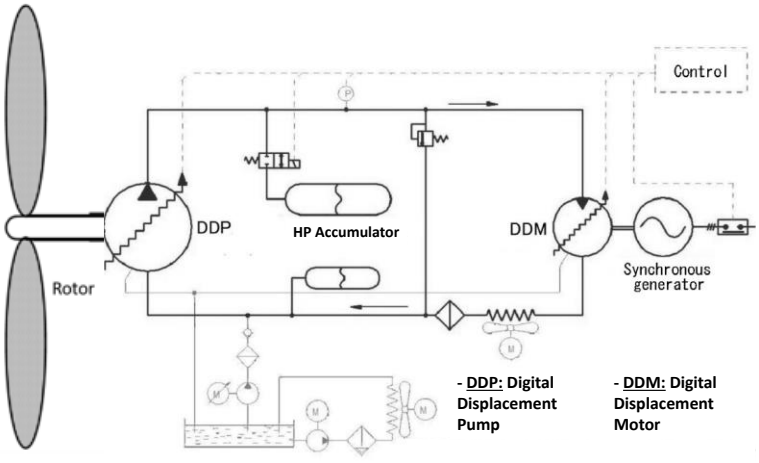

Figure 8: Sea Angel HST configuration. Figure modified from [19]

Commercial efforts have resulted in field demonstrations but not commercialization. These field demonstrations help popularize the technology by showing the feasibility and performance of the system. Commercialization delays are mainly due to insufficient commercially available components for utility-scale turbines, so HSTs become an expensive option. For example, Sea Angel, the 7MW prototype turbine, uses Artemis's Digital Displacement pump and motor to improve the overall performance of the HST. This technology is currently being commercialized but is not widely available.

1.2.2. Academic Research and Development

Multiple HST simulations and laboratory experiments have been made in academia. Researchers at RWTH Aachen University, the University of Minnesota, and Lanzhou

University of Technology [20] have worked on wind turbine dynamic models, short-term and long-term energy storage, advanced control strategies, and validations through laboratory experiments shown in Figures 9, 10 and 11.

At RWTH Aachen, Schmitz et al. [21], [22] developed a 1MW HST test stand to test HSTs under wind turbine condtablitions, Figure 9. The main results show that their multiple pumps and motors scheme with a switching control strategy can reach 85% overall efficiency over a wide power range.

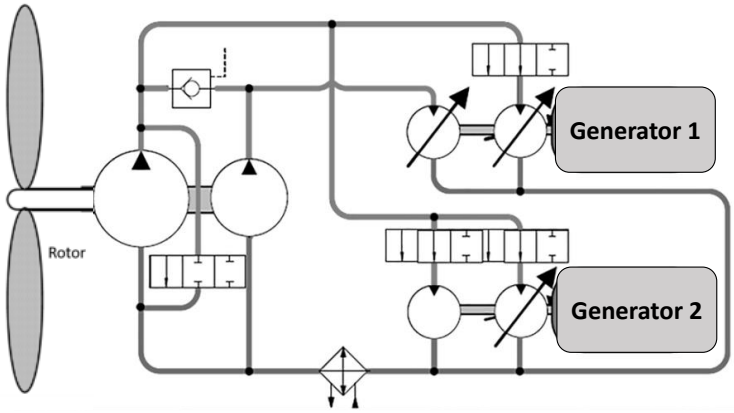

Figure 9: HST wind turbine test stand schematic proposed in [21]. Figure modified from [15]

Mohanty et al. [23] at the University of Minnesota worked on a high-fidelity dynamic model of a power regenerative test stand, Figure 10. The model was used to validate HST wind turbine simulations and showed through simulations that an HST with a fixed displacement pump, a variable displacement motor, and a synchronous generator can fulfill the required grid regulations [24]. The steady-state and transient response of the model is compared and validated with experimental data [14].

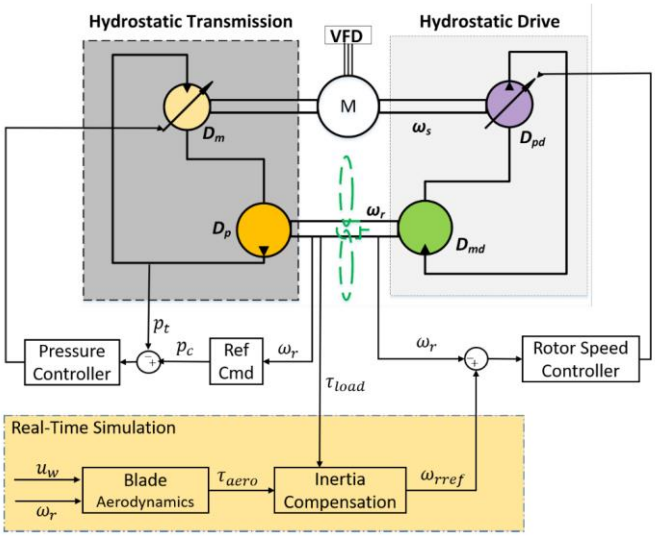

Figure 10: HST wind turbine test stand schematic proposed in [14]

Hybridization has also been studied at the University of Minnesota. Dutta et al. [25] worked on simulations of a midsize hybrid HST wind turbine with a secondary pump coupled to the generator shaft and an accumulator for short-term energy storage. The study shows a 4% energy improvement in conventional HST turbines. It also shows that the optimal accumulator size is 60 L. Mohr et al. worked on simulations [26] and later experimental validations [27] of a midsize hybrid HST wind turbine with a secondary pump coupled to the rotor shaft and a 50 L accumulator for short-term energy storage, Figure 11. Results show a smoother system response but low annual energy production improvement.

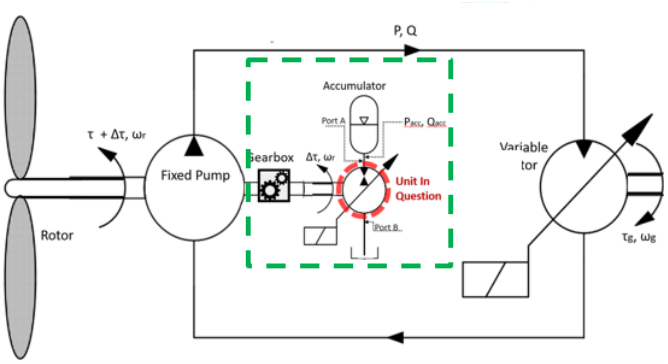

Figure 11: HST system with energy storage proposed in [26]

Advanced control approaches have also shown promise. Wang et al. [28] worked on simulations of Model Predictive Control to improve the power capture of a midsize HST wind turbine. The results showed a faster response than the conventional $k\omega^2$ control for small wind step changes (about 1 m/s). More significant step changes made the system unstable. The author states that these preliminary results need to be re-evaluated with a higher accuracy model to obtain better control gains. Escobar-Naranjo et al. [29], [30] have explored the use of Extremum Seeking Control through simulation and experiments, which will be expanded on as one of the chapters in this thesis.

Wei et al. [20] at Lanzhou University of Technology worked on simulations of a 600 kW hybrid HST wind turbine for long-term energy storage with a 6000 L accumulator. The simulations show the system can overcome wind power's fluctuation and intermittence shortcomings.

1.3. Proposed Research Ideas

This thesis presents three research ideas to improve the efficiency of HSTs in wind turbines:

- The first idea explores blade pitch oscillations through CFD simulations and optimizations to find the best oscillating conditions for energy improvement.
- The second idea explores Extremum Seeking Control to improve the Maximum Power Point Tracking (MPPT) of conventional torque control strategies.
- The third idea explores hydraulic oil temperature control to optimize the viscosity that maximizes the HST's efficiency.

1.3.1. Oscillating Wind Turbine Blades to Improve Wind Turbine Power Capture

The second chapter of this thesis explores the opportunity of oscillating the pitch of the wind turbine blades to increase the lift forces, hence the rotor's torque, to generate more power [31]. Oscillating an airfoil causes a phenomenon of delayed flow separation known as dynamic stall [32], which, under particular conditions (frequency, amplitude, and average angle of attack), can increase the instantaneous maximum lift coefficient by up to 97% [33]. This concept is well described in the literature, especially for load and aeroelastic calculations. Oscillating pitch models were initially developed for helicopter applications and adapted for wind turbine modeling [34]. Holierhoek et al. [35] systematically compared experimental data and three of the most used models on wind turbine airfoils but never explored the opportunity to improve power capture. In this study, we investigated the possibility of using oscillating pitch for wind turbine applications through computational fluid dynamics (CFD) simulations and Blade Element Momentum Theory (BEMT). The chapter will present the tools and methods used to perform the study and later explain the different results obtained through simulations and optimization. Preliminary results of this chapter are published in the proceedings of the Scandinavian International Conference on Fluid Power 2021 [31].

1.3.2. Extremum Seeking Control to Improve Wind Turbine Power Capture

The third chapter of this thesis focuses on using Extremum Seeking Control (ESC) for Maximum Power Point Tracking (MPPT). Conventional turbines use the $k\omega^2$ torque control law in region 2. A pressure control law derived from the $k\omega^2$ law has been designed

and experimentally validated on the power regenerative hydrostatic transmission wind test stand at the University of Minnesota [23]. The performance of the pressure control law strongly depends on the value of the gain k, where the optimal value of k varies over time and cannot be calculated a priori from manufacturer's data or experiments. Extremum Seeking Control (ESC) can overcome these challenges. ESC is a model-free real-time optimization control algorithm used to determine and track the parameters that optimize a system's objective function. The use of ESC is well-suited for wind turbines because of the slowly changing conditions of the system. Since the ESC does not require any hardware additions, any power capture improvements lower the levelized cost of electricity (LCOE). ESC has previously been used to optimize the power capture of gearbox wind turbines by tuning k of the $k\omega^2$ torque control law in region 2. Xiao et al. [36], [37], have proven through simulations and experiments that ESC can improve the performance of conventional gearbox wind turbines by up to 12%. Ghaffari et al. [38] have also implemented ESC for gearbox wind turbines. Their work focuses on improving the transient response by including an inner-loop induction generator controller based on field-oriented control. Their simulations show a more robust response under transient conditions than conventional ESC. Ibrahim et al. [39] have worked with ESC for wind turbines with hydro-mechanical drivetrains. The main difference in their approach is to dither the swash plate angle of the pump in the hydrostatic transmission directly instead of oscillating the torque control gain. Also, their simulations compare their results to those of a fixed-speed wind turbine. Creaby et al. [40] propose a multivariable ESC control strategy for maximizing the energy capture of a conventional gearbox turbine. The main points treated in their simulation study include solutions to practical problems such as windup due to

actuator saturation and slow convergence rate for rapidly changing wind speeds. This chapter studies an extension of ESC to HST wind turbines through simulations and experiments, including a study on the effects of changing the C_p vs. λ curve over time. Preliminary results of this chapter are published in the proceedings of the ASME/BATH 2021 Symposium on Fluid Power and Motion Control and the proceedings of the ASME/BATH 2022 Symposium on Fluid Power and Motion Control [29], [30].

1.3.3. Dynamic Temperature Control to Improve HST Efficiency

The fourth chapter of this thesis focuses on optimizing the efficiency of the HST by optimizing the oil viscosity using temperature control. Significant hydraulic component losses originate from fluid-surface interactions within interfacial gaps. Pressure drops cause leakage through the gaps, and relative motion causes friction across the gaps, both of which contribute to losses. Frictional losses are proportional to viscosity, but leakage is inversely proportional to viscosity resulting in a trade-off between leakage and friction (volumetric and mechanical loss) when choosing the viscosity for hydraulic components. With the pump and motor operating at different speeds, there is an intermediate viscosity that minimizes the transmission's total mechanical and volumetric losses. This viscosity optimization is of great importance since the efficiency of the transmission can be improved without requiring hardware modifications. Only leakage and friction losses are considered in this study, but other sources of hydraulic loss do exist. Cavitation, fluid compression, and commutation have been explored extensively in other works [41], [42]. While these additional losses contribute non-negligible effects on hydraulic component efficiency, for this study, a simple volumetric and mechanical efficiency model is sufficient

to capture the essential trade-off governing viscosity choice in hydraulic components. The first part of the chapter examines the theory and methodology for determining the optimal oil viscosity for an HST used in wind turbine experiments at the University of Minnesota. A simple hydraulic component efficiency model is modified with learned parameters to characterize the viscosity-efficiency curve of the HST. Theoretical predictions are compared to experimental results to verify the viscosity optimization procedure and evaluate the accuracy and limitations of the prediction model. In the second part of the chapter, the model is used to find the optimal viscosity and temperature for multiple operating conditions (wind speeds). The optimal temperature value is then used to control a counterflow heat exchanger that brings the oil to optimal viscosity via different control strategies. Simulation studies using classical PI control and Sliding Mode Control (SMC) are performed to evaluate the performance of the control strategies. The most appropriate one is chosen for experimental testing. The results show less than 1% efficiency improvements for the tested conditions. However, it opens the possibility to study further the capabilities for other wind turbine operating conditions. Also, and probably more interesting, to study dynamic oil temperature control for speed-down HSTs. Preliminary results of this chapter are published in the proceedings of the ASME/BATH 2022 Symposium on Fluid Power and Motion Control [43].

Chapter 2

Oscillating Wind Turbine Blades to Improve Wind Turbine Power Capture

This chapter focuses on oscillating the pitch of wind turbine blades using hydraulic actuation to increase the power capture of hydrostatic transmission wind turbines. This is because oscillating an airfoil under specific conditions increases the instantaneous lift coefficient by up to 97%. Different conditions were investigated by varying airfoil shape, waveform shape, waveform amplitude, waveform frequency, and average angle of attack. The following conditions gave the best performance: a low camber airfoil, a lower average angle of attack than used for a non-oscillating airfoil, and an optimized waveform shape called a “tilted sinusoid.” A multi-level factorial experiment determined the most impactful variables were frequency, amplitude, and average angle of the tilted sinusoid. Numerical simulations and hill climbing optimization studied the best frequencies and amplitudes. Results showed that oscillating the pitch of the wind turbine blades would, under all conditions tested, never outperform steady-state turbine operation, mainly because of the higher drag coefficients also present when oscillating the blade's pitch.

2.1. Materials and Methods

2.1.1. Blade Element Momentum Theory (BEMT)

A turbine blade has an airfoil cross-section with continuously varying chord, orientation, and shape along its length, as shown in Figure 12. The variation from root to mid-span to tip is required so that the blade is strong and efficient. The blade is twisted so that the angle of attack is constant along its length. The product of the chord length and the radius is designed to be constant so that the Reynolds number is constant. For this reason, the chord length decreases with the radius.

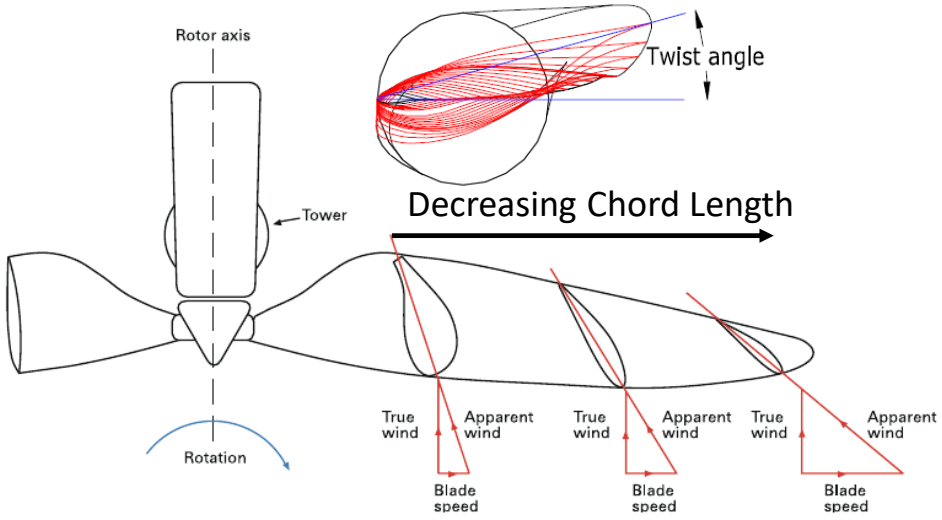

Figure 12: A typical modern horizontal axis wind turbine blade with airfoil profiles, twist and chord length variation[44]

The importance of the aspects mentioned above of wind turbine blade design is that they allow for the characterization of the entire 3D turbine blade from the physics of a single 2D cross-section using BEMT. BEMT is a combination of momentum theory and blade element theory. Momentum theory analyses the momentum balance of the rotating annular stream tube passing through the turbine, Figure 13 [45]. Blade element theory studies the

forces generated by the airfoil's lift and drag forces, Figure 14, at different sections along the length of the blade [46]. Combining both allows us to obtain valuable relationships leading to fast and simple calculations. The method assumes steady wind conditions, no interaction between elements, or wake expansion. Methods to include tip losses, yaw of the turbine, and 3D corrections have been implemented to improve the analytical results [47] but are not included in this work.

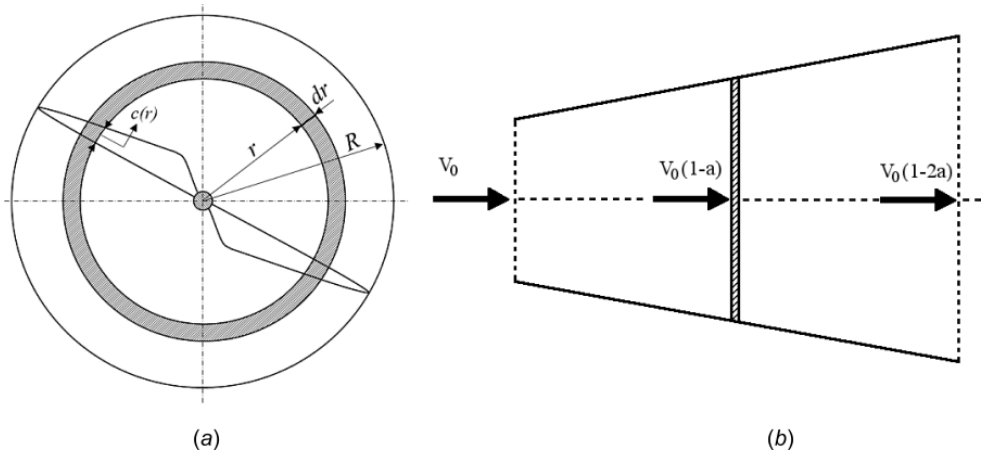

Figure 13: Typical geometry used for BEM theory analysis (a) Actuator disk (b) Fluid stream tube [47]

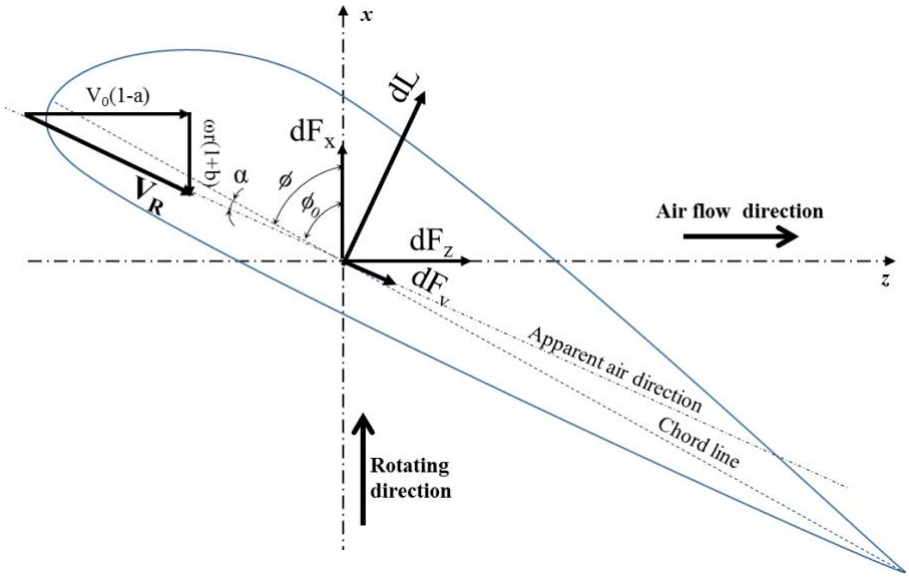

Figure 14: Forces acting on the single-blade element [47]

From BEMT, we can calculate the torque generated by each element of the wind turbine blade using equation (6),

$$dT = \frac{1}{2}\rho B c(r) R(r) V_R^2 (C_L \sin(\phi) - C_D \cos(\phi)) dr \quad (6)$$

Where ρ is the density of the air, B is the number of blades, $c(r)$ is the chord length of the element at a distance, r, from the hub, $R(r)$ is the radius of the blade at a distance, r, from the hub, V_R is the relative velocity of the wind, C_L is the aerodynamic lift coefficient, C_d is the aerodynamic drag coefficient, and ϕ is the angle of relative velocity of the wind with respect to the rotor's axis. The total power generated by the turbine can then be calculated using equation (7),

$$P_r = \int_{R_{hub}}^{R} \omega dT \quad (7)$$

where R_{hub} is the radius of the turbine hub, R is the radius of the blade, and ω is the rotational velocity of the blades.

The power generated by the blades on the rotor is the net power for the static case, equation (8). The net power for the blade oscillation case is the power generated by the oscillating blades minus the power needed to oscillate the blades, P_{osc}, equation (8). To calculate P_{osc} we assume steady-state operation and no friction losses,

$$P_{osc} = \omega_p \tau_{aero} \quad (8)$$

Where ω_p is the rotational velocity of the pitching and τ_{aero} is the torque generated on the blade by the aerodynamic forces and can be calculated by,

$$\tau_{aero} = \frac{1}{2} C_{M_{osc}} \rho V_R^2 c(r)^2 dr \quad (9)$$

and $C_{M_{osc}}$ is the aerodynamic moment coefficient of the oscillating blade. The dynamic power in the rotor is,

$$P_{dyn} = P_r - P_{osc} \tag{10}$$

Considering that C_L and C_D in equation (6) are the coefficients of the oscillating blade. A code that calculates all of these previous equations is given in Appendix a.1.

2.1.2. Variable Selection

To evaluate the performance of the oscillating pitch versus the static pitch, a response variable, the power ratio, P_{ratio}, is introduced. The equation for the power ratio is,

$$P_{ratio} = \frac{P_{dyn}}{P_{sta}} \tag{11}$$

where P_{dyn} is the power captured from the dynamic simulation and P_{sta} is the power captured from the static simulation. Five variables significantly impact the response variable, P_{ratio}. These variables are the airfoil shape, the waveform of oscillation, the average angle of attack, the amplitude, and the frequency. An extensive exploration of the airfoil shape and waveform oscillation was performed before the optimization for the other three variables was conducted.

The airfoil selected for the study is the DU 96-W-180 developed at the Delft University of Technology in the Netherlands, its shape is shown in Figure 15. A low-camber airfoil was selected because it has a high lift-to-drag ratio [48], and its profile data is available online [49]. We also explored high-camber airfoils like the S8XX series from the National Renewable Energy Lab (NREL), and the results showed much lower performances.

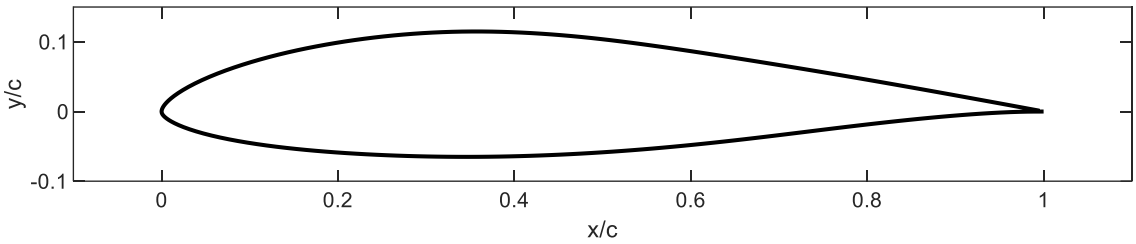

Figure 15: DU 96-W-180 airfoil outline

The waveform selected for the study is a "tilted sinusoid", with an equation of the general form,

$$\alpha = \sum_{k=1}^{n} \frac{\binom{2n}{n-k}}{k2^{2n-1}} \sin(k2\pi ft) \tag{12}$$

where f is the frequency, t is time, and in general $\binom{2n}{n-k}$ is a combination which is defined as,

$$\binom{2n}{n-k} = \frac{(2n)!}{(n-k)!\,(n+k)!} \tag{13}$$

We chose a value of $n = 4$ to obtain the desired tilting, as shown in Figure 16. As $n \to \infty$ the waveform becomes a sawtooth wave.

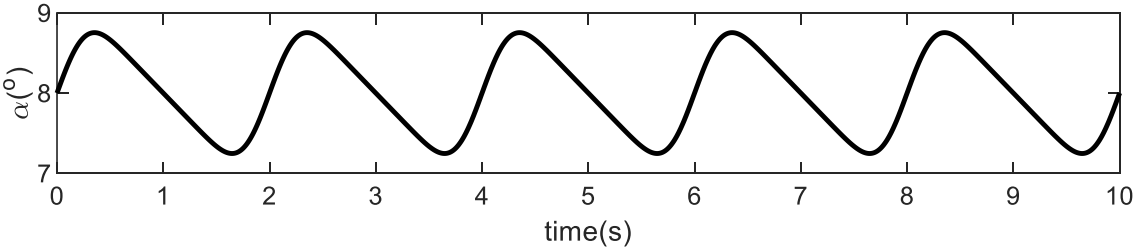

Figure 16: "Tilted sinusoid"

The benefits of a tilted sinusoid oscillation as compared to a regular sinusoid are further described in section 2.2.2 of this thesis.

The three independent variables changed to form the solution space are the average angle of attack, amplitude, and frequency. The average angle of attack is the angle that the airfoil oscillates around. The second free variable is the amplitude of the dynamic pitching. The only constraint on this variable is that the amplitude cannot be larger than the average angle of attack to avoid negative angles of attack during the blade's cycle. Negative angles of attack produce very poor or even negative lifts so they will be avoided. The final free variable is the frequency of the oscillation. The major constraint on this variable is that the maximum rotational speed possible with standard wind turbine actuators is roughly 10 deg/s [50]. One rotational cycle for the airfoil is defined as tilting up to the highest angle, then down to the lowest angle, and then back to its starting angle; therefore, the total angular difference the airfoil travels in one cycle is four times the amplitude. Consequently, the equation for maximum possible frequency, f_{max}, is,

$$f_{max} = \frac{\omega_{max}}{4A} \tag{14}$$

where ω_{max} is the maximum rotational speed of 10 deg/s, and A is the amplitude in degrees. Therefore, the maximum frequency for each simulation case is related to the amplitude of that simulation.

The power ratio values obtained from these simulations are compared to each other to find the pitching settings that produce the highest efficiency. The static blade simulations are performed in QBlade, the dynamic pitching CFD simulations are performed in Ansys Fluent®, and the BEMT calculations are performed in MATLAB®.

2.1.3. CFD Simulations

All the CFD Simulations are run with 2D airfoil cross-sections using the SST k-ω turbulence model, as suggested by Menter [51]. The mesh size is initially 0.002 m for the factorial experiment with refinement around the edge of the airfoil. The mesh size is later enlarged to 0.01 m for the hill climbing optimization to improve the speed of the simulations after validating that the new mesh size produces accurate results. The larger mesh is shown in Figure 17. The mesh is coarse, far away from the airfoil cross-section but refined in the circular region around the airfoil and even further refined at the leading edge. The average angle of attack is then set by rotating the profile in the geometry setup. Then, a user-defined function (UDF) is programmed in C language to simulate the desired oscillatory movements. After loading the UDF into Ansys Fluent®, a 10 s simulation is run. For the factorial experiment, the time step is 0.002 s with 5000 time steps, but this is increased to a time step of 0.01 s with 1000 time steps for the hill climbing optimization for the same reason of reducing simulation time. Ansys Fluent® reports the lift, drag, and pitching moment coefficients in the 2D simulation, which can then be plugged into a series of calculations, including equations (6) and (7), to calculate the overall power generated by the turbine based on BEMT.

Based on the increase of the mesh size and the time step for the hill climbing optimization to save time, a discrepancy of power ratio of around 2% is found for the initial simulations. Despite the slight difference between the two meshes and time steps, this is still a valid method to find the optimal point.

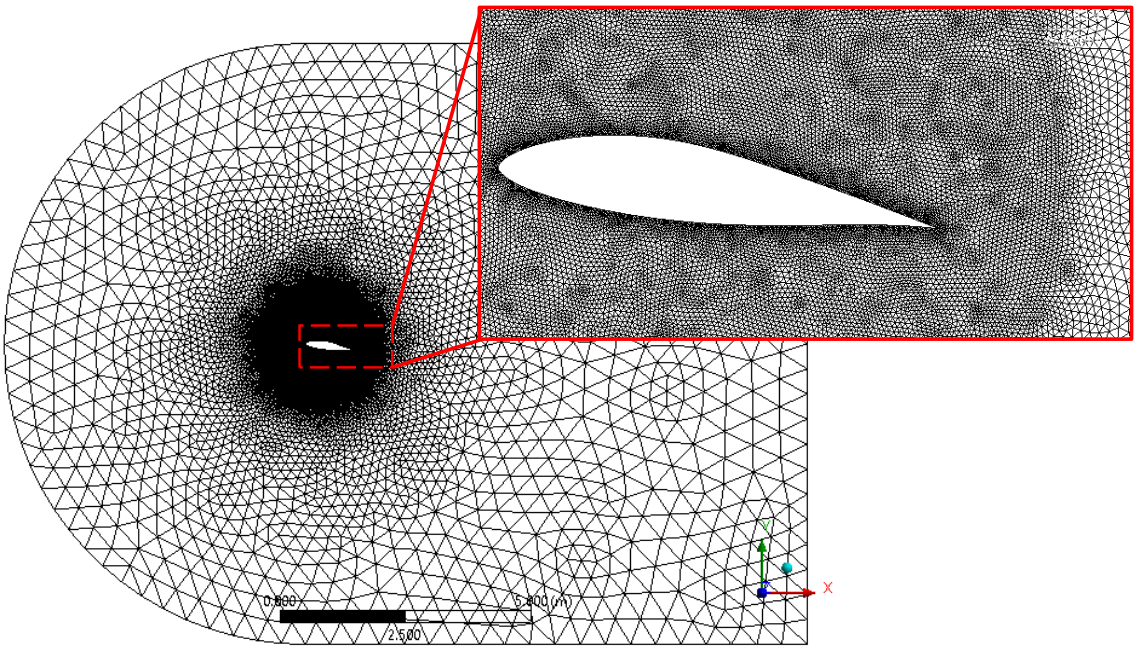

Figure 17: 2D mesh in Ansys Fluent® with detailed view of the mesh around the airfoil

2.1.4. Factorial Experiment

The first portion of the optimization study is based on a factorial experiment. Factorial design is an efficient method for determining the effect of multiple independent variables on a response variable. It involves selecting high and low values for each independent variable to search the solution space and determine the relative effect of each independent variable, or combinations of variables, on the output variable [52]. The only three independent variables that are adjusted are the average angle of attack, the amplitude, and the frequency. High, low, and medium values are selected for each independent variable. These conditions create twenty-seven cases that are run in Ansys Fluent®.

2.1.5. Hill-Climbing Optimization

The second portion of the optimization study is based on a hill-climbing optimization. Hill-climbing optimization is an iterative local search technique. For this final solution space

search, a greedy approach is used. With this approach, the algorithm always moves toward a higher power ratio to find the best solution [53]. Since it is a three-variable optimization, four initial points are required. To find the next prospect point, the centroid of a trapezoid is found, and a new point is projected from the worst point. This new point replaces the worst point from the previous iteration, a new centroid is found, and a new point is projected. This process is iterated until the optimal solution is found. Figure 18 (a), (b), and (c) illustrate the idea for the first three iterations of the optimization. Figure 22 shows the complete optimization path found for this study. A code that performs this optimization is given in Appendix a.2.

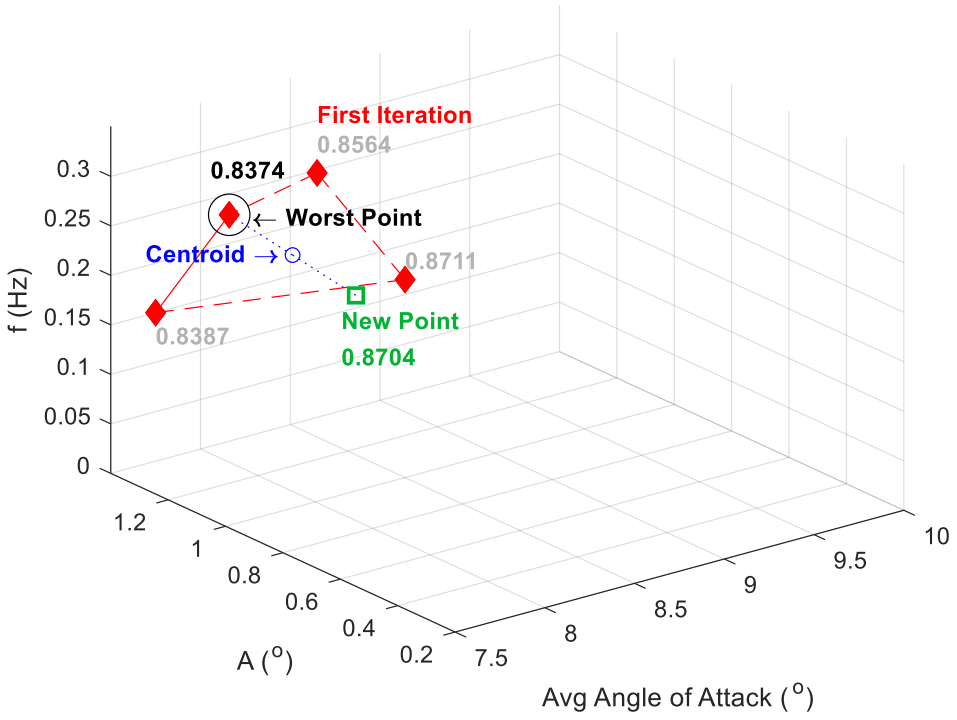

(a)

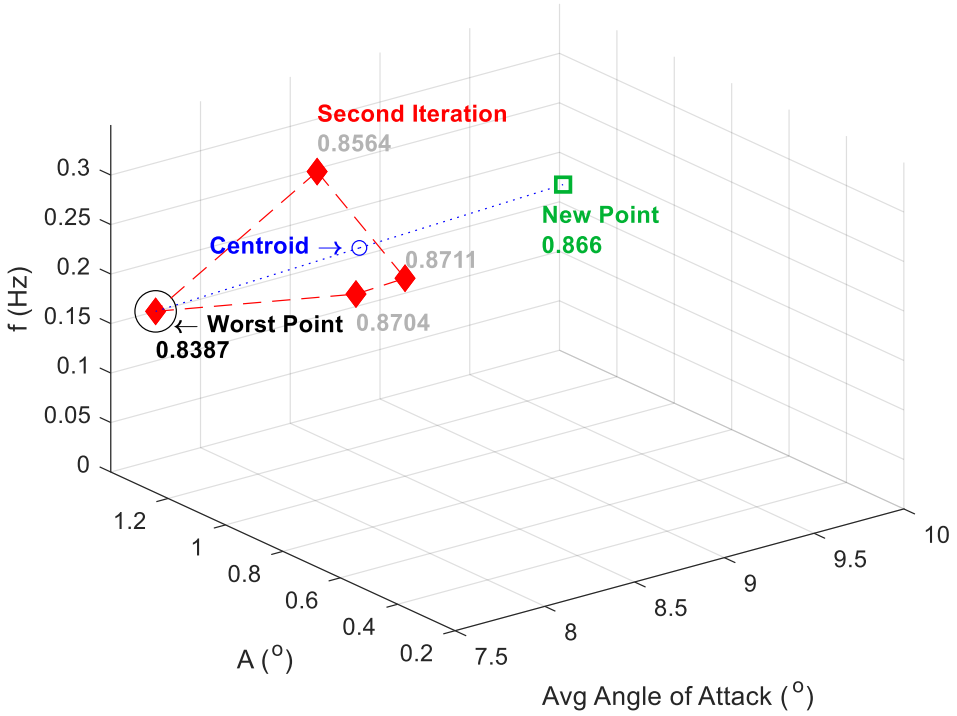

(b)

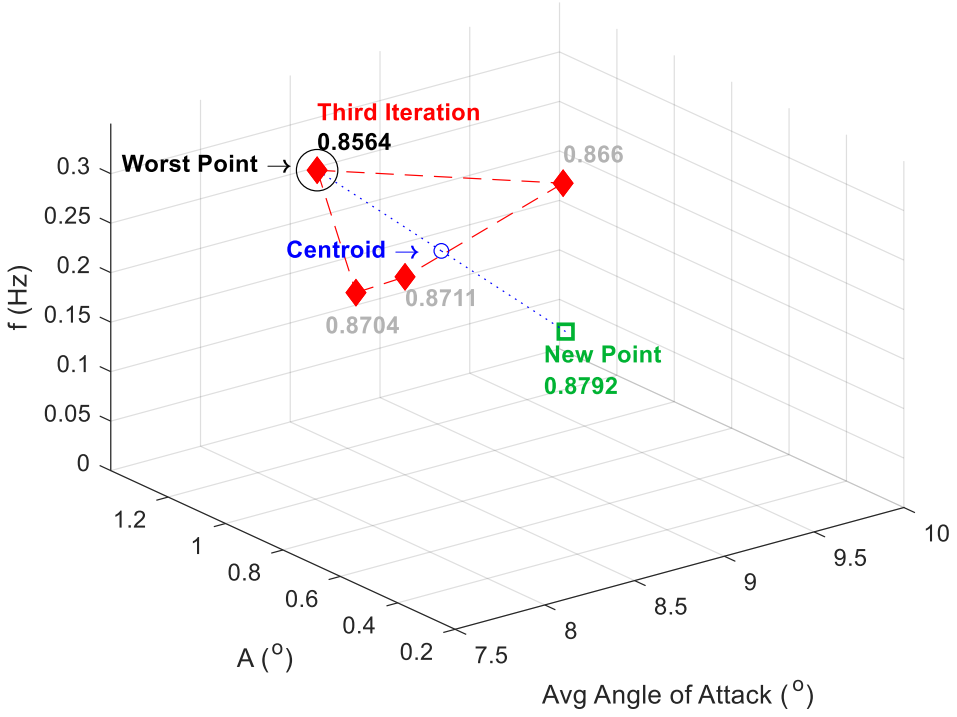

(c)

Figure 18: Step-by-step hill climbing optimization example. The numbers represent the power ratio, P_{ratio}, for the specific average angle of attack, amplitude, and frequency being evaluated.

2.2. Results and Discussion

The results obtained in this work are divided into two. The first results are related to the initial CFD simulations used to evaluate the aerodynamic forces acting on the wind turbine blade. The second results are related to the optimization results obtained through the factorial experiment and the hill climbing optimization to find the best oscillation conditions.

2.2.1. CFD Simulations

We explored the effect of the angle of attack on the lift and drag of airfoils; this information allowed for an educated choice of the solution space to search in the optimization process. Experimental [33] and CFD simulation data of the lift and drag coefficients are shown in Figure 19. Figure 19 (a) shows that the static CFD case, the purple line, exhibits a maximum lift coefficient around an angle of attack of 15°. Still, in Figure 19 (b), it is clear that the drag can be orders of magnitude larger at this point than it is at low angles of attack. Both the experimental and simulation data on these plots suggest that the optimal combination of lift and drag will probably be found roughly between 5° and 11°. The lift coefficient is still high in that range, but more importantly, the drag coefficient is extremely low. The data in Figure 19 is from an NREL S809 airfoil, but this is still a helpful starting range for the airfoil used in the optimization.

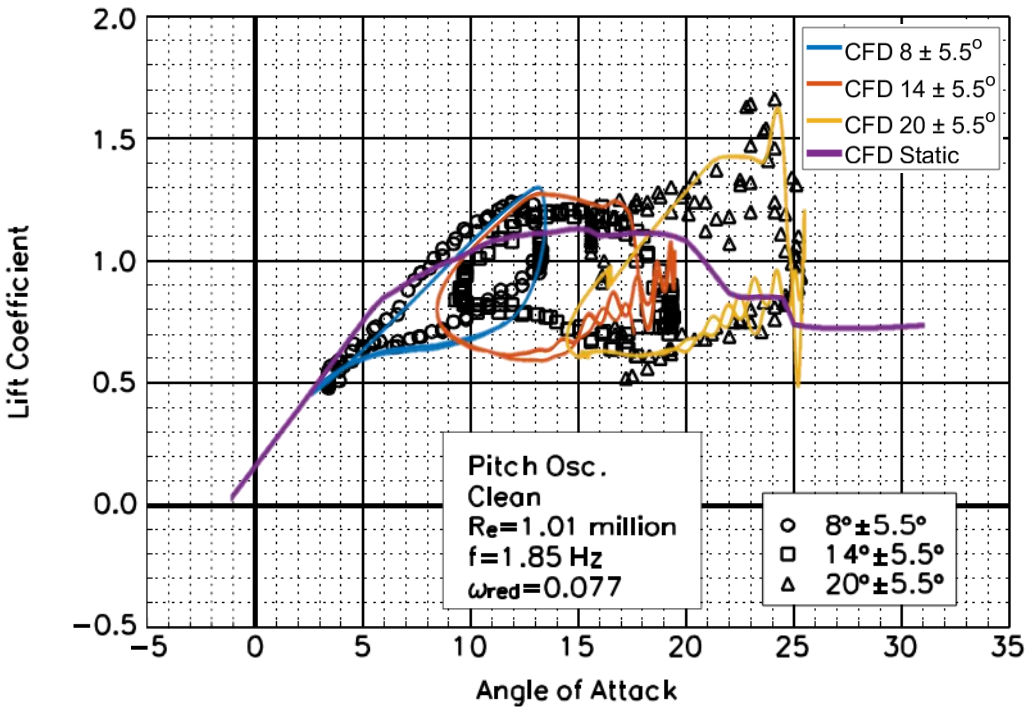

(a)

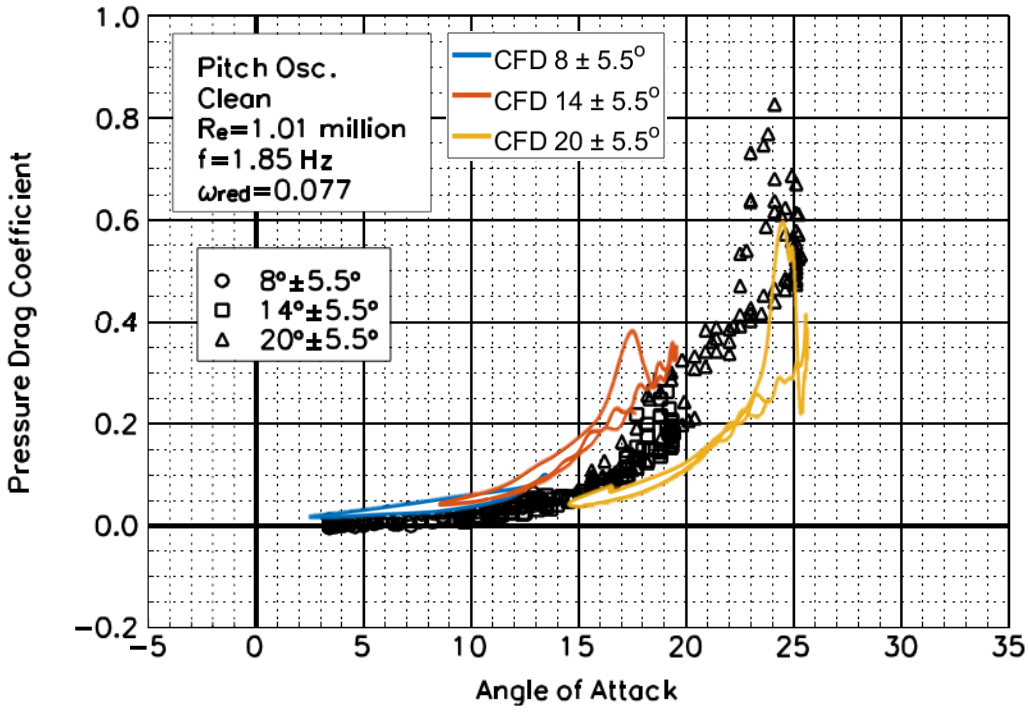

(b)

Figure 19: (a) Dynamic lift coefficients vs. angle of attack curves for S809 airfoil, experimental (black markers) vs CFD data (color lines). (b) Dynamic drag coefficients vs. angle of attack curves for S809 airfoil, experimental (black markers) vs. CFD data (color lines)

2.2.2. Waveform Evaluation

Simulation data shows that a tilted sinusoid oscillation waveform performs better than a regular sinusoid. Specifically, a waveform that goes up quickly and down slowly captures more power. A plot of this type of tilted sinusoid is shown in the bottom plot of Figure 20. The data in Figure 20 is from two simulations in Ansys Fluent® with the same conditions but different waveforms. It can be seen in the third plot of Figure 20 that the tilted sinusoid produces higher lift coefficient to drag coefficient ratios than a regular sinusoid. The primary reason is that when the airfoil moves down slowly, the lift coefficient stays higher than it does with the regular sinusoid, top plot of Figure 20. The drag coefficient is shown in the second plot of Figure 20; the peak locations differ for the sinusoids, but the average drag coefficient is about the same for both.

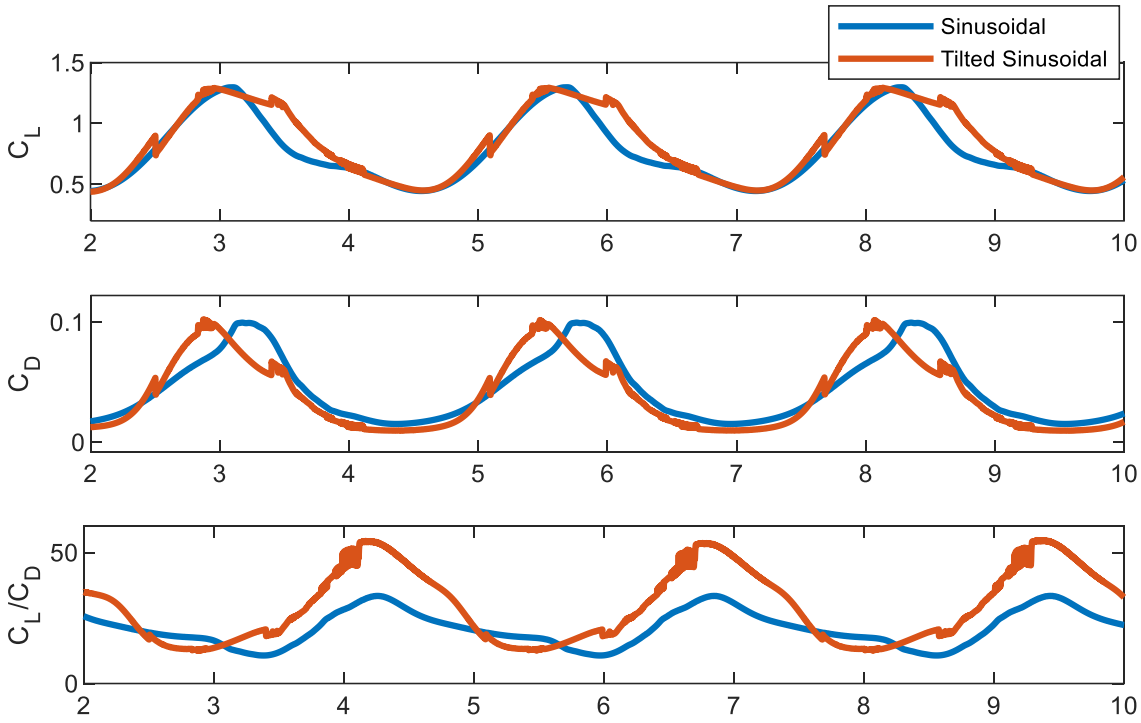

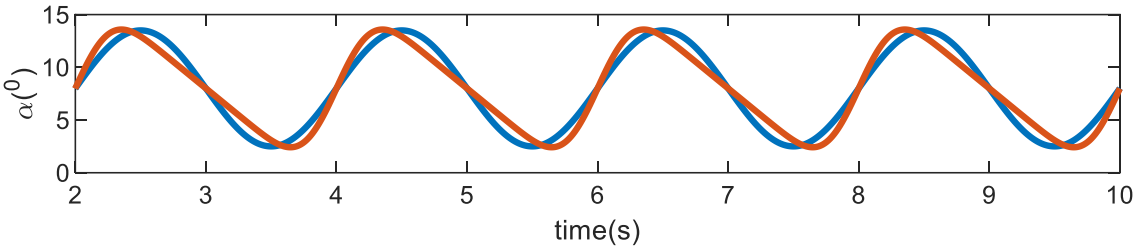

Figure 20: Comparison of C_L and C_D for regular sinusoid and tilted sinusoid waveforms. Data is from CFD simulations in Ansys Fluent®

2.2.3. Factorial Experiment

The only three independent variables that were adjusted were the average angle of attack, the amplitude, and the frequency. High, low, and medium values were selected for each independent variable. This created twenty-seven cases tested in Ansys Fluent®, and the results are shown in the box diagram in Figure 21. The figure shows the low, medium and high values for each independent variable along the bottom and right edges of the solution space box. The number at each point is the power ratio value reported by applying BEMT calculations to the data.

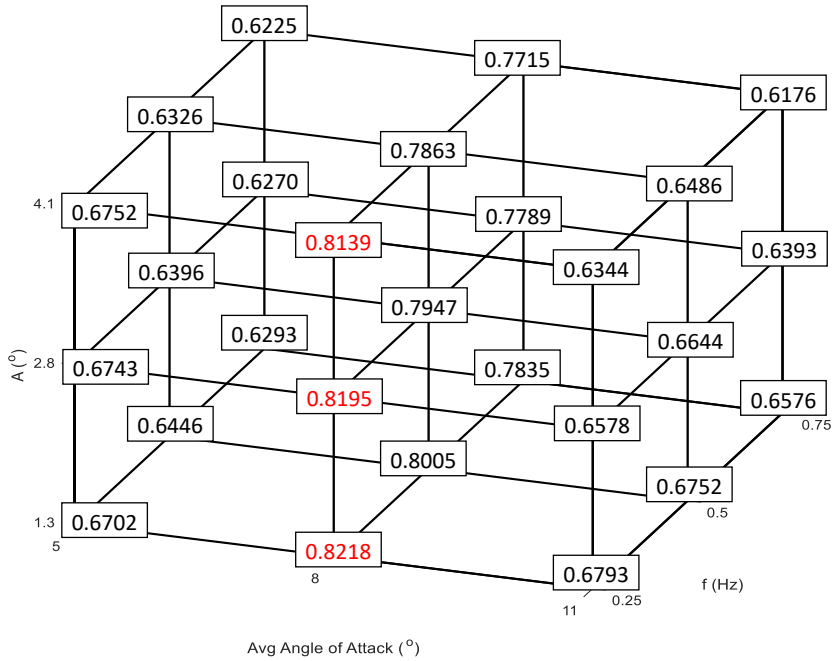

Figure 21: CFD power ratio results from the factorial experiment. The most efficient points are highlighted in red

Figure 21 provides insight into how each variable affects the final power captured from the turbine. The highest power ratio values are highlighted in red. An average angle of attack of 8 degrees captures more power than higher or lower average angles of attack. This is because with an average angle of attack of 8 degrees, the oscillation stays in a low drag range but still has a relatively high lift. Also, lower frequencies produce better power capture; the highest values are found at a frequency of 0.25 Hz. This is mainly because it requires less input power to pitch the blade at a lower frequency. Finally, the amplitude is the variable that has the slightest effect on the power captured by the blade. For the most part, smaller amplitudes result in slightly higher power capture, but the impact is minimal compared to the impact of the average angle of attack and frequency. The best result from the initial 27 simulations was used as a starting point for the hill climbing optimization.

2.2.4. Hill-Climbing Optimization

The path of the hill-climbing optimization is shown in Figure 22. The four starting points are shown as red diamonds, the optimization path is shown as a solid black line, and the maximum power ratio is shown as a green star. One of the initial points was the point of the highest power ratio from the factorial experiment. The other three were chosen around that with the idea of providing depth in every variable so that the algorithm could search the solution space effectively. A total of twenty-four simulations were run in this portion of the optimization. The search algorithm was reinitialized twice due to stalling, and each time it was restarted, the search size was refined around the highest value from the previous run. The first time the search stalled because the new point had a negative frequency, and the second stall was because the new suggested point had already been simulated. These

are both very common problems and solutions for this type of optimization. Overall, the hill-climbing algorithm discovered a 9% increase in power capture over the highest power ratio found from the factorial experiment with a final power ratio of 0.8977. The frequency, average angle of attack, and amplitude for the highest power ratio were 0.0065 Hz, 8.6022° and 0.6486°. It is expected to see a power ratio of 1 if the algorithm reaches a frequency of 0 Hz and an average angle of 8°. However, a simulation mismatch comes from calculating optimal aerodynamic coefficients with QBlade for the static case and with Ansys Fluent® for the dynamic case.

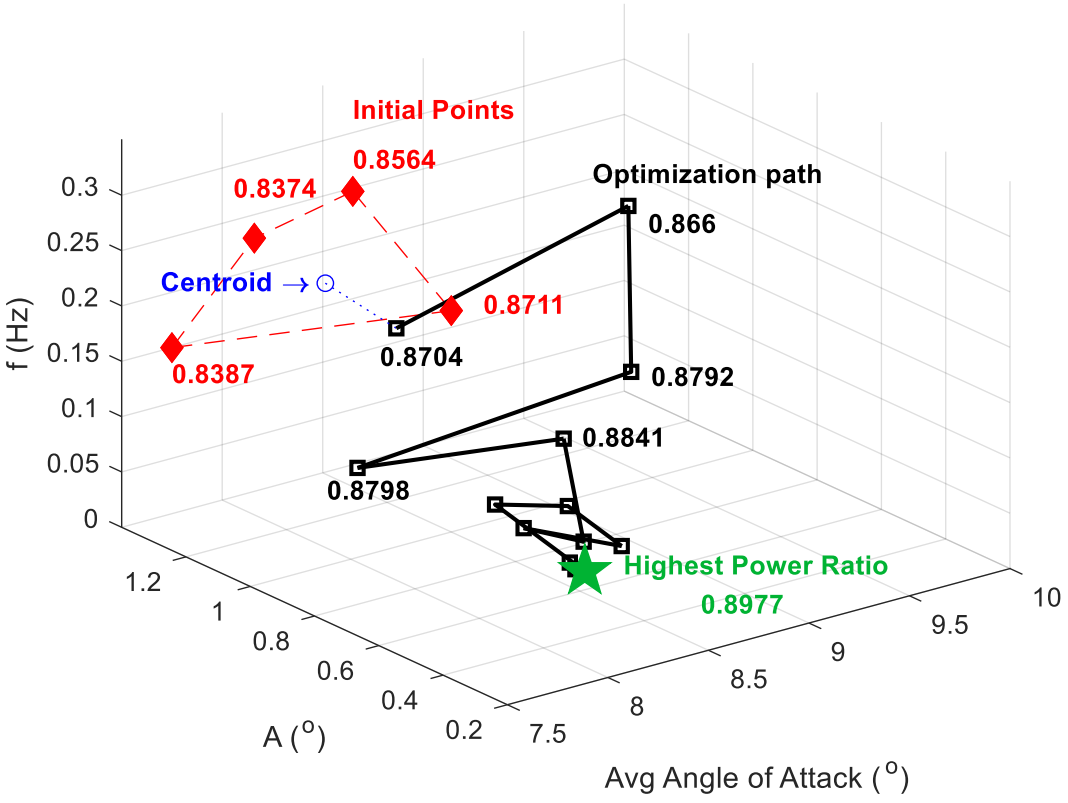

Figure 22: Path of hill-climbing optimization shown in black. Initial points are shown as red diamonds, and the point of the highest power ratio is shown as a green star (The optimization path only shows the new point for each iteration)

Hill-climbing does not guarantee finding the global maximum and can end up reporting a local maximum as the final result because the greedy approach cannot climb down hills.

This is a general problem of any convex optimization technique [54]. It could get stuck on a local maximum without knowing that there is a higher power ratio value somewhere else in the solution space. A standard method for overcoming this is to restart the search numerous times in random locations. Still, there was not enough time to do this because each simulation required intensive manual input. It consists of determining the new waveform equation, rewriting the waveform code, reinitiating the CFD simulation, and after the simulation, inputting the data into the MATLAB® code to determine the next search point. However, performing the factorial experiment first allowed for a coarse search of the relevant solution space where the maximum power ratio value is almost certain to be found. Hence, it is reasonable to believe that the hill-climbing optimization started close to the global maximum. If this is the case, the final point of this optimization's maximum power ratio can be considered the global maximum. Another optimization technique, known as ant colony optimization, was considered but not used because it also requires many simulations [55] and is outside the project's scope.

2.3.Conclusion

This study was conducted to determine whether oscillating the pitch of wind turbine blades could increase the amount of wind power harvested with a horizontal axis wind turbine. We used computer simulations and computational fluid dynamics (CFD) analysis combined with Blade Element Momentum Theory to compare the power captured by static pitch blades to that captured by oscillating blades. In the first stage of the study, we found that oscillating the blades with a tilted sinusoid waveform resulted in better performance than using a sinusoid waveform. This was evident when comparing the lift-to-drag ratio

between the two waveform inputs. In the second stage of the study, we attempted to optimize the oscillating conditions to improve performance. However, we found that the oscillating blade could only produce 89.77% of the power produced by the static blade under optimal conditions. This was due to the drag forces present in the system and the need to input additional power to oscillate the blades.

Chapter 3

Extremum Seeking Control to Improve Wind Turbine Power Capture

Adaptive control strategies are commonly used for systems that change over time, like wind turbines. Extremum Seeking Control (ESC) is a model-free real-time adaptive control strategy widely used in conventional gearbox wind turbines for Maximum Power Point Tracking (MPPT). ESC optimizes the rotor power by constantly tuning the torque control gain (k) when operating below rated power. The same concept can be applied to hydrostatic wind turbines. This chapter shows the application of ESC to HST wind turbines through simulations and experiments. The controller is also tested to show its performance under changing C_p vs. λ curves.

3.1. Materials and Methods

3.1.1. Extremum Seeking Control (ESC)

Adaptive control strategies are commonly used for systems that change over time. Extremum Seeking Control is a model-free approach that allows for continuous convex optimization. This is convenient for wind turbines because the power as a function of the torque is a convex function that changes over time. ESC works by introducing a dither signal to the variable to be optimized. Then the filtered system's output is compared to a

demodulation signal. This comparison tells the controller if it must climb up the hill with a positive or a negative slope. When the product reaches zero, an optimum value has been found [56]. The block diagram of a basic version of an ESC is shown in Figure 23.

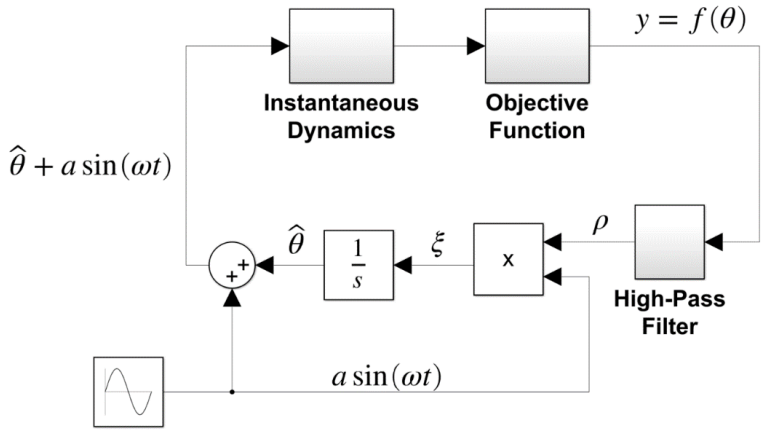

Figure 23: ESC basic version.

Where $y(\theta)$ is the objective function, ρ is the output of the objective function without a DC gain, ξ is the demodulated signal, $\hat{\theta}$ is the estimate of the best controller gain, a is the amplitude of the dither signal, and ω is the oscillation frequency of the demodulation and dither signals.

Figure 24 is a simple graphical explanation of how ESC operates in its most basic mode, where the system has instantaneous dynamics, the objective function, $y = f(\theta)$ is static and has an optimal point $y^* = f(\theta^*)$. It shows that the algorithm climbs the hill with a positive slope when the product of the **green** (ρ on the left) sinusoidal and the **gray** (demodulation signal) sinusoidal is positive. The algorithm climbs the hill with a negative slope when the product of the **blue** (ρ on the right) sinusoidal and the **gray** sinusoidal is negative. Finally, when the product is close to zero, the algorithm has found the optimal θ^* that makes $y^* = f(\theta^*)$ and no climbing is performed.

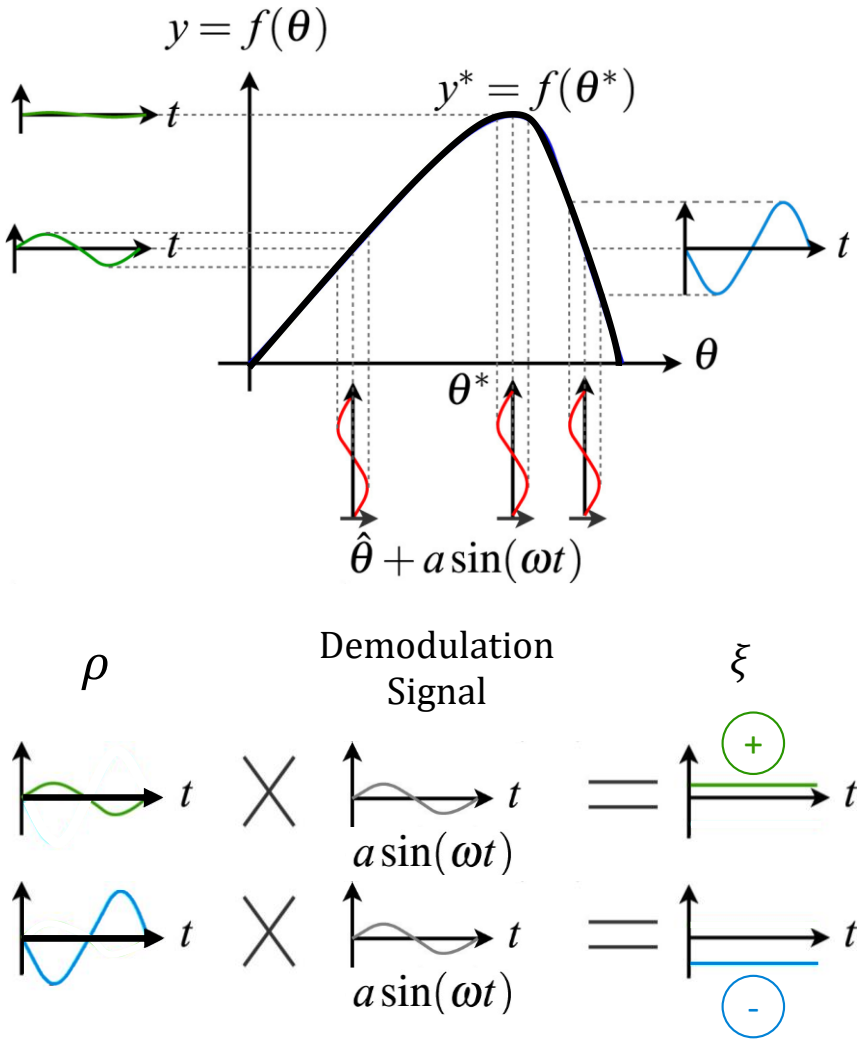

Figure 24: ESC operation example, modified from [57]

3.1.2. Controller Tuning

The block diagram for the ESC used in the HST analysis is shown in Figure 25. This architecture and the tuning process are based on the work of Xiao et al. [36] and Creaby et al. [40] but adapted to the conditions of a hydrostatic wind turbine.

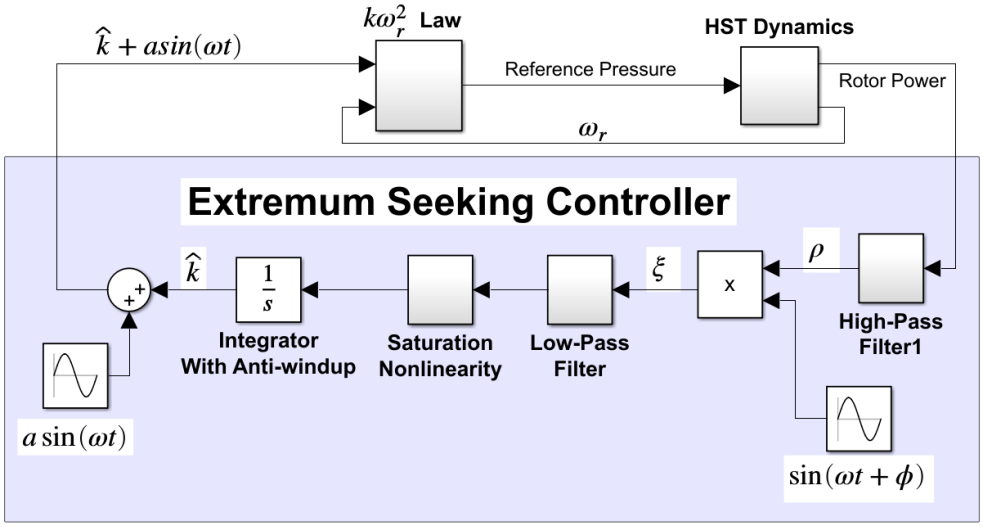

Figure 25: ESC Architecture with Anti-Windup. Modified from [29] and [30]

In Figure 25, extra parameters are added to the ESC compared to the ones in Figure 23. The added parameters are, ϕ which is the phase shift between the demodulation signal and the dither signal, and the saturation nonlinearity, which is defined as,

$$sat(x) = \begin{cases} -m, & x < -n \\ mx/n, & -n \leq x \leq n \\ m, & x > n \end{cases} \quad (15)$$

Where m and n are additional tuning parameters for the ESC.

Based on Figure 25, the variables required to implement ESC are the following:

- The oscillation frequency of the demodulation and dither signals, ω
- The phase shift of the demodulation signal, ϕ
- The cut-off frequencies of the high-pass filter (HPF), ω_{cHPF}, and the low-pass filter (LPF), ω_{cLPF}
- The amplitude of the dither signal, a
- The parameters for the saturation nonlinearity, m, and n

The first three parameters are determined from an open-loop analysis of the input-output dynamics of the system, as will be presented in section 3.1.3.

The amplitude of the dither signal must have a good signal-to-noise ratio to guarantee that the output of the objective function is comparable to the demodulation signal. In this case, 15% of the theoretical optimal torque gain, k_{opt}, for the turbine was chosen based on equation (4).

The parameters m and n are chosen to guarantee system stability and a fast response time. Instabilities are present because of fast-changing wind speeds. The saturation nonlinearity modifies the integrator gain and avoids significant nonlinear changes in the response. These gains can be tuned by monitoring the demodulated signal and understanding the order of magnitude of the desired response.

3.1.3. HST Dynamics

The dynamic model of the HST wind turbine used for this research is based on the one proposed in [23]. A schematic of the HST is shown in

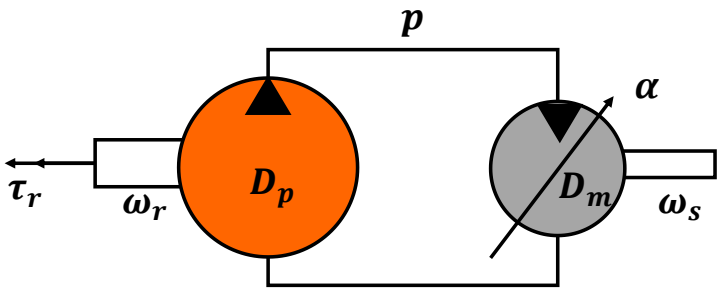

Figure 26: Hydrostatic Transmission schematic

The model consists of rotor dynamics,

$$\dot{\omega}_r = \frac{1}{J}\left[\tau_r(\omega_r, U, \beta) - b\omega_r - D_p p\right] \tag{16}$$

Where J is the combined moment of inertia of the shaft and blades, ω_r is the angular speed of the rotor, τ_r is the torque in the rotor and is a function of the angular speed of the rotor, the wind speed, U, and the pitch angle β, b is the damping coefficient of the shaft, D_p is the pump's displacement, and p is the pressure difference across the lines.

The pressure dynamics are,

$$\dot{p} = \frac{B}{V}\left(D_p\omega_r - \alpha D_m\omega_s - L_t\right) \tag{17}$$

Where B is the effective bulk modulus, V is the total volume of the fluid, α is the normalized swash plate angle of the motor, D_m is the motor's displacement, ω_s is the synchronous speed of the generator, and L_t is the leakage loss term for the hydraulic units.

Actuator dynamics are also considered and modeled as a first-order system with an experimentally obtained time constant τ_a. The transfer function is,

$$\frac{\mathrm{A}(s)}{U(s)} = \frac{1}{\tau_a s + 1} \tag{18}$$

The values used for the simulations are summarized in Table 1.

Table 1: Model Parameters and Values

Parameter	**Value**
J	$2.17\ kg\ m^2$
V	$9.82 \times 10^{-4}\ m^3$
B	$1.8\ \times 10^{9}\ pa$
D_p	$2512\ cc/rev$
D_m	$135\ cc/rev$
τ_a	$2.5641\ s$

A detailed block diagram of the system is shown in Figure 27.

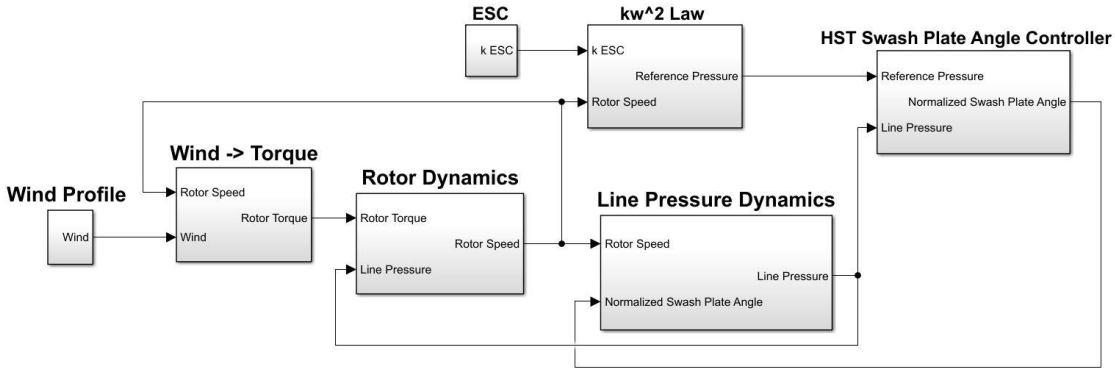

Figure 27: Block diagram for HST dynamics with ESC

3.1.4. Open-Loop Analysis for Simulation Studies

To obtain the first-order dynamics of the system, the torque gain, k, is varied, and the wind turbine rotor speed, ω_r, determined. These nonlinear dynamics are determined by creating ten step changes in k, Figure 28 top, and finding the time-varying response of ω_r, Figure 28 bottom. Here the wind is kept at a constant speed of 6 m/s, and the ESC is not included in the loop.

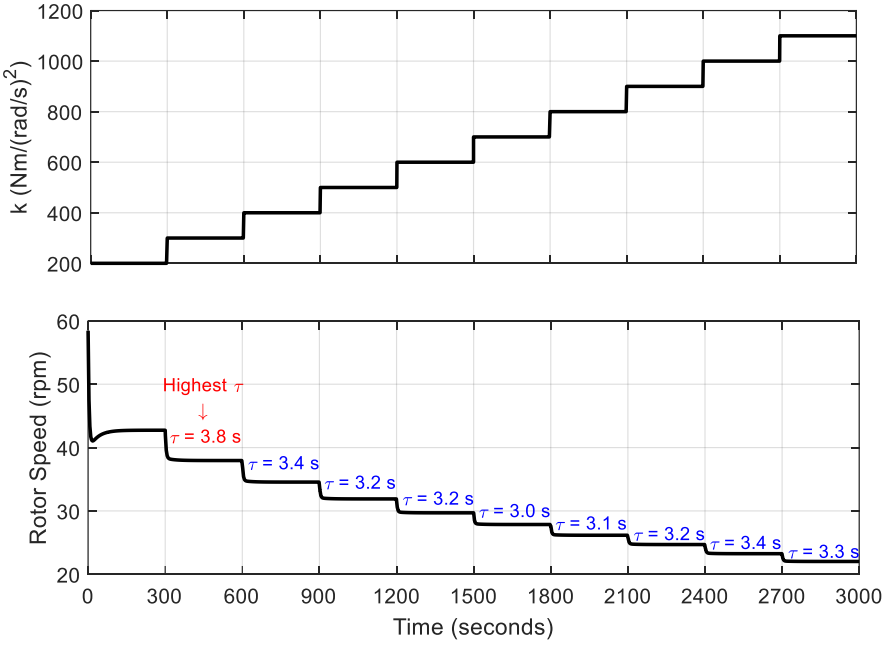

Figure 28: Open-Loop response of the system

First-order dynamics can approximate the open-loop response. The time constant, τ, can be approximated as the time it takes the system to reach 63.2% of the steady-state value, as shown in Figure 29. The time constants for each response are shown in Figure 28 bottom. The highest time constant response is chosen ($\tau = 3.8\ s$) to guarantee that the first-order approximation is representative of the nonlinear system. The resulting transfer function is,

$$\frac{\Omega_r(s)}{K(s)} = \frac{1}{\tau\, s + 1} \tag{19}$$

The step response of the first-order system compared to the system's response is shown below in Figure 29.

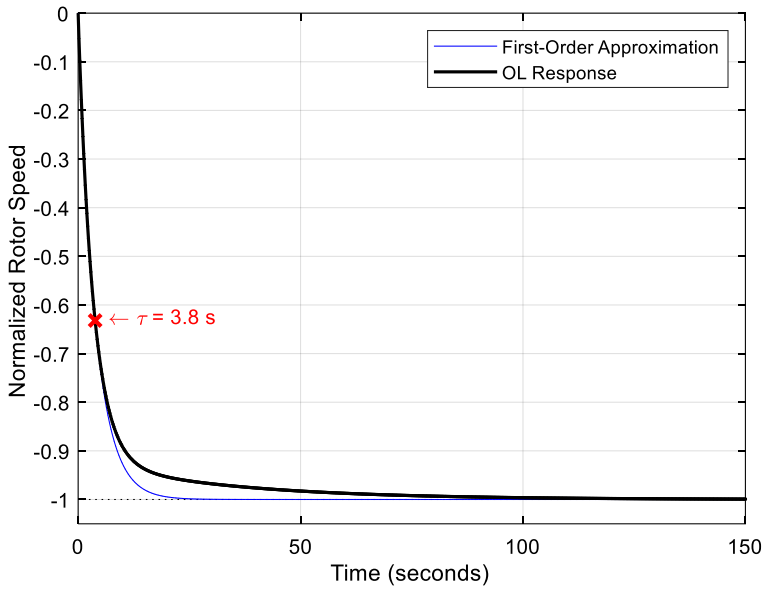

Figure 29: Step response of the first-order approximation compared to the open-loop response of the system

The frequency of the dither signal should be lower than the bandwidth of the system ($\omega_{BW} = 0.26\ rad/s$) as shown in Figure 30 top. It is conservative choosing a value of ω that is about 20% of ω_{BW} to avoid problems with the approximation. It is also essential to

avoid the tower's principal structural vibration modes. The wind turbine modes for the 60-kW turbine under study are unknown. However, for a similar wind turbine (the AOC 15/50), the fundamental vibration of the tower occurs at a frequency of $1.7\,Hz$ or $10.68\,rad/s$ [58] showing that the dither signal would not trigger detrimental vibrations on the wind turbine.

The phase shift, ϕ, of the demodulation signal depends on the value of phase shifts of the HPF, ϕ_{HPF}, and the open-loop system, ϕ_{OL}, at the dither frequency, ω. The values of ϕ_{HPF}, and ϕ_{OL}, are shown in Figure 30 bottom. These shift the original dither signal affecting the demodulated signal, ξ, therefore affecting the performance of the optimization. To compensate for these phase shifts, a phase shift, ϕ, is added to the demodulation signal.

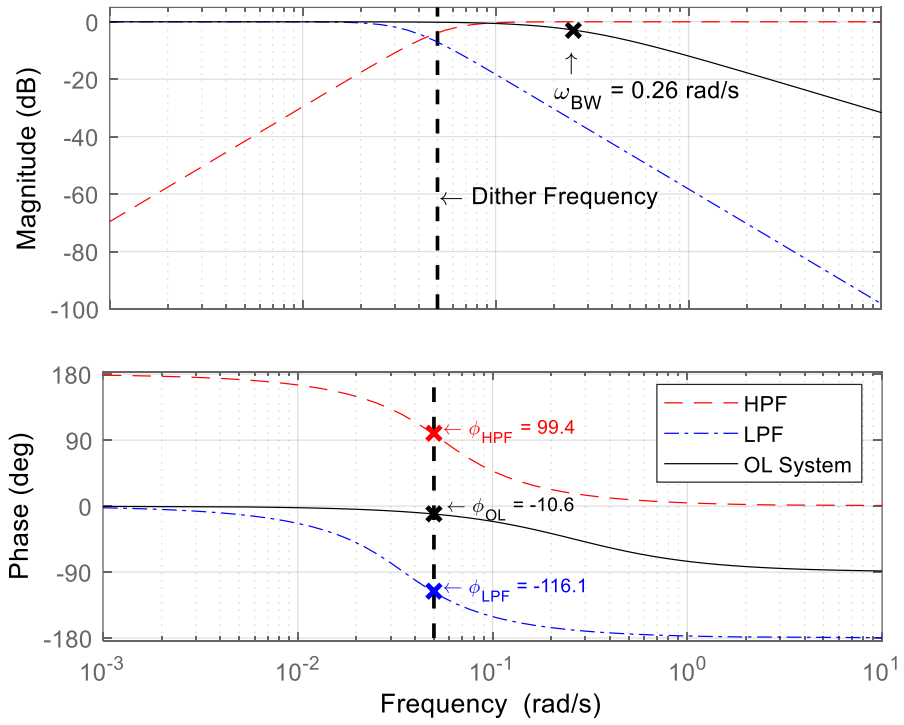

Figure 30: Bode plots of the open-loop input dynamics, HPF, LPF, and the dither frequency

The cut-off frequency of the HPF, ω_{cHPF} is chosen to filter out the low frequencies and remove the DC gain. The HPF used for this study is a second-order filter with a transfer function,

$$HPF(s) = \frac{s^2}{s^2 + 2 * 0.7 * \omega_{cHPF} * s + \omega_{cHPF}^2} \tag{20}$$

The cut-off frequency of the LPF, ω_{cLPF}, is chosen to filter out the high frequencies after the demodulation signal has been introduced to the ESC. The LPF used for this study is a second-order filter with a transfer function,

$$LPF(s) = \frac{\omega_{cLPF}^2}{s^2 + 2 * 0.7 * \omega_{cLPF} * s + \omega_{cLPF}^2} \tag{21}$$

Bode plots for the open-loop system response, the HPF, and the LPF are shown in Figure 30.

The parameters found for the ESC are summarized in Table 2.

Table 2: ESC parameters for initial simulations

Parameter	**Value**
HPF Cut-off frequency, ω_{cHPF}	$0.055\ rad/s$
LPF Cut-off frequency, ω_{cLPF}	$0.035\ rad/s$
Dither frequency, ω	$0.05\ rad/s$
Phase shift, ϕ	$0.48\ rad$
Amplitude of dither signal, a	$57.66\ Nm/(rad/s)^2$
Saturation nonlinearity	$m = 0.85$ $n = 0.2$

3.1.5. Open-Loop Analysis for Experimental Studies

As for the simulations, the open loop response of the system, with input, k, and output, rotor speed ω_r, is obtained. k is the input variable that we are dithering, and ω_r is the output of the system. The step response is shown in Figure 31.

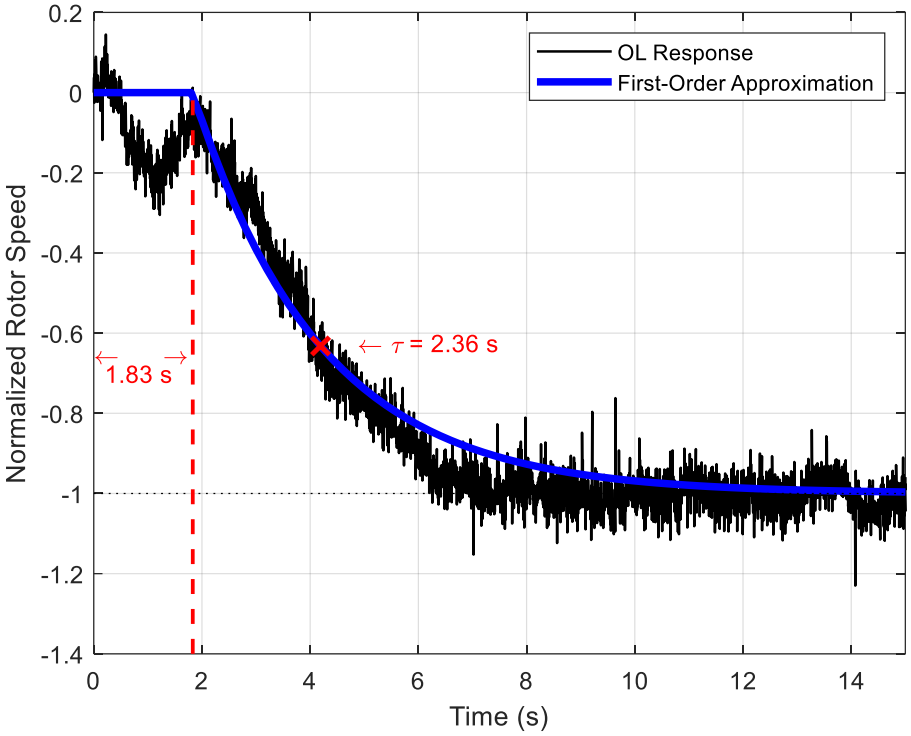

Figure 31: Step response of open loop system

A first-order system with a delay is used. This open loop test revealed a delay of 1.83s, which must be considered for re-tuning the parameters compared to the simulation studies [29]. The first-order transfer function with a delay of the open loop response is given by equation (22).

$$H(s) = \frac{\Omega(s)}{K(s)} = e^{-1.83\,s}\frac{1}{2.36\,s + 1} \tag{22}$$

Again, the frequency response of the system is used to choose the best dither/demodulation frequency, ω, the phase shift of the demodulation signal, ϕ, and the high pass filter (HPF) and low pass filter (LPF) cut-off frequencies, ω_{cHPF} and ω_{cLPF}.

The frequency response of the system is shown in Figure 32.

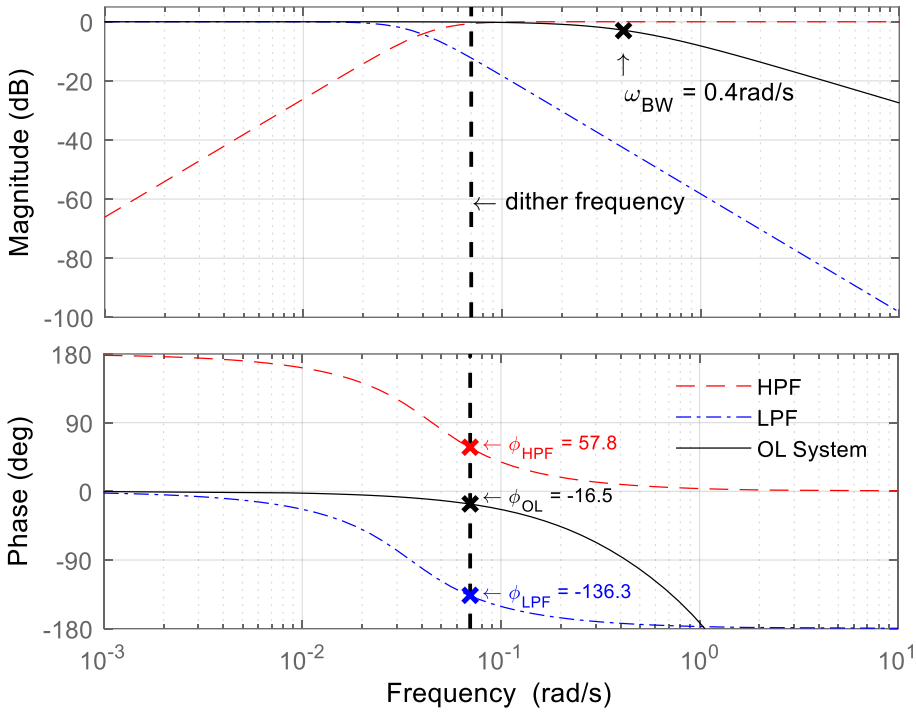

Figure 32: Bode diagram of open loop system, HPF and LPF

From the Bode Plot, the dither/demodulation frequency is chosen to be well within the bandwidth, ω_{BW}, of the open loop system. The phase shift is calculated by adding the phase shifts of the open loop system and the HPF. The cut-off frequency of the HPF is selected to filter out anything below the dither frequency without affecting it. The cut-off frequency of the LPF is selected to filter the dither frequency and everything above it. The amplitude, a, of the dither signal is chosen so the sinusoidal is not overshadowed by the noise's

amplitude. The saturation nonlinearity gains are tuned to avoid significant nonlinear changes in the response. A summary of the chosen parameters is given in Table 3.

Table 3: ESC Parameters for experiments

Parameter	Value
HPF Cut-off frequency, ω_{cHPF}	$0.045\ rad/s$
LPF Cut-off frequency, ω_{cLPF}	$0.035\ rad/s$
Dither frequency, ω	$0.07\ rad/s$
Phase shift, ϕ	$0.72\ rad$
Amplitude of dither signal, a	$76.88\ Nm/(rad/s)^2$
Saturation nonlinearity	$m = 3$ $n = 0.6$

These parameters were used to re-run the simulations and the experiments presented in the experimental validation section of this chapter.

3.1.6. HST Test Stand at the University of Minnesota

The HST test stand at the University of Minnesota is shown in Figure 33. The power regenerative test stand consists of an HST on the left side and an HSD (hydrostatic drive) on the right side. The test stand is rated at 100 kW output with only 50 kW input because of power regenerative. The HSD uses hardware-in-the-loop (HIL) simulation to emulate the aerodynamic torque, allowing testing for steady, step, and turbulent wind conditions. The HSD is a speed-down transmission with a variable displacement pump and a fixed displacement motor. The HST is a speed-up transmission with a fixed displacement pump and a variable displacement motor. Each transmission has an independent hydraulic system. The HST is the transmission where the baseline controller and the ESC are tested.

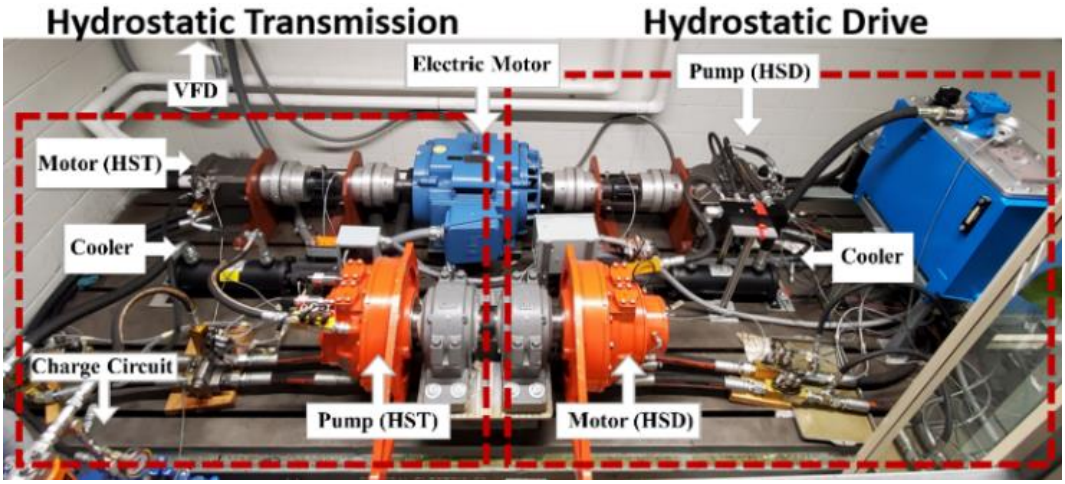

Figure 33: HST Test stand at the University of Minnesota

Since this is a coupled system, a decoupling control strategy is required. A detailed description is presented by Mohanty [59], but outside the scope of this thesis. The system is connected to a Windows machine with an interface built on MATLAB Simulink Real-Time® for data acquisition and control. Twenty-seven sensors measure all components' pressure, flow, temperature, speed, and torque. Detailed descriptions of the test stand, its components, and the dynamics of the system can be found in [14], [60], and [23].

3.2. Results and Discussion

This work was evaluated through simulations, and the results were validated at the U of M test stand presented in section 3.1.6.

3.2.1. Simulation Studies

This section presents the results of simulation studies evaluating the use of ESC for a 60-kW hydrostatic transmission wind turbine [23], [26]. First, a systematic approach to establish the ideal ESC parameters is shown. Second, a comparison of the power capture

performance of ESC versus the conventional torque control law (the $k\omega^2$ law) is shown. The simulations include a time changing power capture coefficient (C_p) to clearly show the advantages of using ESC. Studies under steady and realistic wind conditions show the main advantages of using ESC for a hydrostatic wind turbine.

The differences with a conventional gearbox wind turbine come from the continuously variable transmission and the dynamics of the hydraulic system. These differences require the use of different parameters in the ESC design.

Simulations and analysis in MATLAB® and Simulink are performed to test and compare the ESC and the baseline controller under three different wind conditions: steady wind, step wind, and turbulent wind.

3.2.1.1. Steady Wind Study

The first step of the study is to investigate the effect of changing the C_p vs λ curve for the baseline controller and the ESC under steady wind. Figure 34 shows the three C_p vs. λ curves that are studied. The "ideal" (solid black line) curve is what the baseline controller uses to calculate k_{opt}. This curve has a $\lambda_* = 6.5$ and a $C_{pmax} = 0.41$. The "modified" (blue dotted, red dotted lines, and green dotted) curves will simulate a change from the ideal curve by changing the optimal tip-speed-ratio, λ_*, of the ideal case to 5.5, 4.5, and 7.5 but maintaining the same C_{pmax}. The theoretical C_p vs. λ curves were created based on equation (23) [61].

$$C_p(\lambda,\beta) = C_1\left(\frac{C_2}{\lambda_i} - C_3\beta - C_4\beta^x - C_5\right)e^{\frac{C_6}{\lambda_i}}$$

$$\frac{1}{\lambda_i} = \frac{1}{\lambda + 0.08\beta} - \frac{0.035}{\beta^3 + 1} \tag{23}$$

The coefficients are then chosen to obtain the ideal and modified cases. The ideal case with $\lambda_* = 6.5$ has the following coefficients: $\beta = 0$, $C_1 = 0.1546$, $C_2 = 116$, $C_5 = 11.5$ and $C_6 = 0.0068$.

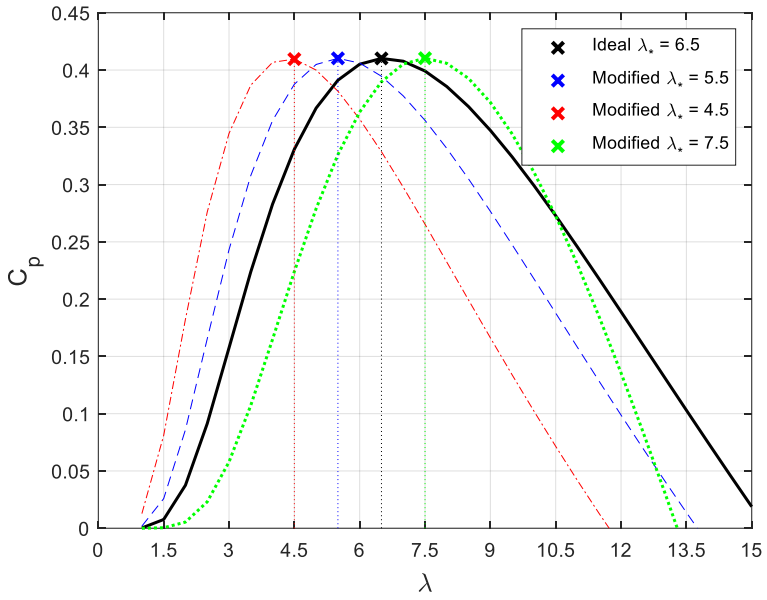

Figure 34: C_p vs. λ curves for the ideal case and the modified cases

The simulations ran for $5000\ s$. In the first $2000\ s$, the system was operating under ideal conditions. At the $2000\ s$ mark, the C_p vs. λ curve was changed to the modified curves and the simulation continued to run for another $3000\ s$. The wind used for these simulations is steady wind at $8\ m/s$.

As can be seen in Figure 35, Figure 36, and Figure 37, the steady wind study shows several interesting results. First, it clearly shows that the performance of the baseline controller

decreases if the ideal C_p vs. λ curve is not used. Second, it shows that the ESC can find the optimal rotor power independently of the change in λ_*. However, the higher the change the longer it takes the ESC to reach a stable response. For example, in the modified $\lambda_* = 5.5$ case the rotor power reaches the optimal point within $500\ s$. In the modified $\lambda_* = 4.5$ case the rotor power reaches the optimal point in within $1500\ s$. Also, when the C_p vs. λ curve has a higher curvature, the optimized rotor power with ESC is smoother. This is because the gradient is more significant as you approach the tip of the curvature and the optimal point is more precise, as seen in the modified $\lambda_* = 4.5$ case. With a lower curvature, the optimal point is not as precise; hence the ESC oscillates more, as seen in the ideal case, the modified $\lambda_* = 5.5$ and the modified $\lambda_* = 7.5$ cases.

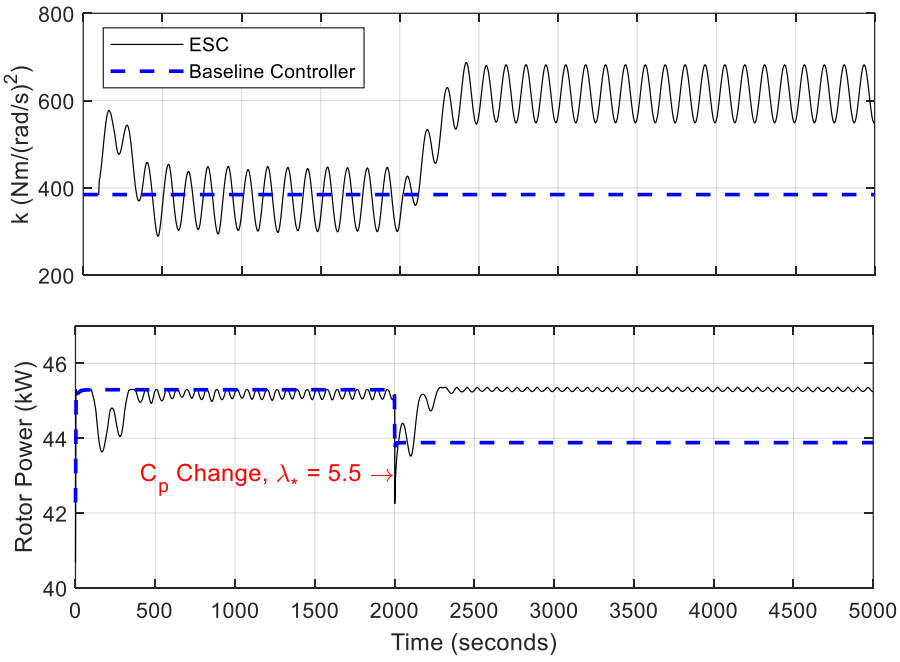

Figure 35: Torque gain and rotor power for the baseline controller and for the ESC with modified $\lambda_* = 5.5$

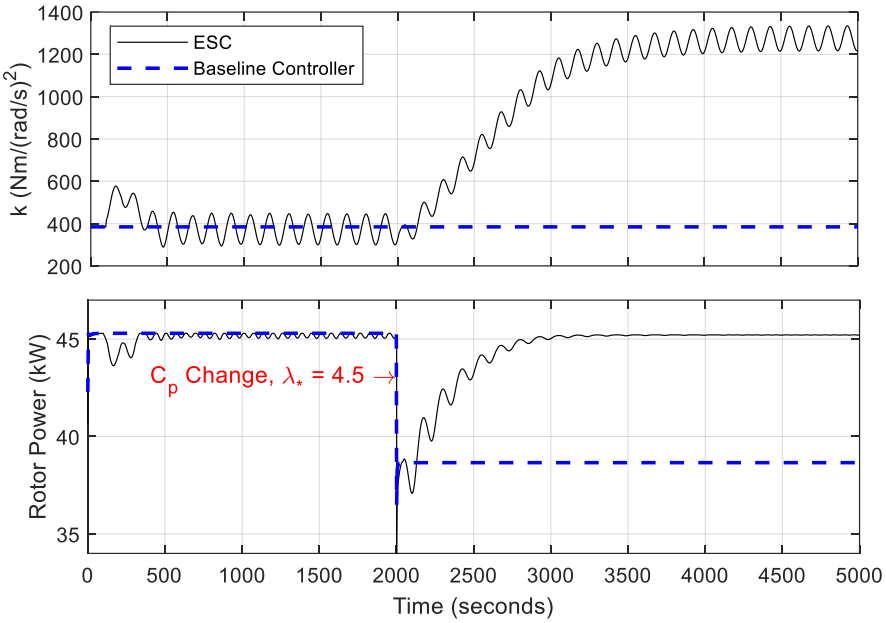

Figure 36: Torque gain and rotor power for the baseline controller and for the ESC with modified $\lambda_* = 4.5$

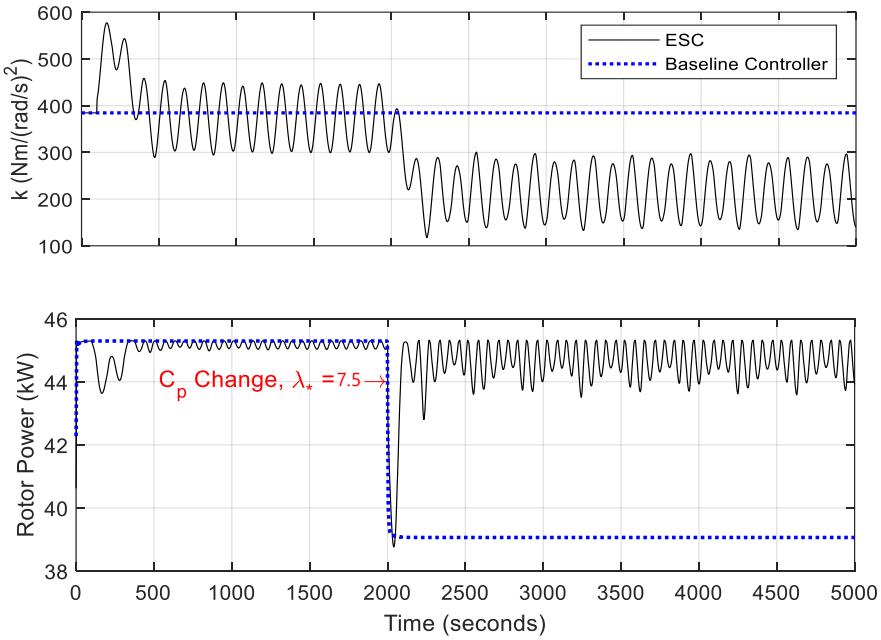

Figure 37: Torque gain and rotor power for the baseline controller and for the ESC with modified $\lambda_* = 7.5$

3.2.1.2. Step Wind Study

A step wind study was performed based on the steady wind study results. Two main simulations were performed, one under ideal conditions and one under the modified $\lambda_* = 5.5$ case. The results are summarized in Figure 39 and Figure 40. The step wind input used for the simulations is shown in Figure 38.

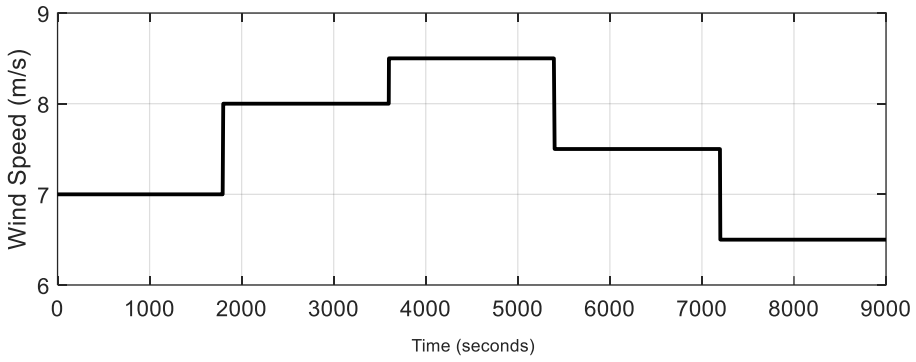

Figure 38: Step wind input for simulations

The step wind study shows that the ESC can perform at least as well as the baseline controller under different wind speeds in control region 2. When $\lambda_* = 6.5$ the ESC can reach the same optimal conditions as the baseline controller, Figure 39. When $\lambda_* = 5.5$ the ESC outperforms the baseline controller and can always capture more power, Figure 40. In both cases, ESC is more affected by transients at higher wind speeds. However, when $\lambda_* = 5.5$ there is a bigger difference in rotor power at higher wind speeds, meaning that the ESC can extract more power from the wind when the wind speeds are close to the rated speed of $10\ m/s$.

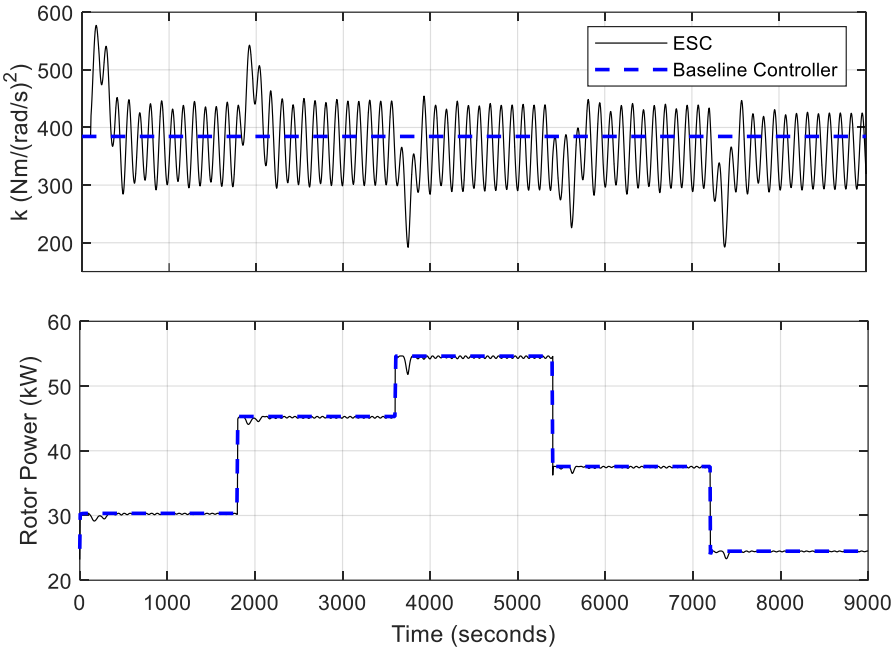

Figure 39: Step wind results for ESC and baseline controller under ideal $\lambda_* = 6.5$

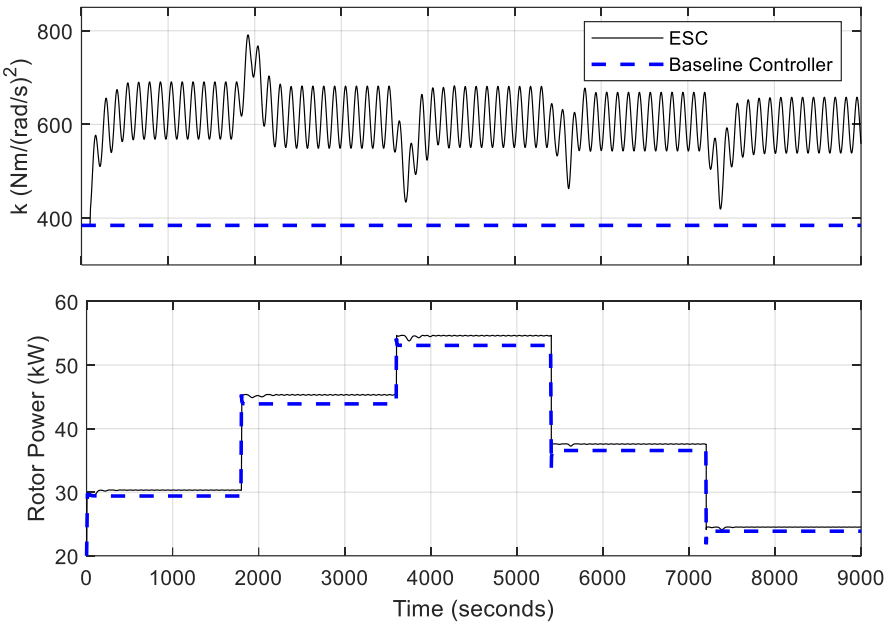

Figure 40: Step wind results for ESC and baseline controller under ideal $\lambda_* = 5.5$

3.2.1.3. Turbulent Wind Study

Simulations under turbulent wind were performed to complete the study. The same conditions as in the step wind study are used, i.e., ideal case and modified $\lambda_* = 5.5$ case. The results are summarized in Figure 42 and Figure 43. The turbulent wind used for the simulations is shown in Figure 41. This wind profile was generated using Turbsim, with a 2% turbulence intensity.

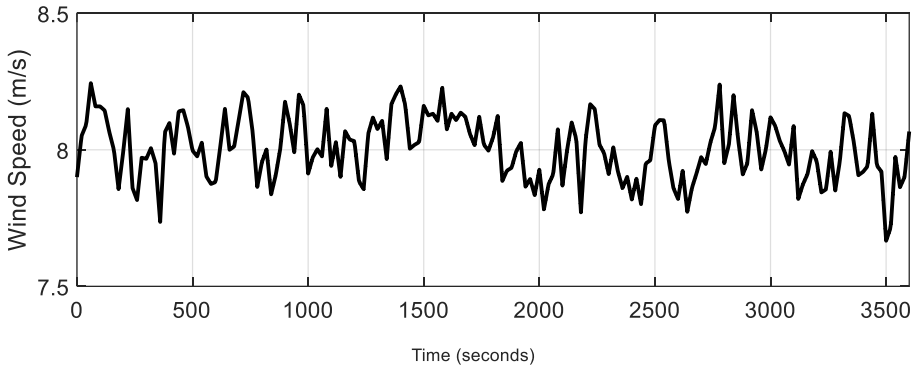

Figure 41: Turbulent wind input for simulations

The turbulent wind study shows in the ideal case that the ESC is close to reaching the optimal torque gain value, but it oscillates as the wind speed oscillates. When compared to the baseline controller, it underperforms due to the rapid wind changes, Figure 42. When $\lambda_* = 5.5$ the ESC is always capturing more power than the baseline controller independently of the rapid wind changes, Figure 43. It can be noticed that this is because the torque gain for the baseline controller is never at an optimal point. In contrast, the one for the ESC is constantly approaching the optimal operating point.

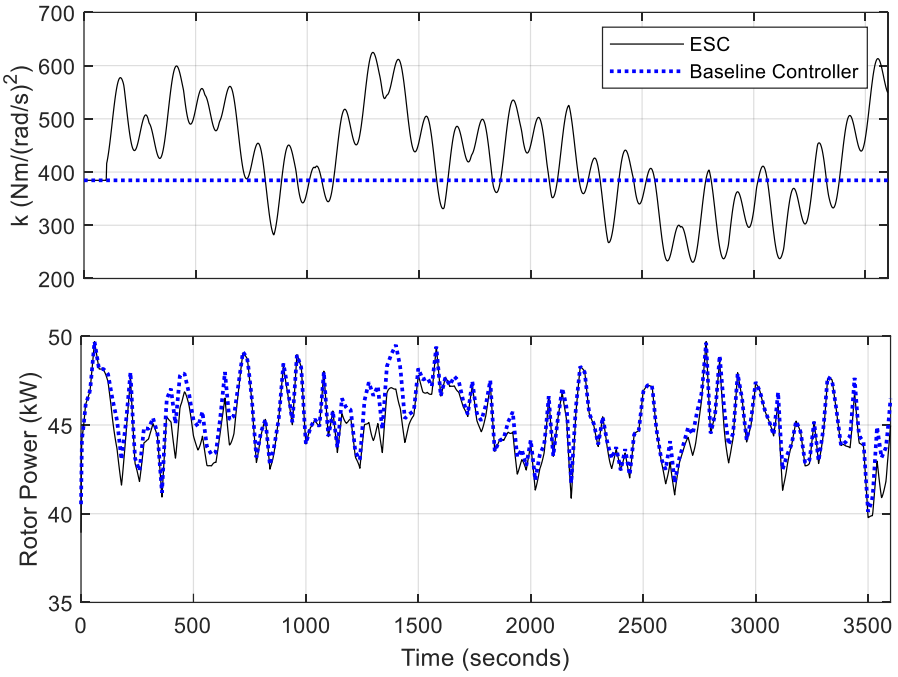

Figure 42: Turbulent wind results for ESC and baseline controller under ideal $\lambda_* = 6.5$

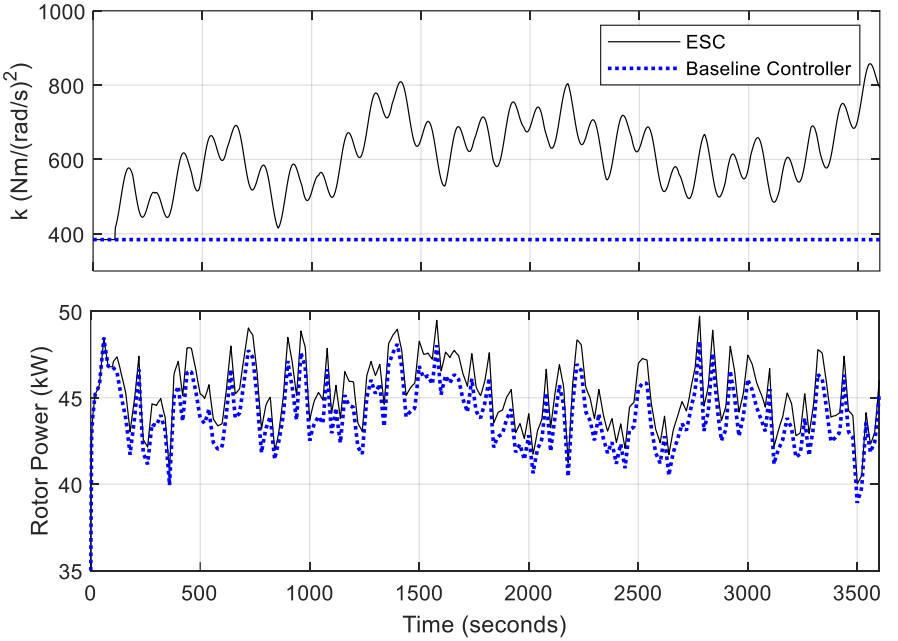

Figure 43: Turbulent wind results for ESC and baseline controller under ideal $\lambda_* = 5.5$

For the step wind and turbulent wind studies, further investigations of the power changes in the $\lambda_* = 5.5$, $\lambda_* = 4.5$, and $\lambda_* = 7.5$ cases were performed. To do so, a power ratio,

P_{ratio}, between the average rotor power with the ESC, $\overline{P}_{rot_{ESC}}$, and the average rotor power with the baseline controller, $\overline{P}_{rot_{base}}$, was defined as:

$$P_{ratio} = {\overline{P}_{rot_{ESC}}}\Big/{\overline{P}_{rot_{base}}} \tag{24}$$

The results of this study are shown in Table 4.

Table 4: Comparison of power ratios depending on the input wind and λ_* values

Wind	$\boldsymbol{\lambda_*}$	**Power Ratio**
Step	6.5	0.9964
Turbulent		0.9887
Step	5.5	1.0289
Turbulent		1.0278
Step	4.5	1.1290
Turbulent		1.1229
Step	7.5	1.0599
Turbulent		1.0467

The main conclusion is that even if the ideal conditions are in place, the ESC can perform as well as the baseline controller. If there are any changes in the C_p vs. λ curve, then having an ESC in place will help with capturing more power from the wind. The power ratio does not change linearly, and the gains in power grow significantly as the λ_* value moves away from the ideal case.

3.2.2. Experimental Validation

This section presents an experimental validation of the simulation results presented above. Results were obtained for steady wind experiments with $\lambda_* = 6.5$ and $\lambda_* = 4.5$, for step wind experiments for $\lambda_* = 6.5$ and $\lambda_* = 5.5$, and for anti-windup experiments for $\lambda_* = 6.5$. All the experiments were run with wind speeds within region 2. Figure 34 shows the C_p vs. λ curves for the different cases.

3.2.2.1. Anti-Windup Study

The anti-windup algorithm was tested under step wind conditions, Figure 44.

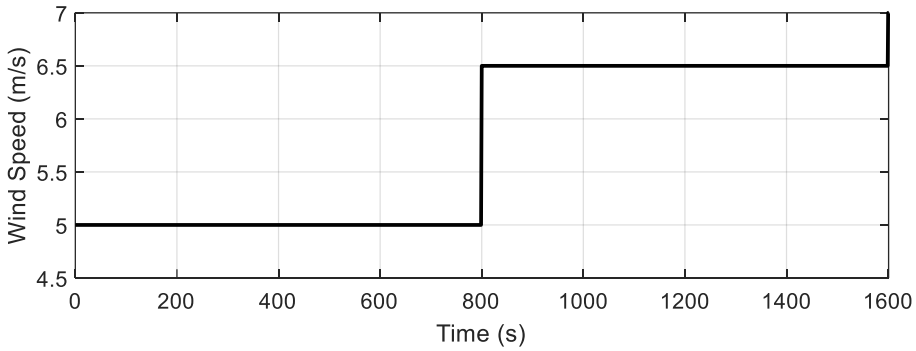

Figure 44: Step wind profile for anti-windup experiments

The results of using an anti-windup algorithm to overcome the saturation of $\hat{k}$ are shown below in Figure 45.

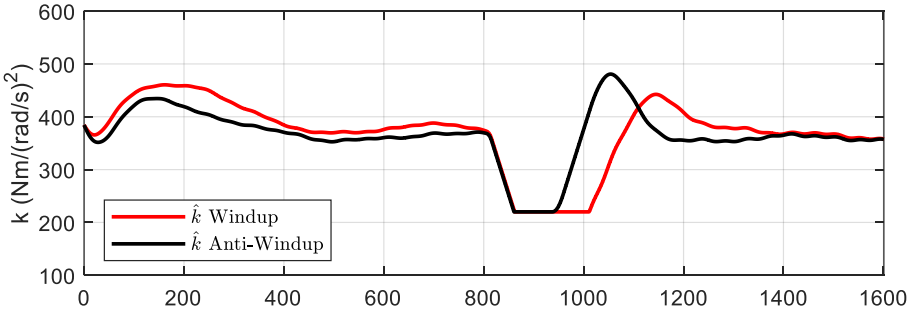

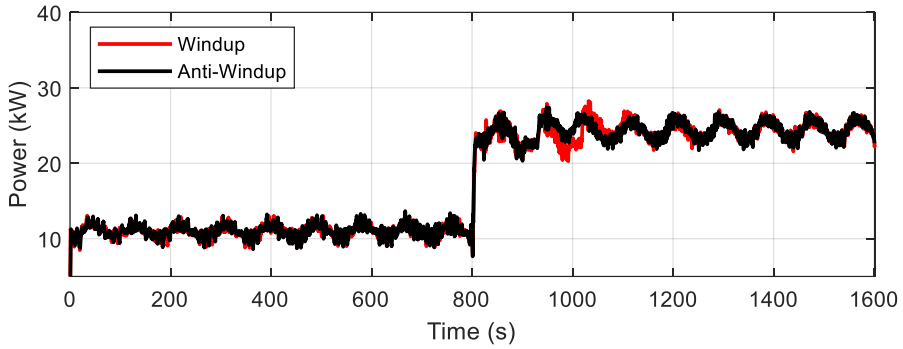

Figure 45: Anti-Windup results

Because of windup, ESC took approximately 116 s in saturation before returning to find the optimal. When the anti-windup is implemented, this time is reduced to 82 s, a difference of 34 s. The power capture is not affected significantly in this case (only a 0.29% improvement), but with higher wind steps, the power capture will be more significant.

3.2.2.2. Step Wind Study

The steady wind study consisted of verifying if the ESC would adapt to a sudden change in the C_p vs. λ curve at constant wind speed of 6 m/s. A change from $\lambda_* = 6.5$ to $\lambda_* = 4.5$ was introduced at 800 s for the ESC and the baseline controller. The experimental results effectively validated what was seen previously in simulations. The results are shown in Figure 46.

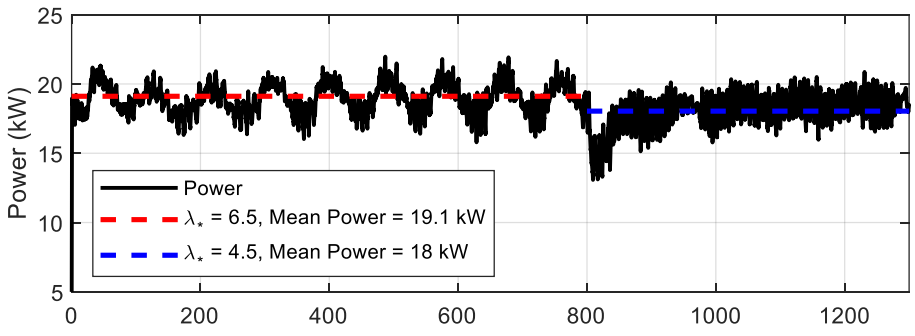

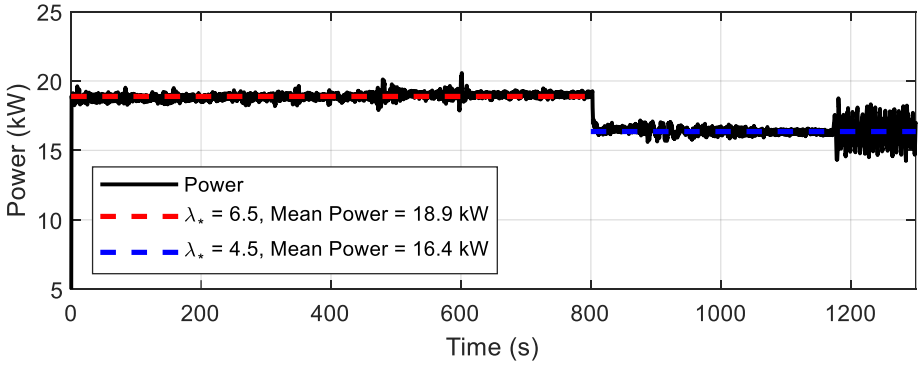

Figure 46: Steady wind responses for ESC (top) and baseline controller (bottom) with a λ_* change from 6.5 to 4.5

After the change of λ_*, the ESC shows a drop in power of 5.6% and the baseline controller shows a drop in power of 13.4%. There is a drop in the ESC because the controller needs more time to adapt to the ideal gain fully; if fully adapted, the percent drop is not as significant, less than 1%. Data was taken for a more extended period to guarantee adaptation, but for a fair comparison with the baseline controller, only the first 1300s of data are shown and used for these calculations. Even under these conditions, the results show that a change in the C_p vs. λ curve can result in a relative power loss of 7.8% if the k gain is kept constant. This validates the better performance of the ESC versus the baseline controller, showing the importance of adaptation.

3.3. Conclusion

In this study, an ESC for a $60\,kW$ hydrostatic wind turbine was implemented and compared to a baseline controller. The study's results were presented through simulation and then validated through experimental tests at the University of Minnesota's power regenerative test stand. The results showed that the ESC was able to perform as well as the baseline controller under ideal conditions. However, when operating under modified

conditions, the ESC consistently outperformed the baseline controller. The performance of the ESC was affected by changes in the C_p vs. λ curve, with more significant changes from the ideal case resulting in longer times for the ESC to find an optimal torque gain. The curvature of the C_p vs. λ curve also impacted the performance of the ESC, with a higher curvature resulting in better performance. Overall, the proposed adaptive controller achieved the goal of finding an optimal torque control gain under both simulated and experimental conditions when the Cp vs. λ curve changed over time.

Chapter 4

Dynamic Temperature Control to Improve HST Efficiency

This chapter focuses on improving HST efficiencies by optimizing oil viscosity through temperature control. The efficiency of hydraulic pumps and motors involves mechanical and flow losses. If the viscosity is too high, mechanical losses dominate. If the viscosity is too low, volumetric losses dominate. An optimum viscosity that balances these two factors can be found. Since viscosity is a strong function of temperature, control can be used to dynamically change the viscosity as operating conditions change to maintain maximum efficiency. The chapter describes the simplified viscosity model for the pump and the motor and the simplified heat exchanger model used to control the system's temperature. Two temperature control approaches are investigated Proportional plus Integral (PI) control and Sliding Mode Control (SMC).

4.1. Materials and Methods

4.1.1. Modeling Hydraulic Pumps and Motors

This study uses a mathematical efficiency model dependent on non-dimensional viscosity, two non-dimensional length ratios, and fractional displacement. Instead of using physical dimensions for the non-dimensional length ratios, constant viscosity experiments determined these parameters for the pump and motor. The predicted results of the model were compared to validation experiments where viscosity was varied by changing

temperature. Several existing mathematical models in the literature describe the relationship between viscosity and efficiency for hydraulic components. Parametric pump and motor efficiency models have been developed and refined by Wilson [62], Reethof [63], Schlosser [64], McCandlish and Dorey [65], and others. While the accuracy of these models may be higher, their complexity could be a drawback for optimization studies.

This study examines an extension of a simple efficiency model for pumps and motors proposed by Stelson and Wang [66]. In this study, the losses are assumed to be limited to the piston-cylinder gap. If physical dimensions are used in this model, the predicted efficiency is too high since losses from other interfaces within the pump or motor are neglected. Although different gap geometries are more complex than the piston-cylinder, losses from these other interfaces can be included by modifying the model's parameters to match experiments.

Because modeling the efficiency of hydraulic pumps and motors is challenging, the experienced reader will likely question the validity of such a simple model. Such concerns are valid if the models were being used for design purposes. But a less accurate model may be suitable for optimization. Large viscosity-dependent losses occur from leakage and viscous drag. Other losses due to compression, cavitation, commutation, orifice effects, and irregular geometry can be significant but less likely to be viscosity sensitive. If the viscosity dependence of these effects is small, the simplified model will still find the optimum viscosity.

The approach to optimization here lies between using a more detailed but more challenging to characterize model versus a model-free approach. This intermediate approach is semi-empirical, meaning that a model based on physics is used with parameters fit from measurements.

Two dimensionless loss factors are found in this model, l_Q, the leakage loss factor, equation (25), and l_T, the friction loss factor, equation (26), [43].

$$l_Q = \frac{1}{3}\hat{d}^3\widehat{D}^2\frac{1}{f}\frac{1}{\hat{\mu}} \tag{25}$$

$$l_T = 4\frac{1}{\hat{d}}\frac{1}{\widehat{D}^2}\frac{1}{f}\hat{\mu} \tag{26}$$

where $\hat{d}$ is the dimensionless gap, $\widehat{D}$ is the dimensionless diameter, f is the displacement fraction, and $\hat{\mu}$ is the dimensionless viscosity defined as $\hat{\mu} = \frac{\mu\omega}{p}$. With μ being the dynamic viscosity, ω the angular speed, and p the pressure.

These loss factors are used to compute the pump and motor's volumetric and mechanical efficiency. Since these are the only two factors considered, the overall efficiency of the pump (η_p) and the motor (η_m) are given as [43]:

$$\eta_p = \frac{1 - l_Q}{1 + l_T} = \frac{1 - \left(\frac{1}{3}\hat{d}^3\widehat{D}^2\frac{1}{f}\frac{1}{\hat{\mu}}\right)}{1 + \left(4\frac{1}{\hat{d}}\frac{1}{\widehat{D}^2}\frac{1}{f}\hat{\mu}\right)} \tag{27}$$

$$\eta_m = \frac{1 - l_T}{1 + l_Q} = \frac{1 - \left(4\frac{1}{\hat{d}}\frac{1}{\widehat{D}^2}\frac{1}{f}\hat{\mu}\right)}{1 + \left(\frac{1}{3}\hat{d}^3\widehat{D}^2\frac{1}{f}\frac{1}{\hat{\mu}}\right)} \tag{28}$$

The dimensionless parameters for the HST's pump and motor at the University of Minnesota are found by fitting the model to experimental data. The code to fit the parameters is shown in Appendix b.1. The pump's overall efficiency model fit is shown in Figure 47 and is based on equation (29).

$$\eta_{pump} = \eta_{p_{pump}} \eta_{m_{pump}} \tag{29}$$

With $f = 1$ because the HST is a fixed displacement pump.

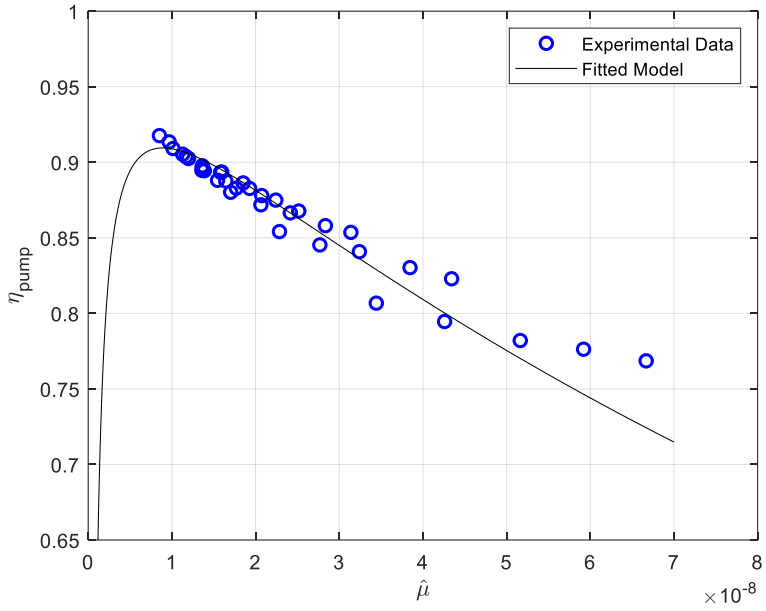

Figure 47: HST pump's overall efficiency data and fitted model

The dimensionless gap for the pump is, $\hat{d} = 0.0300$, and the dimensionless diameter for the pump is, $\widehat{D} = 0.0047$.

The motor's overall efficiency model fit is shown in Figure 48 and is based on equation (30).

$$\eta_{motor} = \eta_{p_{motor}} \eta_{m_{motor}} \tag{30}$$

The dimensionless gap for the motor is, $\hat{d} = 0.0371$, and the dimensionless diameter for the motor is, $\widehat{D} = 0.0269$.

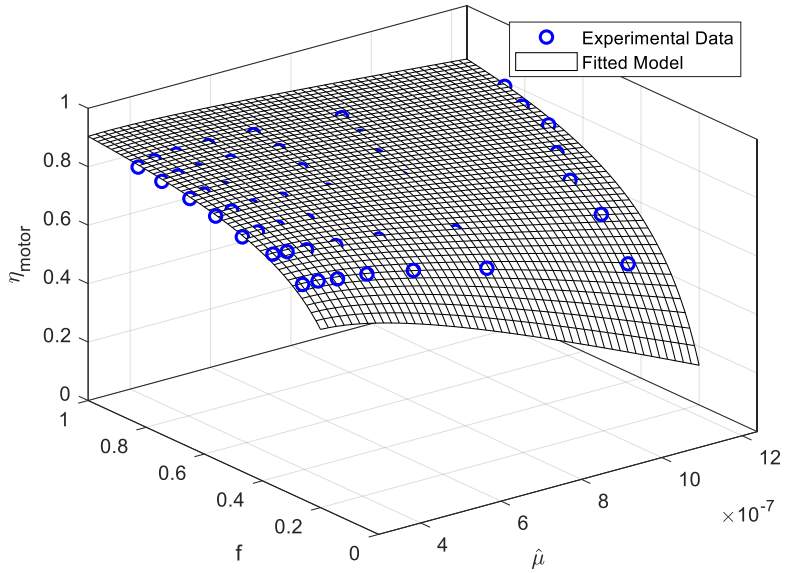

Figure 48: HST motor's overall efficiency data and fitted model

The overall HST efficiency is,

$$\eta_{HST} = \eta_{pump}\eta_{motor} \tag{31}$$

Then, an experimental validation was performed under different operating conditions [43]. The results are shown below in Figure 49. The first conditions tested were 72 bar pressure, 0.40 motor displacement, and 2.72 rad/s pump speed. Optimal viscosity was predicted at 17.1 cSt; the results are shown in Figure 49 (a). The second conditions tested were 90 bar pressure, 0.61 motor displacement, and 4.18 rad/s pump speed. Optimal viscosity predicted at 19.1 cSt; the results are shown in Figure 49 (b). The third conditions tested were 130 bar pressure, 0.37 motor displacement, and 2.6 rad/s pump speed. Optimal viscosity predicted at 31.4 cSt; the results are shown in Figure 49 (c). The fourth conditions tested were 188 bar pressure drop, 0.46 motor displacement, 3.35 rad/s pump speed. Optimal viscosity predicted at 43.1 cSt; the results are shown in Figure 49 (d)

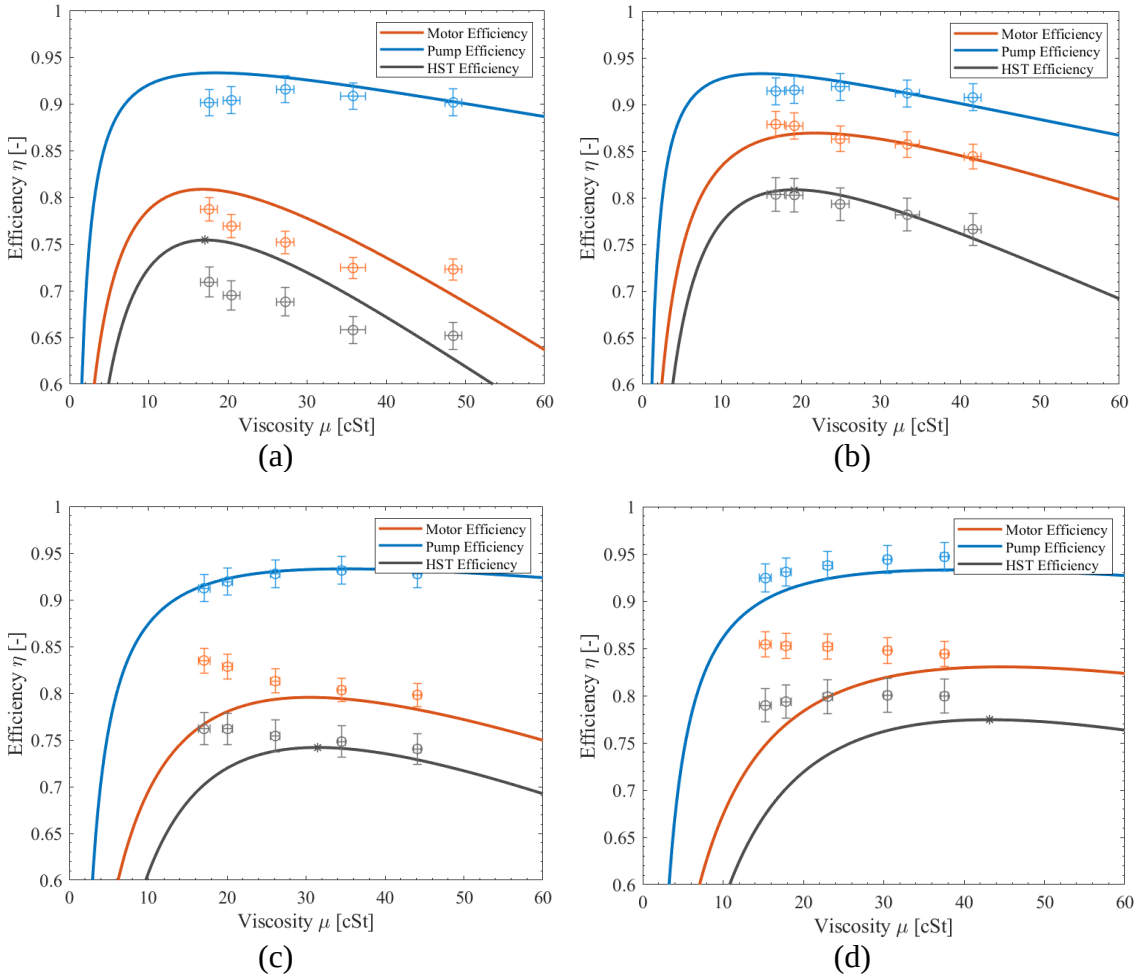

Figure 49: Experimental Validation under four different conditions [43]. *Error bars are 95% confidence intervals for the measurements propagated from statistical and systematic uncertainties of sensors.

4.1.2. Simplified Heat Exchanger Model

The HST test stand has a counterflow heat exchanger to maintain the hydraulic oil's temperature to a set value. A schematic of the heat exchanger integrated with the hydraulic components is shown in Figure 50.

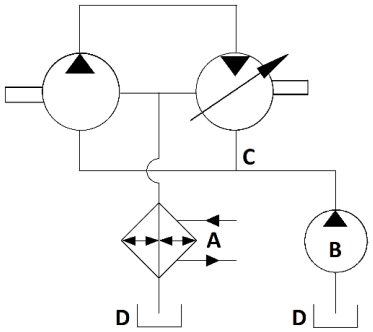

Figure 50: Heat exchanger schematic [43]

The counter-flow heat exchanger (A) is connected in series to the case drain leakage flow from the pump and motor. A charge pump (B) replenishes fluid back to the transmission loop from the reservoir (D). Thermocouples are installed at the HST low and high-pressure lines (C). The temperature can be controlled by adjusting the chilled water flow through the heat exchanger with a proportional electro-valve.

The heat exchanger can be modeled as a second-order system with a time delay. Figure 51 shows the system's response used for system identification.

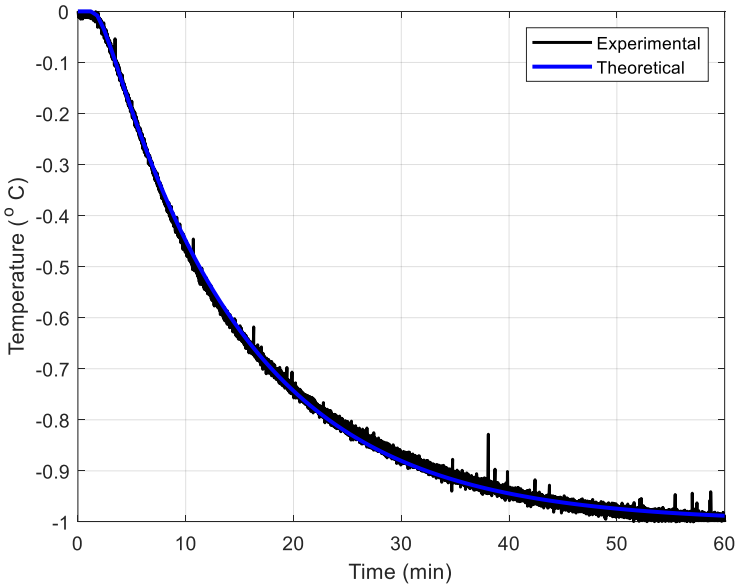

Figure 51: Open-loop system characterization

The open-loop transfer function of the system is,

$$\frac{X_1(s)}{U(s)} = \frac{T}{V} = \frac{-2.55 \times 10^{-5}\, e^{-80s}}{s^2 + 0.02131s + 2.55 \times 10^{-5}} = \frac{-ke^{-80s}}{(49.90s + 1)(785.74s + 1)} \qquad (32)$$

This simplified model is used to tune and test the controllers in the following sections. It is also coupled with the HST and viscosity models presented earlier. This is a simplified model because it does not consider changes in temperature due to the power. As the power increases, the system heats up faster, and as the power decreases, the system heats up slower. However, the simplified model serves as a good starting point for the design of the controllers.

Coupling the three models is used for preliminary evaluation of the efficiency changes in the system. A schematic of the coupled HST-efficiency-heat exchanger model is shown in Figure 52.

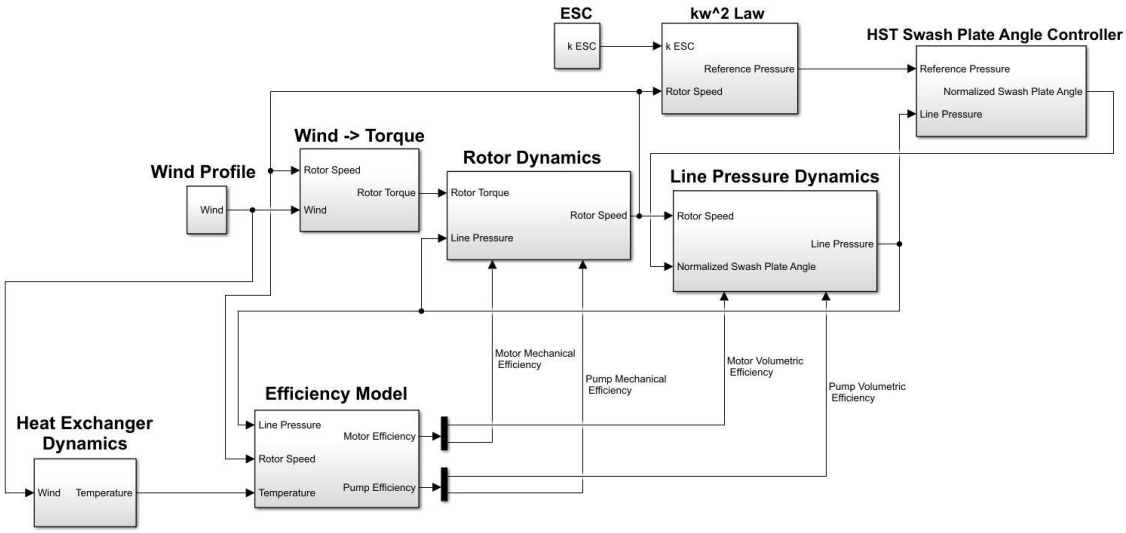

Figure 52: Integrated HST-efficiency-heat exchanger models

The heat exchanger model takes the wind as an input and uses a relationship between the wind speed and the temperature to set the ideal value. This relationship is found by running

a hill-climbing optimization where the objective function is the efficiency, and the variable being tuned is the temperature. The controllers are designed to find the reference value as fast as possible.

4.1.3. Proportional plus Integral (PI) Control

A classical proportional plus integral (PI) controller is proposed. A PI controller is proposed first because the classical approach is always easy to implement and evaluate. The general form of the PI controller in the Laplace domain is,

$$C(s) = K_p + \frac{K_i}{s} \tag{33}$$

The controller gains K_p and K_i are tuned first using the ultimate sensitivity method proposed by Zeigler-Nichols, summarized in [67], and later fine-tuned to reduce the inherent transients of this tunning strategy. This method evaluates the amplitude and frequency of the oscillations when the system is marginally stable. To do so, the proportional gain, K_p is increased until this condition is met. Then, using this gain, typically called K_u and the period of oscillation, P_u, of the marginally stable response, the tuned gains for the PI controller can be calculated as follows, $K_p = 0.45K_u$ and $K_i = 0.54\frac{K_u}{P_u}$.

The main problem with the PI controller is its unreliability in uncertain conditions. Because the model is simplified, any variations on the existing system may destabilize the response. Hence, the need for a robust controller like the one presented in the following section. Also, in this case, the control input gets saturated often, which means that there is an undesirable integrator wind-up.

4.1.4. Sliding Mode Control (SMC)

A Sliding Mode Control (SMC) strategy is proposed. SMC is a popular control strategy, and this chapter's approach to SMC is based on the work of Slotine [68]. SMC is a nonlinear robust control strategy that drives the system to respond quickly while keeping the computational effort low. The SMC forces the states to reach a sliding surface and stay on it. There are two essential points for designing an SMC:

- designing a suitable sliding surface, S.
- designing a control law, u, that drives the states to the sliding surface, S, and that guarantees that S^2 remains a Lyapunov-like function for stability.

The simplified linear system evaluated has the following form,

$$\begin{aligned} \dot{x}_1 &= -\frac{x_1}{785.74} - \frac{k_1 x_2}{785.74} \\ \dot{x}_2 &= \frac{-x_2 + u}{49.9} \end{aligned} \tag{34}$$

For reference tracking, the sliding surface, S, equation (35), is defined based on the error, $\tilde{x}$, between the desired trajectory, r, and the measured state, x_1, equation (36).

$$S(\tilde{x}, \dot{\tilde{x}}) = \lambda \tilde{x} + \dot{\tilde{x}} \tag{35}$$

Where λ is a strictly positive constant, and $\tilde{x}$, $\dot{\tilde{x}}$ are the error and its derivative with respect to time.

$$\tilde{x} = r - x_1 \tag{36}$$

In this case, r is the reference temperature, and x_1 is the measured temperature.

The sliding surface is required to be asymptotically stable. This condition holds because equation (35) is a first-order homogenous linear differential equation with a solution of the

form $\tilde{x} = Ce^{-\lambda t}$, where C is a constant dependent on initial conditions. In other words, as $S \to 0 \Rightarrow \tilde{x} \to 0$ and $\dot{\tilde{x}} \to 0$. It also means that as $S \to 0 \Rightarrow x_1 \to r \Rightarrow \tilde{x} \to 0$, meaning that there is no steady-state error.

To keep a $S = 0$ a control law u needs to be chosen, such that outside of $S(t)$, the sliding condition, equation (37), is met.

$$\frac{1}{2}\frac{d}{dt}S^2 \leq -\eta|S| \tag{37}$$

Where η is a positive constant. As explained in [68], "… equation (37) states that the squared "distance" to the surface as measured by S^2, decreases along all system trajectories…" , i.e. if the sliding condition is met, then the system is stable and in sliding mode pointing towards the surface, as illustrated in Figure 53.

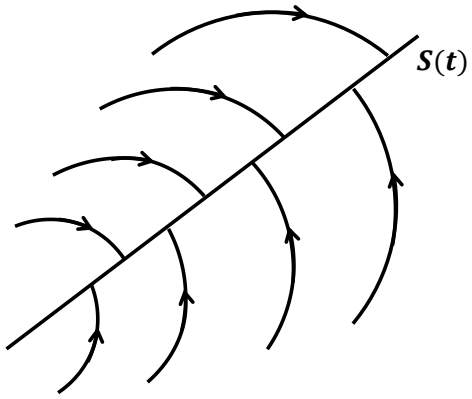

Figure 53: The sliding condition

The dynamics of the sliding surface are $\dot{S} = 0$.

$$\dot{S} = 0 \to 0 = \lambda(\dot{r} - \dot{x}_1) + \ddot{r} + \frac{\dot{x}_1}{785.74} + \frac{k_1}{785.74}\left(\frac{-x_2 + \hat{u}}{49.9}\right) \tag{38}$$

From the sliding surface dynamics, the equivalent control $\hat{u}$ is found. $\hat{u}$ is the best estimate of a control law if the system's dynamics are precisely known. With this, a control law, u, equation (39), is designed to bring the states to the sliding surface and to keep them on the surface.

$$u = \hat{u} + u_{sw} \tag{39}$$

$u_{sw} = -k_{SMC} sgn(S)$ is designed to satisfy equation (37), and it is called the switching control law. The discontinuous term $sgn(S)$ allows the system to behave as a Lyapunov-like function of the closed-loop system, helping avoid disturbances and system parameter uncertainty. The constant k_{SMC} is designed to guarantee that the parametric uncertainties do not affect the stability of the closed-loop system by ensuring that equation (37) holds.

Based on the previous explanations, the initial control law found for the proposed system has the form,

$$u = A\dot{x}_1 + Bx_2 - k_{SMC} sgn(S) \tag{40}$$

Where $A = 4.5$ and $B = 1$ are constants dependent on the system dynamics, k is a positive control tunning constant, and sgn is the signum function, Figure 54 (left), which is defined as,

$$sgn(x) = \begin{cases} -1 \; if \; x < 0 \\ 0 \; if \; x = 0 \\ 1 \; if \; x > 0 \end{cases} \tag{41}$$

A commonly known problem of SMC is chattering. Chattering happens because the switching law only has two states due to the signum function. Chattering can be acceptable in some instances, but generally, it is detrimental to the actuator because of high actuator activity and because the response will show undesirable high-frequency behavior. Other

switching laws are proposed to overcome chattering. Using a saturation function, Figure 54 (right), instead of a signum function is a common way of solving the chattering problem.

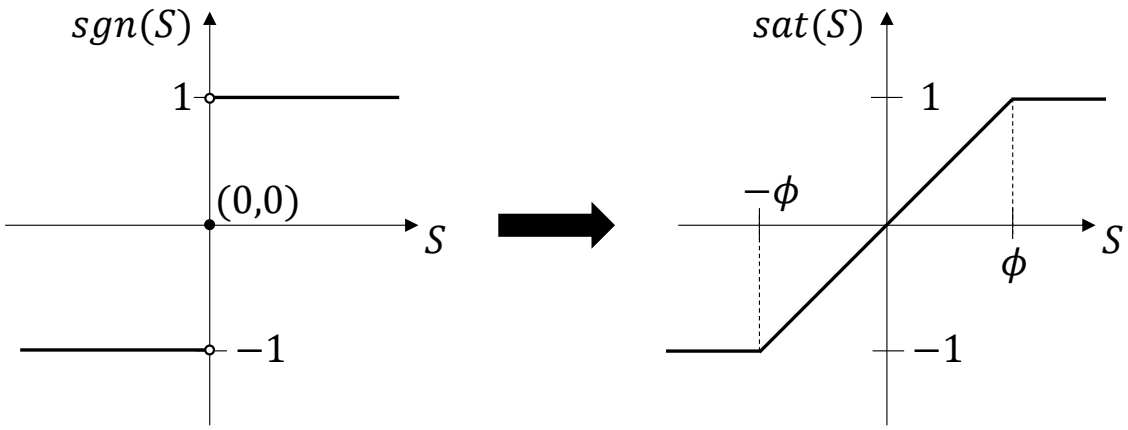

Figure 54: (left) Signum function. (right) Saturation function

The saturation function is defined as,

$$sat(S) = \begin{cases} -1 & if \quad S < -\phi \\ \dfrac{S}{\phi} & if \quad -\phi \leq S \leq \phi \\ 1 & if \quad S > \phi \end{cases} \tag{42}$$

This function opens the possibility of having a boundary layer, ϕ, where the control law will not switch from positive to negative values. It operates by interpolating within the boundary layer, so the control signal is continuous and not discrete. When using a saturation function instead of a signum function, then $u_{sw} = -k_{SMC} sat\left(\frac{S}{\phi}\right)$ with equation (40) turning into equation (43).

$$u = A\dot{x}_1 + Bx_2 - k_{SMC} sat\left(\frac{S}{\phi}\right) \tag{43}$$

In summary, the general idea behind sliding mode control is to select a sliding surface, S, and then select the feedback control law u_c such that S^2 remains a Lyapunov-like function

of the closed-loop system regardless of the presence of model uncertainty and disturbances [68].

4.2. Results and Discussion

4.2.1. Simulation Studies

Both control strategies are evaluated in simulations, and the best controller is chosen for experimental validations.

A step-up and step-down in temperature compare the responses of the PI controller and the SMC. First, a comparison between the SMC without anti-chattering and the PI controller is presented. The results are shown in Figure 55.

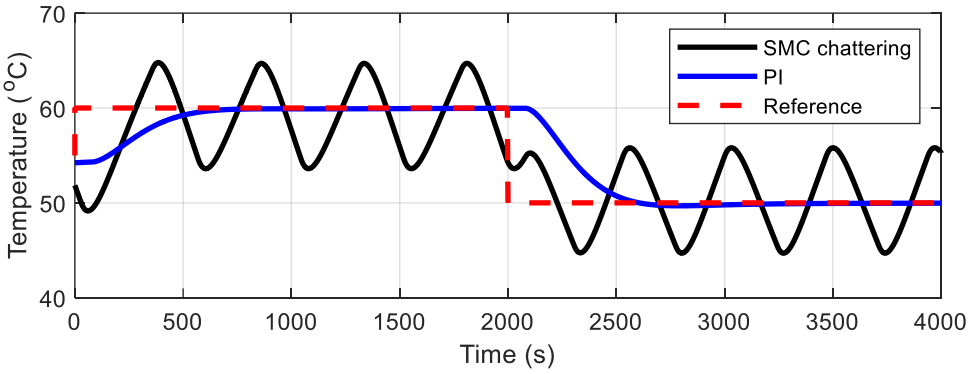

Figure 55: Comparison between PI and SMC controllers

The parameters for the PI controller and the SMC are given in Table 5.

Table 5: PI and SMC parameters

Controller	Parameters
PI	$K_p = -0.253204$ $K_i = -0.000343$
SMC	$\lambda = 1$ $K_{SMC} = 10$

It is tempting to prefer a PI controller because of its smooth response. But the chattering can be attenuated by adding a boundary layer to the SMC. The results are shown in Figure 56.

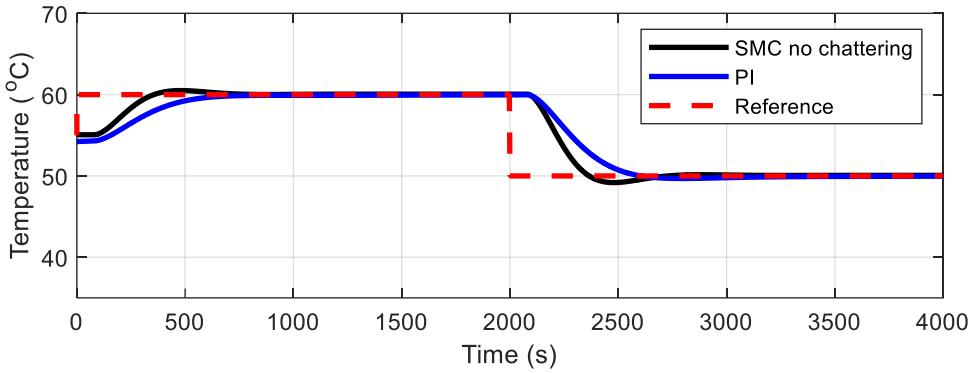

Figure 56: Comparison between PI and SMC controllers. SMC response shown after implementing the anti-chattering strategy

The parameters for the PI controller and the SMC with a boundary are given in Table 6.

Table 6: PI and SMC with boundary parameters

Controller	**Parameters**
PI	$K_p = -0.253204$ $K_i = -0.000343$
SMC	$\lambda = 10.5$ $K_{SMC} = 35$ $1/\phi = 1/800$

Because implementing the anti-chattering strategy is simple and does not require significant changes to the controller, it is a solution that is worth implementing. It also means that the controller will be robust to uncertain parameters and respond faster than the proposed PI controller solution.

Other strategies like Model Predictive Control could also work for quicker responses, but at the cost of high computational efforts and robustness depending on an accurate plant model.

4.2.2. Experimental Studies

4.2.2.1. Viscosity Boundary

When running experimental validations, it is essential to account for the system's limitations. In the case of the HST, there is a viscosity limitation with the hydraulic pump (Hagglunds $2500\ cc/rev$ unit). The manufacturer is explicit about maintaining an oil viscosity higher than $32\ cSt$ to guarantee that the unit operates optimally for its intended lifetime [69]. Because of this, a bounding temperature algorithm is implemented. The algorithm uses the relationship between viscosity, temperature, and pressure, equation (44), to set a bound on the temperature. This equation is taken from the ISO 2909 (Standard Practice for Calculating Viscosity Index from Kinematic Viscosity at 40 and 100°C) [70] and corrected for pressure based on [71].

$$\mu(p,T) = \left[\left(10^{(10^{(A+B\log_{10}T)})}\right) - 0.7\right] e^{1.7\times10^{-3}p} \tag{44}$$

Where A and B are constants depending on the hydraulic oil chosen, for this study, the hydraulic oil used is ISO 68, more specifically Mobil SHC 526 (VG 68) synthetic hydraulic oil. The viscosity vs. temperature vs. pressure curve is shown in Figure 57.

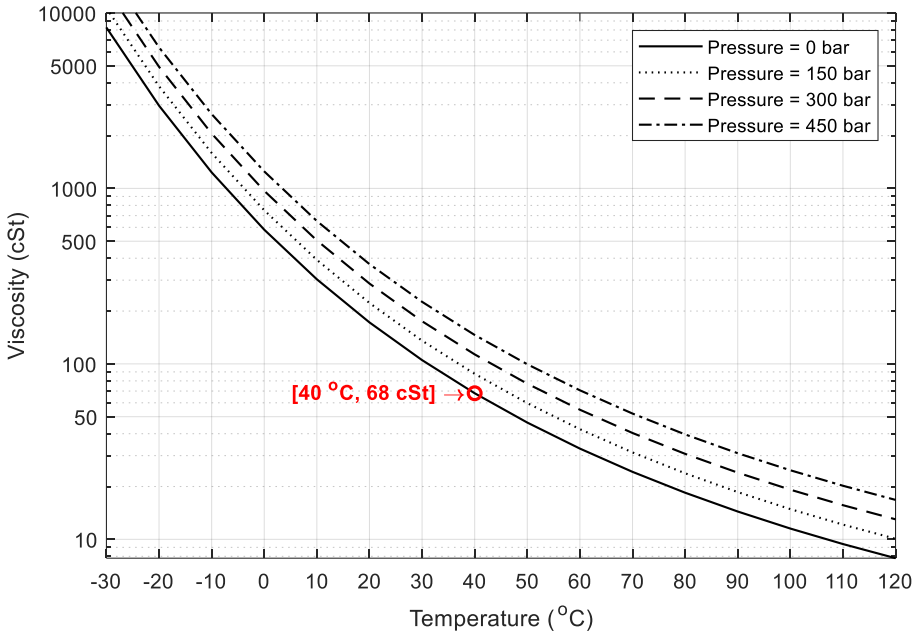

Figure 57: ISO 68 viscosity vs. temperature vs. pressure curve.

The $pressure = 0\ bar$ case is the characteristic curve for the ISO 68 oil, where the viscosity is 68 cSt at 40 °C as demarked on the figure.

Then based on equation (44), the bounding equation is,

$$T(p) = 10^{\frac{\mu_{32}(p)-A}{B}} - 273.15 \tag{45}$$

Where $\mu_{32}(p)$ is the viscosity of the fluid as a function of the pressure when the viscosity without a pressure correction is set to 32 cSt, and is defined by,

$$\mu_{32}(p) = \log_{10}\left[\log_{10}\left(\frac{32}{e^{(1.7\times10^{-3}p)}} + 0.7\right)\right] \tag{46}$$

This algorithm is implemented on the HST test stand, and its operation is shown later in this chapter.

4.2.2.2. Kalman Filter

One of the biggest challenges in validating the results comes from noisy signals and the fact that no measurements are available for one of the states of the system (x_2). This state is necessary to implement the SMC designed for the temperature control system, as seen in equation (43). An optimal observer (Kalman Filter) was implemented to overcome these two problems, Figure 58. The state-space model of the system is:

$$\begin{bmatrix}\dot{x}_1\\ \dot{x}_2\end{bmatrix} = \begin{bmatrix}-\frac{1}{785.74} & -\frac{47.0748}{4455}\\ 0 & -\frac{1}{49.9}\end{bmatrix}\begin{bmatrix}x_1\\ x_2\end{bmatrix} + \begin{bmatrix}0\\ \frac{1}{49.9}\end{bmatrix}u \tag{47}$$

$$y = [1 \quad 0]\begin{bmatrix}x_1\\ x_2\end{bmatrix} + [0]u$$

The Kalman Filter's block diagram is shown below.

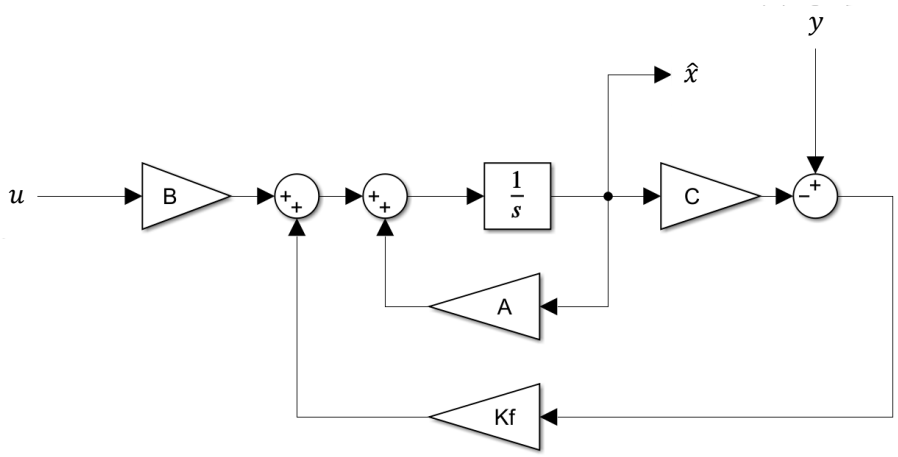

Figure 58: Kalman Filter block diagram with input, u, on the left, estimated states, $\hat{x}$, in the middle, and output of the system, y, on the right.

The Kalman Filter estimates the desired states used on the SMC, and the estimates are used instead of the measured states. It can be shown that if the observer states make the estimated surface $S_e \rightarrow 0$, then the actual surface $S \rightarrow 0$ [68]. The filter gain is obtained based on the state-space model of the heat exchanger, the noise's covariance, and the disturbance's

covariance. The covariances were found from experimental results obtained on the HST test stand at the University of Minnesota. The MATLAB® code used to calculate these is shown in Appendix b.2. The gains are then calculated by solving the Algebraic Riccati Equations using MATLAB®. The gains are, $Kf = [0.9979778, 1.7346096 \times 10^{-18}]$. A comparison between the measured data and the estimated data for the temperature is shown in Figure 59.

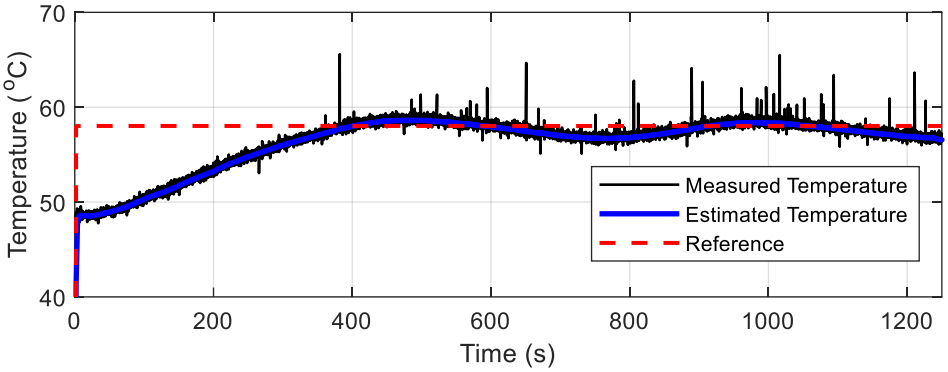

Figure 59: Measured vs. Estimated Temperature

4.2.2.3. Validating the Performance of SMC

Dynamic temperature control was compared to constant temperature control of $55\,°C$. $55°C$ is chosen based on component manufacturer specifications. Two studies were conducted for two controller cases. First, a $1\ m/s$ step down in the wind is introduced at $2000\ s$, Figure 60 top. In the first study, the controller (controller case 1) was tuned to obtain a smoother transient behavior, sacrificing the steady-state error. Second, a $1.5\ m/s$ step down in the wind is introduced at $2000\ s$, Figure 60 bottom. In the second study, the controller (controller case 2) was tuned to reduce the steady-state error, sacrificing the smoother transient behavior. The step size was changed to show the disturbance rejection capabilities of both controllers.

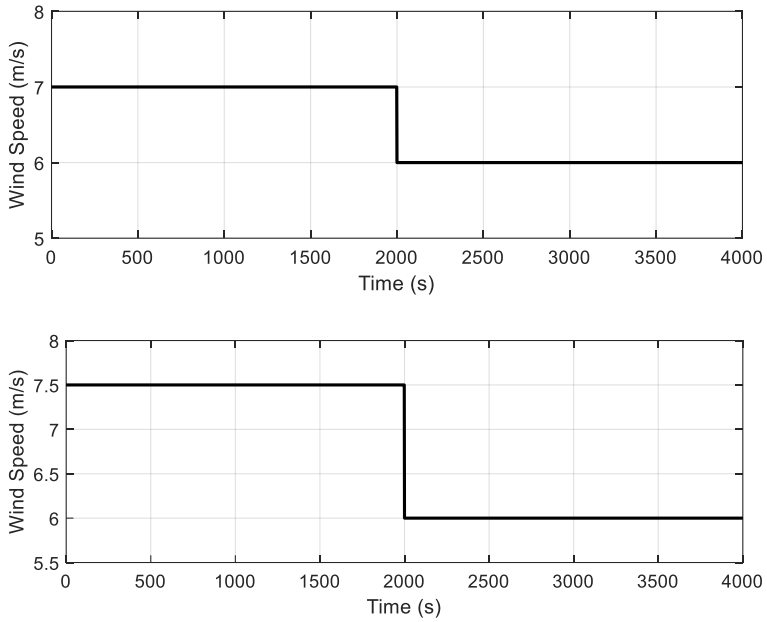

Figure 60: Step wind profile used for the experimental studies

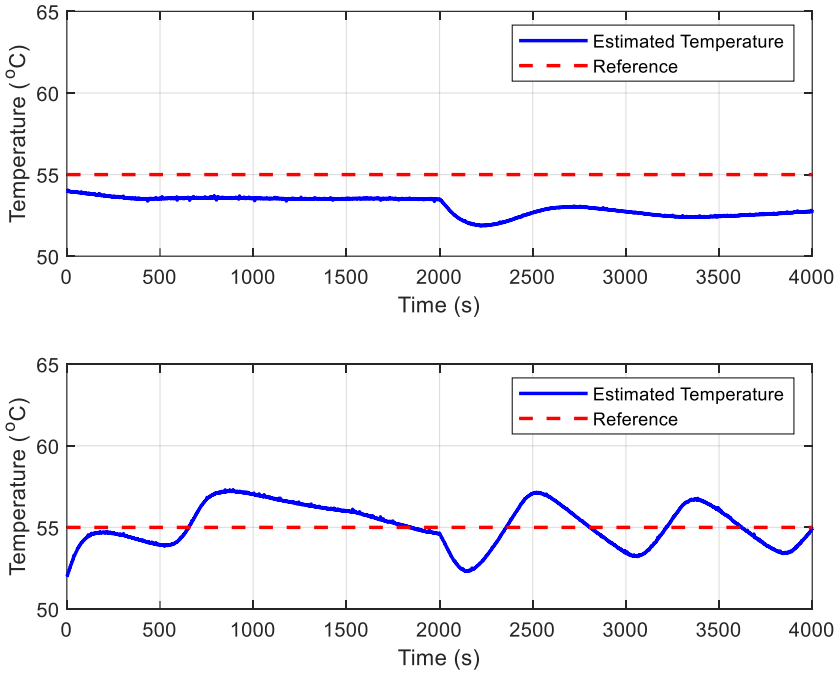

Figure 61: Constant temperature responses under two wind step conditions and two controller cases. On the top, wind step down of 1 m/s at 2000 s for controller case 1. On the bottom, wind step down of 1.5 m/s at 2000 s for controller case 2.

The first case shows the response of controller case 1 with a smoother transient response. The main concern is the steady-state error, which will impact the final efficiency of the system. One way to overcome this is by introducing an integrator. The integrator introduces an extra state to the sliding surface and eliminates the steady-state error. However, this will also introduce more oscillations, leading to a response similar to the one obtained in controller case 2.

The second study shows the response of controller case 2 with a small steady-state error but more considerable oscillations. These oscillations become smaller with time and vary depending on the wind speed. One way to overcome this is by using a time-changing boundary on the sliding surface. If the boundary adapts with time, the controller will have transient behaviors better suited to each situation [68]. The results obtained for the dynamic temperature control are shown in Figure 62.

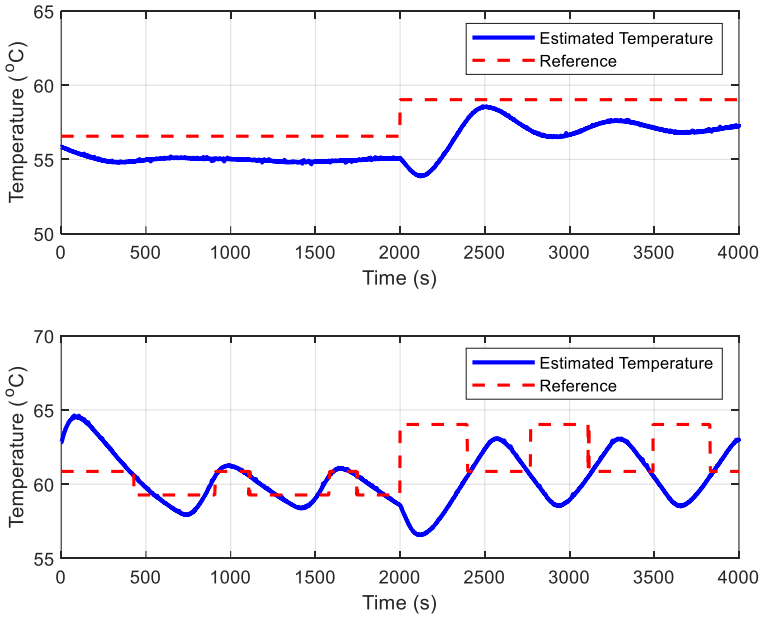

Figure 62: Dynamic temperature responses under two wind step conditions and two controller cases. On the top, wind step down of 1 m/s at 2000 s for controller case 1. On the bottom, wind step down of 1.5 m/s at 2000 s for controller case 2.

Controller cases 1 and 2 are evaluated as in the constant temperature study. This study shows controller behaviors similar to those in the constant temperature study. One thing to note is that for controller case 2, due to the high amplitude of the transients, the viscosity boundary algorithm kicks in, which is why the reference temperature is constantly changing over time.

The instantaneous efficiency for the dynamic and constant temperature studies for both controller cases is shown in Figure 63.

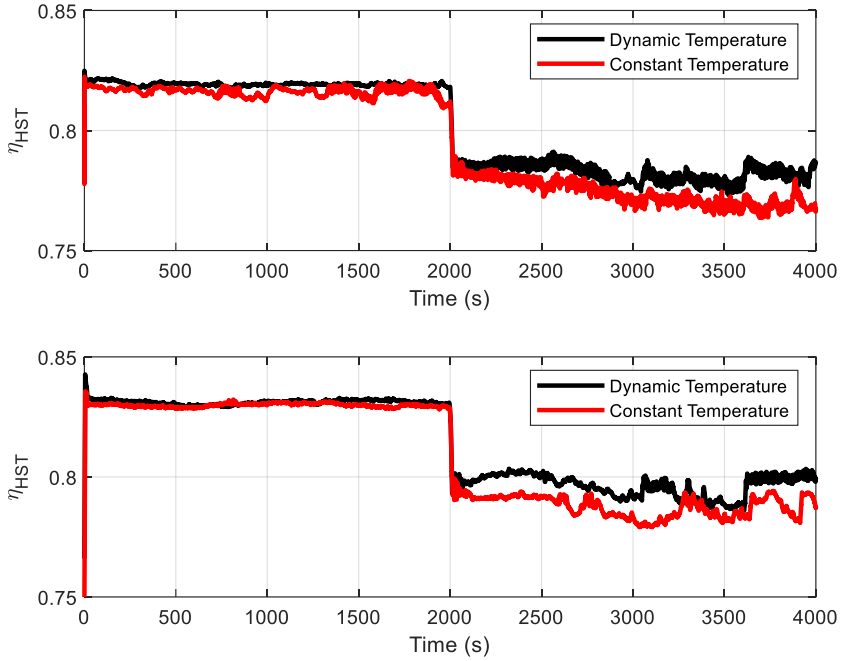

Figure 63: Instantaneous HST efficiency comparison for the dynamic and the constant cases

The average constant and dynamic temperature efficiencies are calculated using equation (48).

$$\bar{\eta}_{HST} = \frac{\bar{\tau}_{in}\bar{\omega}_{in}}{\bar{\tau}_{out}\bar{\omega}_{out}} \tag{48}$$

Where $\bar{\tau}_{in}$, $\bar{\tau}_{out}$ are the measured average input and output torques and $\bar{\omega}_{in}$, $\bar{\omega}_{out}$ are the measured average input and output angular velocities. This equation can also be used for finding the average efficiency for each wind speed instead of the whole experiment.

The results show an average improvement in the efficiency of less than 1%. The efficiency improvement is due to the difference between the $\bar{\eta}_{HST}$ for the dynamic temperature and the $\bar{\eta}_{HST}$ for the constant temperature. If this difference is positive, efficiency is improved. When considering the $4000\ s$ of data, there is an efficiency improvement of 0.57% for controller case 1 and 0.4933% for controller case 2. However, the best comparison is for the efficiencies after $2000\ s$, where the wind speeds are the same in both studies. In that case, there is an efficiency improvement of 0.8475% for controller case 1 and 0.8702% for controller case 2. These improvements are less than expected but also show the potential of using a dynamic temperature control of the hydraulic oil.

Multiple observations can be found for each wind speed controller. First is the importance of not having a steady-state error. In both studies for both controller cases, the efficiency is improved by having a controller that can track the temperature better. Second is that high amplitude oscillations do not significantly affect efficiency. Third, it can be advantageous to use dynamic temperature control even with the small percentages shown in these two studies. There are higher and lower wind speeds to be explored, meaning a higher deviation from the constant case. Even if the constant temperature is chosen to be another value, there will always be deviations as the wind varies, especially in lower frequency changes such as night and day winds or simply windy versus regular days. Fourth, it only requires

software adjustments, and any improvement in the transmission's overall efficiency translates into more power captured by the wind turbine. Fifth, having a system that responds faster to temperature commands would likely help with better total efficiency improvements; the quicker it reaches the optimal temperature, the longer the system will operate under optimal conditions. Last, it also leads to future studies for speed-down HSTs, where the high-speed shaft could rotate at lower speeds than for the wind turbine case or even be variable, opening more opportunities for improvement.

A controller case 3 under the second wind study was evaluated. This controller includes an integrator and a more larger boundary layer than controller case 2. The reason to include an integrator is that increasing the boundary increases the steady-state error. If an integrator is included, then the boundary can be increased to reduce high-amplitude oscillations without affecting the steady-state error. The main difference in the controller is the sliding surface, which is now defined as,

$$S = \dot{\tilde{x}} + 2\lambda\tilde{x} + \int_0^t \tilde{x} \tag{49}$$

After redefining the sliding surface, the same process shown in section 4.1.4 can be repeated to find the controller input, u.

The temperature response for controller case 3 is shown below in Figure 64

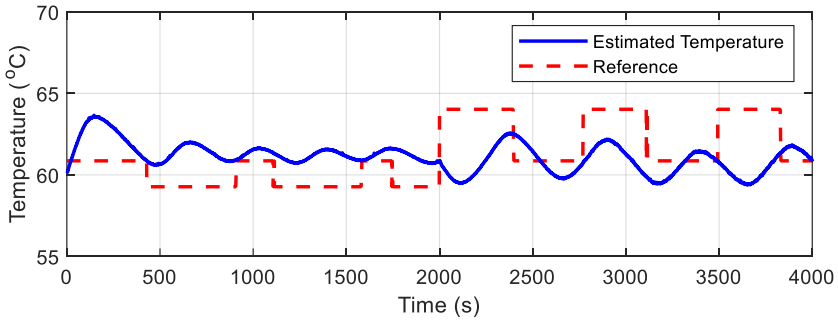

Figure 64: Dynamic temperature responses for controller case 3. Wind step down of $1.5\ m/s$ at $2000\ s$.

In this study, because both controllers were tested under the same wind speeds, it is fair to compare the average efficiencies throughout the $4000\ s$. The average efficiency for controller case 2 is 81.38%. The average efficiency for controller case 3 is 81.34%. This confirms the results obtained earlier, where it was concluded that high amplitude oscillations would not affect the overall efficiency as much as a high steady-state error. The main advantage of using controller case 3 is a smoother temperature response, which translates into a smoother instantaneous efficiency, as seen in Figure 65.

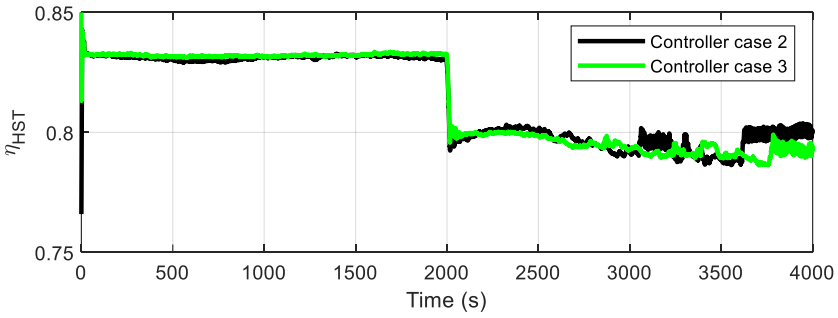

Figure 65: Instant HST efficiency comparison for controller cases 2 and 3

4.3. Conclusion

This study investigates the potential benefits of implementing active temperature control of hydraulic oil in an HST to improve its efficiency. To do this, a simplified efficiency

model of the HST was first created and validated through experiments. This model was then integrated into simulations of the HST system, along with a simplified heat exchanger model, to evaluate the effects of dynamic temperature control. Two control strategies were proposed for temperature control: a classical PI controller and a robust nonlinear SMC. Both controllers were evaluated through simulations, and the SMC was chosen for further experimentation due to its robustness and fast response time. Finally, the two controller cases were tested experimentally under constant and active temperature reference. The results showed that the efficiency improvements from the temperature control strategies were less than 1%. However, this approach is still of interest because it only requires software changes and can be implemented in speed-down transmissions.

Chapter 5

Conclusions and Future Work

5.1. Conclusions

Wind turbines have used gearbox transmissions as the primary solution to speed up the low rotations of the blades' rotor. This research expands on the idea of using hydrostatic transmissions as an option to replace gearboxes on midsize wind turbines of the community wind sector. HSTs are continuously variable transmissions with a high power-to-weight ratio and reliability. They have been used for demanding mining, agriculture, and fishing applications. This is why HSTs are a suitable contender for gearboxes on midsize wind turbines. In contrast, HSTs are not as efficient as mechanical gearboxes. However, when used for a wind turbine, the turbine's efficiency is comparable with either transmission. Three ideas are proposed to improve the efficiency of HSTs to make them more competitive.

First, we have explored the opportunity to harvest more wind power by oscillating wind turbine blades. The study compared, through simulations, the power captured by static pitch wind turbine blades to the power captured by oscillating the pitch of wind turbine blades. We used CFD analysis combined with Blade Element Momentum Theory to calculate the power ratio. For the first stage of the study, it was found that oscillating the blades with a tilted sinusoid improved the overall performance compared to oscillating the blades with a sinusoid wave. This was evident when comparing the lift-to-drag ratio

between the two waveform inputs. For the second stage of the study, an optimization of the oscillating conditions was proposed. The optimization showed that the overall performance of the oscillating case was never higher than the overall performance of the static case. For optimal conditions, the oscillating blade could only produce 89.77% of the power produced by the static blade. This is mainly because of the drag forces present in the system and because you must input extra power into the system to oscillate the blades.

Second, an ESC for a 60-kW hydrostatic wind turbine is implemented and compared to a baseline controller. The study first shows simulation results and then experimental validations at the power regenerative test stand of the University of Minnesota. When operating under ideal conditions ($\lambda_* = 6.5$) the ESC can match the baseline controller's performance. When operating under the modified cases ($\lambda_* = 5.5$, λ_*=4.5, and $\lambda_* = 7.5$) the ESC consistently outperforms the baseline controller. The change in the C_p vs. λ curve affects the performance of the ESC in different ways. The more significant the change from the ideal case, the longer the ESC takes to find an optimal torque gain. The curvature affects the performance of the ESC, with a higher curvature giving the best results. In general, the proposed adaptive controller achieves the desired goal of finding an optimal torque control gain if the C_p vs. λ curve changes in time both in simulation and experimentation.

Third, dynamic temperature control of the hydraulic oil is implemented to improve the efficiency of the HST. First, a simplified efficiency model of the HST is created and validated through experiments. Then this model is integrated into the HST simulations with a simplified heat exchanger model to evaluate the dynamic temperature control. Two

control strategies are proposed to control the temperature: a classical PI controller and a robust nonlinear SMC. The performance of both controllers is evaluated through simulations. The SMC is chosen to be used in experiments because of its robustness and high-speed response. Finally, two controller cases are evaluated experimentally for a constant temperature reference case and a dynamic temperature control case. The comparisons show efficiency improvements of less than 1%. However, this idea is still interesting because it only requires software changes and can be implemented for speed-down transmissions.

5.2. Future Work

5.2.1. Improvements to the ESC

Lead-lag compensation is often used to decrease the response time of a dynamic system. For an ESC, the optimization could be faster if the power response is faster. We propose introducing a compensator before the high-pass filter of the ESC scheme. This would imply a recalibration of the ESC parameters due to the additional dynamics introduced by the compensator. However, if there is a chance of improving the optimization time, the gains in power capture can be increased.

The ESC can also be improved by introducing rotor torque estimation. Rotor torque is required to compute the power in the turbine's rotor. In the current experimental test stand, the torque in the rotor is available because it is a research setup, and the system is highly instrumented. In real-life conditions, a torque sensor that could measure such high torques would be impractical and would bring the overall cost of the system up. This could also lead to using other control strategies that use the torque estimate to find the correct command to optimize power capture. That is the case for the rotor speed control proposed by Chapple [17]. In their case, the reference is based on the optimal tip speed ratio (TSR), λ_*. The TSR depends on the wind speed, the rotor's speed, and the rotor's diameter. The optimal value could be found by using ESC to adapt to the changing R and a torque estimator to calculate the wind speed.

5.2.2. Detailed Heat Exchanger Model

The proposed second-order dynamic system with a time delay does not capture the system's actual dynamics, mainly because the temperature change is also a function of the power. If

the power is high, the system can heat up faster (or it is harder to cool down). Similarly, if the power is low, the system can cool down faster (or it is harder to heat up). Also, this is a fitted model, and it is not based on the physics related to the heat exchanger. An extension of the model proposed by Franklin [67], equation (50), is an excellent start to approach this problem. A schematic of a counterflow heat exchanger is shown in Figure 66.

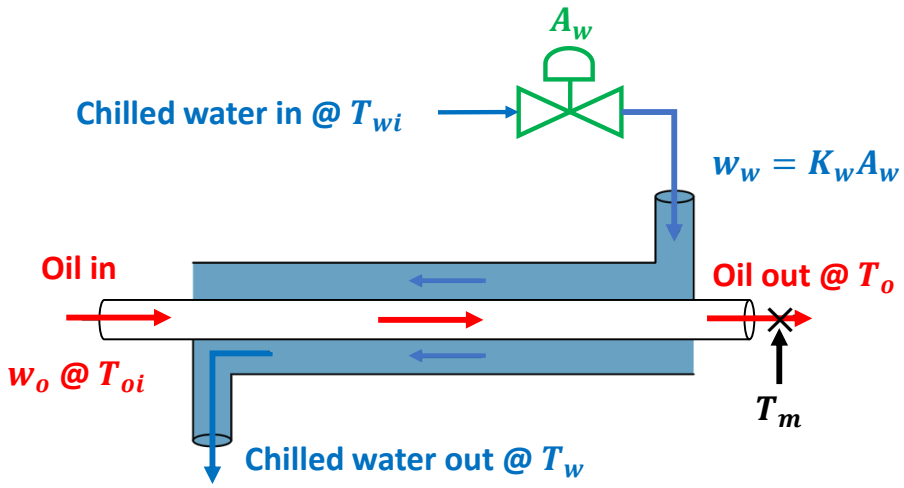

Figure 66: Counter flow heat exchanger

Here chilled water enters through the controllable valve at the top. There is a constant flow of oil through the pipe to be cooled down by the chilled water. The differential equations that describe the dynamics of the measured output temperature, T_m, as a function of the area A_w from the control valve can be described by equation (50). The temperature sensor at the oil output, lags the temperature by t_d seconds.

$$\begin{aligned} C_o\dot{T}_o &= w_o c_{co}(T_{oi} - T_o) - \frac{1}{R}(T_w - T_o) \\ C_w\dot{T}_w &= K_w A_w c_{cw}(T_{wi} - T_w) + \frac{1}{R}(T_w - T_o) \\ T_m(t) &= T_o(t - t_d) \end{aligned} \tag{50}$$

Where C_o and C_w are the thermal capacities of the oil and the water, w_o and w_w are the mass flow rates, c_{c0} and c_{cw} are the specific heats, T_{oi} and T_{wi} are the input temperatures, T_o and T_w are the output temperatures, R is the thermal resistance equation describing what the oil temperature is. This is a nonlinear model because the input, A_w, is multiplying one of the two states of the system, T_w. The model can be extended by introducing a heat source term, meaning that heating happens at a different rate than cooling. This nonlinear model would be experimentally validated on the test stand at the University of Minnesota.

The model could be used to test realistic wind conditions and different methods to cool down or heat the oil. Other extensions can be added, like the oil tank dynamics. These would help us understand the effects of changing the tank size in the hydraulic circuit. This is more than a control problem; it is also a design problem. The system should be redesigned to respond faster and consider real-life wind turbine conditions. Until this point, the system was analyzed with a big tank not optimally designed for active temperature control. It also uses chilled water, typically unavailable at wind turbine sites. Winter conditions are also a challenge for heating the oil; similarly, summer conditions for cooling it down.

5.2.3. Optimal Viscosity Study for a Speed-Down HST

An extension to a speed-down HST should be evaluated based on the results obtained from the speed-up HST. The operating conditions for a speed-down HST are more conventional for typical applications such as off-road vehicles and agricultural equipment. These operate under lower shaft speeds and higher pressures, so the opportunity to vary the temperature

becomes more beneficial. The HST studied comprises a variable displacement pump and a fixed displacement motor Figure 67.

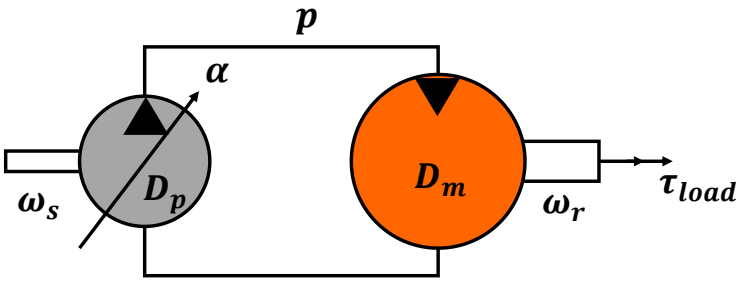

Figure 67: Speed-down HST schematic

The dynamics depend on the rotor dynamics and the pressure dynamics. The equation of motion for the rotor dynamics is,

$$\dot{\omega}_r = \frac{1}{J}(pD_m - b\omega_r - \tau_{load}) \tag{51}$$

Where J is the rotor moment of inertia, ω_r is the rotational speed of the low-speed shaft, p is the line pressure, D_m is the displacement of the motor, b is the damping of the rotor, and τ_{load} is the load torque on the low-speed shaft.

The equation of motion for the pressure dynamics is,

$$\dot{p} = \frac{B}{V}\left(D_p\alpha\omega_s - D_m\omega_r - L_d\right) \tag{52}$$

Where B is the equivalent bulk modulus, V is the volume of fluid in the hydraulic lines, α is the swash plate angle of the pump, ω_s is the rotational speed of the high-speed shaft, and L_d is the leakage loss term.

This work would start with a simplified version of the model where the high-speed shaft rotates at constant speeds and evolve to consider the more complicated, nonlinear model where the speed changes in time.

5.2.4. Integrating ESC with Dynamic Temperature Control

The focus of the thesis was to find individual strategies that would help with overall turbine efficiency improvements. Both the ESC and the dynamic temperature control showed improvements individually. A question remains whether these two control strategies would work well together. The ESC is constantly tuning the torque control gain, k, which continuously changes the reference pressure. It is essential to verify how these pressure oscillations would affect the performance of the sliding mode controller implemented for the hydraulic oil dynamic control. As mentioned, the temperature depends on the power in and out of the system. Since the pressure reference affects the torque input (power input), there might be a clear relationship between the oscillations posed by the ESC and the temperature controlled by the SMC.

Bibliography

[1] R. Wiser *et al.*, “Wind Vision: A New Era for Wind Power in the United States,” *Electr. J.*, vol. 28, no. 9, pp. 120–132, 2015.

[2] U.S. Department of Energy, “Wind Vision Report by United States Department of Energy,” 2008. https://www.energy.gov/eere/wind/wind-vision

[3] R. Wiser *et al.*, “Land-Based Wind Market Report: 2022 Edition; Executive Summary,” 2022.

[4] A. Betz, “Schraubenpropeller Mit Geringstem Energieverlust,” pp. 193–213, 1919.

[5] A. Betz, “Windenergie und Ihre Ausnutzung durch WindMüellen,” *Vandenhoeck and Ruprecht, Göettingen,* 1926.

[6] J. F. Manwell, J. G. McGowen, and A. L. Rogers, *Wind Energy Explained: Theory, Design and Application*. New York: Wiley, 2009.

[7] A. Orrell, K. Kazimierczuk, and L. Sheridan, “Distributed Wind Market Report: 2021 Edition,” 2021.

[8] K. E. Johnson, L. Y. Pao, M. J. Balas, and J. F. Lee, “Control of Variable-Speed Wind Turbines: Standard and Adaptive Techniques for Maximizing Energy Capture,” *IEEE Control Syst.*, vol. 26, no. 3, pp. 70–81, 2006.

[9] W. Short, D. J. Packey, and T. Holt, “A Manual for the Economic Evaluation of Energy Efficiency and Renewable Energy Technologies,” 1995.

[10] Y. Sheng and K. A. Stelson, “Feasibility of Hydrostatic Transmission in Community Wind Turbines,” *Submitt. to Proc. 18th Scand. Int. Conf. Fluid Power, May 30 - June 1, 2023, Tampere, Finl.*, 2022.

[11] NREL, “NREL CART Project.” http://www.nrel.gov

[12] L. Y. Pao and K. E. Johnson, “A Tutorial on the Dynamics and Control of Wind Turbines and Wind Farms,” *2009 Am. Control Conf.*, pp. 2076–2089, 2009.

[13] J. Pande, P. Nasikkar, K. Kotecha, and V. Varadarajan, “A Review of Maximum Power Point Tracking Algorithms for Wind Energy Conversion Systems,” *J. Mar. Sci. Eng. 2021*, vol. 9, no. 11, p. 1187, Oct. 2021.

[14] B. Mohanty and K. A. Stelson, “Experimental Validation of a Hydrostatic Transmission for Community Wind Turbines,” *Energies*, vol. 15, no. 1, 2022.

[15] W. Chen, Y. Lin, and X. Wang, “Review of the Application of Hydraulic Technology in Wind turbine,” no. January, pp. 1495–1522, 2020.

[16] J. A. Kovach, N. C. Lindner, B. E. Nicol, and R. D. Kimpel, “Variable Speed Wind Turbine Drive and Control System,” U.S. Patent, 7,569,943, Aug. 4 2007

[17] P. Chapple and M. O. K. Niss, “A Wind Turbine with Hydrostatic Transmission and LVRT Control,” European Patent 2,481,917, Aug. 8, 2007

[18] P. Meuser, M. Türk, and T. Pleikis, “Hydrostatic Drive of a Wind Turbine,” World Patent 2,011,003,405, Jan.13, 2011

[19] M. Umaya, T. Noguchi, M. Uchida, M. Shibata, Y. Kawai, and R. Notomi, “Wind Power Generation-Development status of Offshore Wind Turbines,” *Mitsubishi Heavy Ind. Tech. Rev.*, vol. 50, no. 3, p. 29, 2013.

[20] L. Wei, Z. Liu, Y. Zhao, G. Wang, and Y. Tao, “Modeling and control of a 600 kW closed hydraulic wind turbine with an energy storage system,” *Appl. Sci.*, vol. 8, no. 8, 2018.

[21] J. Schmitz, N. Diepeveen, N. Vatheuer, and H. Murrenhoff, “Dynamic

Transmission Response of a Hydrostatic Transmission Measured on a Test Bench," *Eur. Wind Energy Conf. Exhib. 2012, EWEC 2012*, vol. 1, pp. 197–206, 2012.

[22] J. Schmitz, M. Vukovic, and H. Murrenhoff, "Hydrostatic transmission for wind turbines - An old concept, new dynamics," *Proc. 2013 ASME/Bath Symp. Fluid Power Motion Control*, 2013.

[23] B. Mohanty and K. A. Stelson, "High Fidelity Dynamic Modeling and Control of Power Regenerative Hydrostatic Wind Turbine Test Platform," *Proc. 2018 ASME/Bath Symp. Fluid Power Motion Control*, 2018.

[24] B. Mohanty, S. Dhople, and K. A. Stelson, "A dynamical model for a hydrostatic wind turbine transmission coupled to the grid with a synchronous generator," *Proc. Am. Control Conf.*, pp. 5774–5779, 2019.

[25] R. Dutta, F. Wang, B. F. Bohlmann, and K. A. Stelson, "Analysis of Short-Term Energy Storage for Midsize Hydrostatic Wind Turbine," *J. Dyn. Syst. Meas. Control*, vol. 136, no. 1, pp. 0110071–0110079, 2013.

[26] E. B. Mohr, B. Mohanty, and K. A. Stelson, "Short-Term Energy Storage System for Hydraulic Hybrid Wind Turbine Transmission," *Proc. 2020 Bath/ASME Symp. Fluid Power Motion Control*, 2020.

[27] E. Mohr, B. Mohanty, D. Escobar-Naranjo, and K. A. Stelson, "Experimentation on a Hydraulic Energy Storage System for Mid-Size Wind Turbines," *Proc. 2021 Bath/ASME Symp. Fluid Power Motion Control*, 2021.

[28] F. Wang and K. A. Stelson, "Model Predictive Control for Power Optimization in a Hydrostatic Wind Turbine," *Proc. from 13th Scand. Int. Conf. Fluid Power, June*

3-5, 2013, Linköping, Sweden, vol. 92, 2013.

[29] D. Escobar-Naranjo, B. Mohanty, and K. A. Stelson, "Using Extremum Seeking Control to Improve the Power Capture of Midsize Hydrostatic Wind Turbines," *Proc. 2021 ASME/Bath Symp. Fluid Power Motion Control*, 2021.

[30] D. Escobar-Naranjo, B. Mohanty, and K. A. Stelson, "Experimental Validation of Extremum Seeking Control for a Midsize Hydrostatic Transmission Wind Turbine," *Proc. 2022 Bath/ASME Symp. Fluid Power Motion Control*, 2022.

[31] D. Escobar-Naranjo, J. Sampson, and K. A. Stelson, "A Study of Hydraulically Actuated Oscillating Pitch to Increase Energy Production in Wind Turbines Figure Legend :," *Proc. from 17th Scand. Int. Conf. Fluid Power, June 3-5, 2021 Linköping, Sweden*, pp. 62–73, 2021.

[32] A. Choudhry, M. Arjomandi, and R. Kelso, "Methods to Control Dynamic Stall for Wind Turbine Applications," *Renewable Energy*, vol. 86. pp. 26–37, 2016.

[33] M. J. Hoffmann, R. Reuss Ramsay, and G. M. Gregorek, "Effects of Grit Roughness and Pitch Oscillations on the S809 Airfoil." NREL/TP-442-7817, National Renewable Energy Lab, Golden, CO (United States), 1995.

[34] J. G. Leishman, "Challenges in Modeling the Unsteady Aerodynamics of Wind Turbines," *ASME 2002 Wind Energy Symp.*, vol. 132, no. November 2001, pp. 141–167, 2002, [Online]. Available: http://proceedings.asmedigitalcollection.asme.org/proceeding.aspx?articleid=1572099

[35] J. G. Holierhoek, J. B. de Vaal, A. H. van Zuijlen, and H. Bijl, "Comparing Different Dynamic Stall Models," *Wind Energy*, vol. 16, pp. 139–158, 2013.

[36] Y. Xiao, Y. Li, and M. A. Rotea, “Experimental Evaluation of Extremum Seeking Based Region-2 Controller for CART3 Wind Turbine,” *34th Wind Energy Symp.*, 2016.

[37] Y. Xiao, Y. Li, and M. A. Rotea, “CART3 Field Tests for Wind Turbine Region-2 Operation with Extremum Seeking Controllers,” *IEEE Trans. Control Syst. Technol.*, vol. 27, no. 4, pp. 1744–1752, 2019.

[38] A. Ghaffari, M. Krstić, and S. Seshagiri, “Power Optimization and Control in Wind Energy Conversion Systems Using Extremum Seeking,” *IEEE Trans. Control Syst. Technol.*, vol. 22, no. 5, pp. 1684–1695, 2014.

[39] M. E. Ibrahim, M. L. Shaltout, and S. A. Kassem, “Extremum-Seeking Control for Energy-Harvesting Enhancement of Wind Turbines with Hydromechanical Drivetrains,” *Wind Energy*, vol. 23, no. 11. pp. 2113–2135, 2020.

[40] J. Creaby, Y. Li, and J. E. Seem, “Maximizing Wind Turbine Energy Capture Using Multivariable Extremum Seeking Control,” *Wind Eng.*, vol. 33, no. 4, pp. 361–388, 2009.

[41] P. Załuski, “Influence of Fluid Compressibility and Movements of the Swash Plate Axis of Rotation on the Volumetric Efficiency of Axial Piston Pumps,” *Energies 2022, Vol. 15, Page 298*, vol. 15, no. 1, p. 298, Jan. 2022.

[42] R. Mommers, P. Achten, J. Achten, and J. Potma, “Commutation Loss in Hydrostatic Pumps and Motors,” *Proc. ASME/BATH 2021 Symp. Fluid Power Motion Control. FPMC 2021*, Dec. 2021.

[43] J. Chen, B. Mohanty, D. Escobar-Naranjo, and K. A. Stelson, “Optimizing Viscosity for Maximum Power in a Hydrostatic Transmission Wind Turbine,”

Proc. 2022 Bath/ASME Symp. Fluid Power Motion Control, 2022.

[44] P. J. Schubel and R. J. Crossley, "Wind Turbine Blade Design," *Energies*, vol. 5, no. 9, pp. 3425–3449, 2012.

[45] E. Kulunk, "Aerodynamics of Wind Turbines," in *Fundamental and Advanced Topics in Wind Power*, R. Carriveau, Ed. InTech, 2011. [Online]. Available: http://www.intechopen.com/books/fundamental-and-advanced-topics-in-wind-power/aerodynamics-of-windturbines

[46] F. Mahmuddin, "Rotor Blade Performance Analysis with Blade Element Momentum Theory," *Energy Procedia*, vol. 105, pp. 1123–1129, 2017, [Online]. Available: http://dx.doi.org/10.1016/j.egypro.2017.03.477

[47] V. Dehouck, Q. C. Jk, and J. Sacheau, "Application of the Blade Element Momentum Theory to Design Horizontal Axis Wind Turbine Blades," *J. Sol. Energy Eng.*, vol. 140, pp. 1–9, 2019.

[48] L. Prandtl and O. G. Tietjens, *Applied Hydro and Aeromechanics*. New York: Dover, 1957.

[49] A. M. Halawa, B. Elhadidi, and S. Yoshida, "Aerodynamic Performance Enhancement Using Active Flow Control on DU96-W-180 Wind Turbine Airfoil," *Evergr. Jt. J. Nov. Carbon Resour. Sci. Green Asia Strateg.*, vol. 5, no. 1, pp. 16–24, 2018, Accessed: Jan. 15, 2021. [Online]. Available: https://hdl.handle.net/10356/137681https://doi.org/10.5109/1929723

[50] M. H. Hansen, A. Hansen, T. J. Larsen, S. Øye, P. Sørensen, and P. Fuglsang, "Control Design for a Pitch-Regulated, Variable Speed Wind Turbine." R-15OO, Risø National Lab, Roskilde, Denmark, 2005. Accessed: Jan. 15, 2021. [Online].

Available: www.risoe.dk

[51] F. R. Menter, “Two-Equation Eddy-Viscosity Turbulence Models for Engineering Applications,” *AIAA*, vol. 32, no. 8, 1994.

[52] E. P. George, J. S. Hunter, W. G. Hunter, R. Bins, K. Kirlin IV, and D. Carol, “Fractional Factorial Designs,” in *Statistics for experimenters: design, innovation, and discovery*, 2nd ed., New York: Wiley, 2005.

[53] I. P. Gent and T. W. Alsh, “Towards an Understanding of Hill-climbing Procedures for SAT,” *AAAI*, vol. 93, pp. 28–33, 1993.

[54] D. Yuret and M. De La Maza, “Dynamic Hill Climbing: Overcoming the limitations of optimization techniques,” *Second Turkish Symp. Artif. Intell. Neural Networks*, pp. 208–212, 1993.

[55] M. Dorigo, M. Birattari, and S. Thomas, “Ant Colony Optimization,” *IEEE Comput. Intell. Mag.*, vol. 1, no. 4, pp. 28–39, 2006.

[56] M. Krstić and H. H. Wang, “Stability of Extremum Seeking Feedback for General Nonlinear Dynamic Systems,” *Automatica*, vol. 36, no. 4, pp. 595–601, 2000.

[57] H. Malek, S. Dadras, and Y. Q. Chen, “Performance analysis of fractional order extremum seeking control,” *ISA Trans.*, vol. 63, pp. 281–287, Jul. 2016.

[58] L. R. McKittrick, D. S. Cairns, J. Mandell, D. C. Combs, D. A. Rabern, and R. D. Van Luchene, “Analysis of a Composite Blade Design for the AOC 15/50 Wind Turbine Using a Finite Element Model,” Sandia National Laboratories Report, Albuquerque, 2001.

[59] B. Mohanty and K. A. Stelson, “Dynamics and Control of an Energy Efficient Power Regenerative Hydrostatic Wind Turbine Dynamometer,” *Energies*, vol. 15,

no. 8, 2022.

[60] B. Mohanty, F. Wang, and K. A. Stelson, “Design of a Power Regenerative Hydrostatic Wind Turbine Test Platform,” *JFPS Int. J. Fluid Power Syst.*, vol. 11, no. 3, pp. 130–135, 2019.

[61] T. Ackermann, *Wind Power in Power Systems*. John Wiley & Sons, 2005.

[62] W. W. E., “Rotary-Pump Theory,” *Trans. ASME*, vol. 68, no. 4, pp. 371–384, 1946.

[63] G. Reethof, *Characteristics of Postive Displacment Pumps and Motors*. Cambridge, MA: M.I.T Press, 1960.

[64] S. W. M. J., *Mathematical Model for Displacement Pumps and Motors*, vol. 7. 1961.

[65] D. McCandlish and R. E. Dorey, “The Mathematical Modelling of Hydrostatic Pumps and Motors,” *Proc. Inst. Mech. Eng. Part B Manag. Eng. Manuf.*, vol. 198, no. 3, pp. 165–174, Feb. 2006.

[66] K. A. Stelson and F. Wang, “A Simple Model of Piston-Cylinder Gap Efficiency in Positive-Displacement Hydraulic Pumps and Motors,” *Proc. 2010 ASME/Bath Symp. Fluid Power Motion Control*, pp. 437–449, 2010.

[67] G. F. Franklin, J. D. Powell, and A. Emami-Naeini, *Feedback Control of Dynamic Systems*, 8th ed. New Jersey: Prentice Hall, 2019.

[68] J.-J. E. Slotine and W. Li, *Applied Nonlinear Control*. New Jersey: Prentice-Hall, 1991.

[69] Hägglunds, “Compact CA Product Manual.” p. 23, 2011.

[70] International Organization for Standardization, “ISO 2909:2002. Petroleum

Products – Calculation of viscosity index from kinematic viscosity.” 2002.

[71] A. Vacca and G. Franzoni, *Hydraulic Fluid Power: Fundamentals, Applications, and Circuit Design*. New York: Wiley, 2021.

[72] J. D’Errico, “Noise Estimator.” MATLAB Central File Exchange, 2007. [Online]. Available: https://www.mathworks.com/matlabcentral/fileexchange/16683-estimatenoise

Appendices

a. MATLAB® Codes for Chapter 2

Two codes are presented for implementing the proposed ideas.

a.1. Blade Element Momentum Theory MATLAB® Code

The first code is for Blade Element Momentum Theory (BEMT). This code takes the airfoil's aerodynamic data and the geometry of the turbine blade to calculate BEMT for the static and dynamic cases, and finally, it calculates the power ratios.

```
%% Power calculation with BEM for DU96W180 Blade.m
close all; clear; clc;

%% Importing data
init = 1000;
% It changes the first point of data being analyzed
deg2rad = pi/180;
% Convertion factor from degrees to radians

% Blade characteristics
r = csvread('r_15.csv');
% Vector of the radius at each element of the blade
R = max(r);
% Radius of the blade
c = csvread('chord_15.csv');
% Chord c(r)
twist1 = csvread('twist_15.csv');
% Twist angle twist(r) in degrees
twist = deg2rad*twist1;
% Twist angle twist(r) in radians
CL = csvread('C_L_15.csv');
% Static Lift coefficient C_L(r)
CD = csvread('C_D_15.csv');
% Static Drag coefficient C_D(r)
a = csvread('a_15.csv');
% Axial induction factor a(r)
b = csvread('b_15.csv');
% Tangential induction factor b(r)
phiql = csvread('phi_15.csv');
% Angle of incidence phi(r) in degrees
phi = deg2rad*phiql;
% Angle of incidence phi(r) in radians
alpha1 = csvread('alpha_15.csv');
% Angle of attack alpha(r) in degrees
```

```
alpha = deg2rad*alpha1;
% Angle of attack alpha(r) in radians

U = 7;
% Air velocity m/s
B = 3;
% Number of blades
rho = 1.225;
% Air density Kg/m^3

omega_pow = csvread('power_rot_speed.csv');
omega_tot = omega_pow(:,1);
pow_tot = omega_pow(:,2);
TSR_Cp = csvread('c_p_TSR.csv');
TSR = TSR_Cp(:,2);
Cp_tot = TSR_Cp(:,2);

pow_qblade = max(pow_tot);
ind = find(pow_tot==pow_qblade);
omega = omega_tot(ind)*pi/30;       % Turbine rotational speed rad/s
Cp_qblade = max(Cp_tot);            % Max Cp turbine

% Importing static data
Qblade = csvread("Cl_Qblade.csv");
Qblade2 = csvread("Cd_Qblade1.csv");
AA = Qblade(10:end,1);
cL_15 = Qblade(10:end,2);
cD_15 = Qblade2(10:end,2);

% Importing dynamic data
f = 0.5;
w = 2*pi*f;

dyn = importdata('sine_0.5Hz_5.5deg_8deg_tilted_15m-s.out');
t_dyn = dyn.data(init:end,2);
AA_dyndeg = 8+(0.0901013*sin(w*t_dyn)+0.0225253*sin(2*w*t_dyn)+...
    0.00429054*sin(3*w*t_dyn)+0.000402238*sin(4*w*t_dyn))/deg2rad;
AA_dyn = AA_dyndeg*deg2rad;
CL_dyn = dyn.data(init:end,3);
CD_dyn = dyn.data(init:end,4);
CM_dyn =
dyn.data(init:end,5);

%% BEM Static
V0 = U*(1-a);               % Velocity component m/s
V2 = omega*r.*(1+b);        % Velocity component m/s
VLOCSQU = (V0.^2)+(V2.^2);  % Velocity squared m^2/s^2
PHI = atan2(V0,V2);         % Angle of incidence in rad
THETA = PHI+alpha;
pitch = THETA-twist;        % Static blade pitch angle in radians

K1 = 0.5*rho*B*c.*r;
DqDr = K1.*VLOCSQU.*(CL.*sin(PHI)-CD.*cos(PHI));    % Torque per
element

element = R/length(r);                              % Size of the
element
```

```
torque = sum(DqDr(1:end,:)*element);                % Total Torque
power = torque*omega;
Cp = power/(0.5*rho*U^3*pi*R^2);
percenterrorCp =100*abs(Cp-Cp_qblade)/Cp_qblade;

%% Torque per element static and dynamic
el = 21;                                            % Number of
elements

V01 = U*(1-a(el,1));
V21 = omega*r(el,1).*(1+b(el,1));
VLOCSQU1 = (V01.^2)+(V21.^2);
DqDr = 0.5*rho*3*r(el,1)*c(el,1).*VLOCSQU1*(CL(el,1)*sin(PHI(el,1))-...
    CD(el,1)*cos(PHI(el,1)));

DqDr_dyn = 0.5*rho*B*r(el,1)*c(el,1).*VLOCSQU1*(CL_dyn.*sin(PHI(el,1))-
...
    CD_dyn.*cos(PHI(el,1)));

q_stat = DqDr*element;
q_dyn = DqDr_dyn*element;

q_dyn_mean = mean(q_dyn);

%% Full blade Power calculations

for el = 1:length(r)

V01(el) = U*(1-a(el,1));
V21(el) = omega*r(el,1).*(1+b(el,1));
VLOCSQU1(el) = (V01(el).^2)+(V21(el).^2); % calculate velocity

M_dyn(:,el) = CM_dyn.*0.5*(rho*VLOCSQU1(el)*element*(c(el,1).^2));

DqDr_dyn(:,el) =
+0.5*rho*B*r(el,1)*c(el,1).*VLOCSQU1(el)*(CL_dyn.*sin(PHI(el,1))-...
    CD_dyn.*cos(PHI(el,1)));
end

q_dyn = DqDr_dyn*element;

net_q_dyn = sum((DqDr_dyn(:,1:end)*element),2);

power_dyn = net_q_dyn*omega;

extra_pow_dyn = sum(M_dyn(:,1:end),2)*w;

net_power_dyn = power_dyn-B*extra_pow_dyn;

torque_dyn_mean = mean(net_q_dyn);

power_dyn_mean = mean(net_power_dyn);

Cp_dyn = power_dyn_mean/(0.5*rho*U^3*pi*R^2);

Ratio = power_dyn_mean/power;
```

a.2. Hill-Climbing Optimization MATLAB® Code

The second code is for Hill-Climbing Optimization. This code takes the CFD-generated data and power ratio results and calculates the best conditions to be tested in CFD simulations. When the optimization is completed, it can be used to plot the final results to see the optimization path.

```
%% Hill Climbing Point by Point
clear all; close all; clc;
%%
csvread('data.csv');
vars = [7.75,1.4, 0.15;8.25,1.15,0.3;8.5,1,0.2;8,1.3,0.25];
num_sims = 4;
increase_dyn = [0.8387 0.8564 0.8711 0.8374];

for j = 1:num_sims
        if increase_dyn(j) == min(increase_dyn)
            min_pos = j;
            break;
        end
    end

    if min_pos == 1
        vars2 = vars(2:4,:);
    else
        vars2 = [vars(1:min_pos-1,:); vars(min_pos+1:4,:)];
    end
    centroid = [mean(vars2(:,1)), mean(vars2(:,2)), mean(vars2(:,3))];
    new_point = [centroid(1) - (vars(min_pos,1) - centroid(1)),...
                 centroid(2) - (vars(min_pos,2) - centroid(2)),...
                 centroid(3) - (vars(min_pos,3) - centroid(3))];

%% Plotting results
data = csvread('data.csv');
Xini1 = data([1,4],2);Yini1 = data([1,4],3);Zini1 = data([1,4],4);
Xini2 = data([2,3],2);Yini2 = data([2,3],3);Zini2 = data([2,3],4);
Xini3 = data([1,3],2);Yini3 = data([1,3],3);Zini3 = data([1,3],4);
Xini4 = data([2,4],2);Yini4 = data([2,4],3);Zini4 = data([2,4],4);
xlab = data(:,2);ylab = data(:,3);zlab = data(:,4);

X = data(5:end-1,2);
Y = data(5:end-1,3);
Z = data(5:end-1,4);

ind = find(data(:,5)==max(data(:,5)));
Xfin = data(ind,2);
Yfin = data(ind,3);
Zfin = data(ind,4);

cX = centroid(1);
cY = centroid(2);
cZ = centroid(3);
```

```
figure
plot3(X,Y,Z,'ks-','Linewidth',1.5); hold on;grid on;
plot3(Xini1,Yini1,Zini1,'rd--',...
    'MarkerFaceColor','red','markersize', 8)
ylabel('A (^o)')
xlabel('Avg Angle of Attack (^o)')
zlabel('f (Hz)')
xlim([7.5,10])
ylim([0.2, 1.4])
zlim([0,0.35])
plot3(Xini2,Yini2,Zini2,'rd--',...
    'MarkerFaceColor','red','markersize', 8)
plot3(Xini3,Yini3,Zini3,'rd--',...
    'MarkerFaceColor','red','markersize', 8)
plot3(Xini4,Yini4,Zini4,'rd--',...
    'MarkerFaceColor','red','markersize', 8)

plot3(Xfin,Yfin,Zfin,'p','MarkerEdgeColor',[0 .7 .2],...
    'MarkerFaceColor',[0 .7 .2],'markersize', 20)

plot3(cX,cY,cZ,'bo')

plot3([cX,X(1)],[cY,Y(1)],[cZ,Z(1)],'b:')

text(Xini4(1),Yini4(1),Zini4(1)+Zini4(1)*0.15,'Initial
Points','Fontweight','bold','color','r')
text(Xfin+Xfin*0.02,Yfin-Yfin*0.02,Zfin-Zfin*0.025,'Highest Power
Ratio','Fontweight','bold','color',[0 .7 .2])
text(8.75,0.38,Zfin-Zfin*0.025,'0.8977','Fontweight','bold','color',[0
.7 .2])
text(cX-cX*0.1,cY,cZ+cZ*0.2,'Centroid
\rightarrow','Fontweight','bold','color','b')
text(X(2),Y(2)+Y(2)*0.15,Z(2)+Z(2)*0.05,'Optimization
path','Fontweight','bold','color','k')
```

b. MATLAB® Codes for Chapter 4

Two codes are presented for implementing the proposed ideas.

b.1. Parameter Fitting MATLAB® Code

This code takes experimental efficiency data and fits it into the simplified efficiency model to obtain the nondimensional pump and motor factors.

```
%% Parameter Finding
clear;close all;clc;

%% Data
datap=xlsread('PumpEffCharHSD_modif1.xlsx');
data=xlsread('MotorEffCharHSD_modif1.xlsx');
% efficiencies = load('Efficiencies_HSD.mat');
%% Knowns Motor
```

```
%dimensionless viscosity
mu=data(:,1)'; % viscosity (Pa*s)
p=100000.*data(:,2)'; % pressure (Pa)
omega=data(:,3)'./2./pi; % speed [rad/s]

%dimensionless displacement
f=data(:,4)'; %(0-1) 1 being max displacement

%Output
eta=data(:,5)'; %Overall Efficiency [-]
% nt=data(:,6)'; %Mechanical Efficiency
% nq=data(:,7)'; %Volumetric Efficiency

%Input
mu=mu.*omega./p;

%% Knowns Pump
%dimensionless viscosity
mup=datap(:,1)'; % viscosity (Pa*s)(0.068/0.056).*
pp=100000.*datap(:,2)'; % pressure (Pa)
omegap=datap(:,3)'./2./pi; % speed [rad/s]

%dimensionless displacement
fp=datap(:,4)'; %(0-1) 1 being max displacement

%Output
etap=datap(:,5)'; %Overall Efficiency [-]

%Input
mup=mup.*omegap./pp;
%% Fit: 'Motor Efficiency'.
[xData, yData] = prepareCurveData( mu,eta );

% Set up fittype and options.
ft = fittype( '(1-
(4*(1/d)*(1/D^2)*mu))/(1+((1/3)*(d^3)*(D^2)*(1/mu)))', 'independent',
'mu', 'dependent', 'eta' );
opts = fitoptions( 'Method', 'NonlinearLeastSquares' );
opts.Display = 'Off';
opts.MaxFunEvals = 5000;
opts.MaxIter = 5000;
opts.Robust = 'LAR';
opts.StartPoint = [0.3 0.1];

% Fit model to data.
[fitresult, gof] = fit( xData, yData, ft, opts );

% Plot fit with data.
figure( 'Name', 'Motor Efficiency' );
h = plot(fitresult,'b-', xData, yData,'ko');
legend( h, 'Motor Efficiency', 'Fit', 'Location', 'NorthEast',
'Interpreter', 'none' );
% Label axes
xlabel( '$\hat{\mu}$','interpreter','latex');
% ylabel( 'f', 'Interpreter', 'none' );
ylabel( '\eta');
ylim([0.85,1])
```

```
grid on
rsquare_m = gof.rsquare;
rmse_m = gof.rmse;
D_m = fitresult.D;
d_m = fitresult.d;
%% Fit: 'Pump Efficiency'.
[xData, yData, zData] = prepareSurfaceData( mup, fp, etap );

% Set up fittype and options.
ft = fittype( '(1-
(((dp^3)*(Dp^2))/(3*fp*mup)))/(1+(4*mup/(dp*(Dp^2)*fp)))',
'independent', {'mup', 'fp'}, 'dependent', 'etap' );
opts = fitoptions( 'Method', 'NonlinearLeastSquares' );
opts.Display = 'Off';
opts.MaxFunEvals = 5000;
opts.MaxIter = 5000;
opts.Robust = 'LAR';
opts.StartPoint = [0.2 0.1];

% Fit model to data.
[fitresultp, gofp] = fit( [xData, yData], zData, ft, opts );

% Plot fit with data.
figure( 'Name', 'Pump Efficiency' );
h = plot( fitresultp,[xData, yData], zData );
legend( h, 'Pump Efficiency', 'Fit', 'Location', 'NorthEast',
'Interpreter', 'none' );
% Label axes
xlabel( '$\hat{\mu}$','interpreter','latex');
ylabel( 'f' );
zlabel( '\eta' );
grid on
rsquare_p = gofp.rsquare;
rmse_p = gofp.rmse;
D_p = fitresultp.Dp;
d_p = fitresultp.dp;

save('Geometry_Parameters','D_p','d_p','D_m','d_m','gofp','gof')
```

b.2. Covariance Calculations for Kalman Filter MATLAB® Code

This code takes experimental data and calculates the covariance that can be used later to find the Kalman Filter coefficients. This is a code written by [72].

```
function noisevar = estimatenoise(X,varargin)
% estimatenoise: additive noise estimation from a time series
% usage: noisevar = estimatenoise(X)
%
% Author: John D'Errico
% e-mail: woodchips@rochester.rr.com
% Release: 2.0
% Release date: 8/25/07
% if no input arguments provided, just dump out the help
```

```
if nargin<1
  help estimatenoise
  return
end
% complex sequences are split into real and imaginary parts.
if ~isreal(X)
  noisevar = estimatenoise(real(X)) + estimatenoise(imag(X));
  return
end
% get the size of X, so we can pick the value for
% dim if it was not supplied. We will also need to
% make sure the length in that dimension is large
% enough.
sx = size(X);
% were t and/or dim supplied? In which order?
if (nargin>3)
  error('Too many inputs supplied. Maximum of 3 inputs are allowed.')
elseif nargin == 1
  % use defaults
  dim = [];
  t = [];
elseif (nargin == 2) && isempty(varargin{1})
  % use defaults
  dim = [];
  t = [];
elseif (nargin==2) && (length(varargin{1}) == 1)
  % dim was supplied
  dim = varargin{1};
  t = [];
elseif (nargin==2)
  % t must have been specified
  t = varargin{1};
  t = t(:);
  dim = [];
elseif (nargin==3) && (length(varargin{1}) == 1)
  % dim and t were supplied, in that order
  dim = varargin{1};
  t = varargin{2};
  t = t(:);
elseif (nargin==3) && (length(varargin{2}) == 1)
  % t and dim were supplied, in that order
  dim = varargin{2};
  t = varargin{1};
  t = t(:);
else
  % there is a problem with the arguments
  error('A and t arguments are of inconsistent size')
end
% get dim if it was not supplied
if isempty(dim)
  dim = find(sx~=1,1,'first');
  if isempty(dim)
    error('X did not have at least one dimension of length >1')
  end
end
% check the length in the dim dimension
nX = sx(dim);
```

```
if nX<5
  error('The length of X in the specified dimension was less than 5')
end
% permute the dimensions so that the chosen dimension
% of X is moved to the end of the line.
ndim = length(sx);
nx = 1:ndim;
nx(dim) = [];
nx = [nx,dim];
Xp = permute(X,nx);
% then just reshape it to be a 2-d array
Xp = reshape(Xp,[],sx(dim));
% was t actually equally spaced anyway? If it was, then we
% want to use the equal spaced code.
equispaced = true;
if ~isempty(t)
  % first sort t, just in case
  [t,tags] = sort(t);
  % and shuffle Xp in the first dimension
  Xp = Xp(:,tags);

  % check for equal spacing in t
  dt = diff(t);

  % average spacing
  avespace = (t(end) - t(1))/(nX-1);
  if (avespace == 0)
    error('Invalid t vector: t was identically zero.')
  end
  tol = 10*eps(avespace);
  if tol < (max(dt) - min(dt))
    % unequal spacing
    equispaced = false;
  end
end
% estimate the measurement variability in the (now) second dimension
% later we will undo this reshape.
% The idea here is to form a linear combination of successive elements
% of the series. If the underlying form is locally nearly linear, then
% a [1 -2 1] combination (for equally spaced data) will leave only
% the noise remaining. Next, if we assume the measurement noise was
% iid, N(0,s^2), then we can try to back out the noise variance.
fda{1} = [1 -1];
fda{2} = [1 -2 1];
fda{3} = [1 -3 3 -1];
fda{4} = [1 -4 6 -4 1];
fda{5} = [1 -5 10 -10 5 -1];
fda{6} = [1 -6 15 -20 15 -6 1];
nfda = length(fda);
for i = 1:nfda
  % normalize to unit norm
  fda{i} = fda{i}/norm(fda{i});
end
% compute an interquantile range, like the distance between the 25%
% and 75% points. This trims off the trash at each end, potentially
% corrupted if there are discontinuities in the curve. It also deals
% simply with a non-zero mean in this data. Actually do this for
```

```
% several different interquantile ranges, then take a median.
% NOTE: While I could have used other methods for the final variance
% estimation, this method was chosen to avoid outlier issues when
% the curve may have isolated discontinuities in function value or
% a derivative.
% The following points correspond to the central 90, 80, 75, 70, 65,
% 60, 55, 50, 45, 40, 35, 30, 25, and 20 percent ranges.
perc = [0.05, 0.1:0.025:0.40];
z = erfinv((1-perc)*2-1)*sqrt(2);
sigmaest = nan(size(Xp,1),nfda);
for i = 1:nfda
  % Apply each difference to the data series with convn
  % the 'valid' option will trim off the junk at the ends
  % from the convolution.

  % did we have equal spacing?
  if equispaced
    % If so, then conv will do the trick.

    % These convolutions will yield noise of the desired variance,
    % although it will be colored noise.
    noisedata = conv2(Xp,fda{i},'valid');
    ntrim = size(noisedata,2);
  else
    % unequal spacing. do it the hard way
    F = 1./gamma(1:i);
    ntrim = nX - i;
    noisedata = zeros(size(Xp,1),ntrim);
    for j = 1:ntrim
      tj = t(j+(0:i));
      tj = tj - mean(tj);
      if all(abs(tj) <= tol)
        % be careful if all points were reps!
        coef = rem((0:i)',2)*2-1;
        coef = coef - mean(coef);
        % and normalize
        coef = coef/norm(coef);
      else
        % use null to choose the linear combination
        % of the elements of Xp.
        tj = tj/norm(tj);
        A = repmat(tj,1,i).^repmat(0:(i-1),i+1,1);
        A = A.*repmat(F,i+1,1);
        nullvecs = null(A');
        % already normalized to have unit norm by null
        coef = nullvecs(:,1);
      end

      % form the appropriate linear combination of Xp
      noisedata(:,j) = Xp(:,j+(0:i))*coef;
    end
  end  % if equispaced

  % were there enough points to even try anything?
  if ntrim >= 2
    % sorting will provide the necessary percentiles after
    % interpolation.
```

```
    noisedata = sort(noisedata,2);

    p = 0.5 + (1:ntrim)';
    p = p/(ntrim + 0.5);

    Q = zeros(size(noisedata,1),length(perc));
    for j = 1:length(perc)
      Qj = interp1q(p,noisedata',1-perc(j)) -
interp1q(p,noisedata',perc(j));
      Qj = Qj/(2*z(j));
      Q(:,j) = Qj';
    end
    % Trim off any nans first, since if the series was short enough,
    % some of those percentiles were not present.
    wasnan = isnan(Q(1,:));
    Q(:,wasnan) = [];

    % Our noise std estimate is given by the median of the
interquantile
    % range(s). This is an ad hoc, but hopefully effective, way of
    % estimating the measurement noise present in the signal.
    sigmaest(:,i) = median(Q,2);

  end

end % for i = 1:nfda
% drop those estimates which failed for lack of enough data
sigmaest(:,isnan(sigmaest(1,:))) = [];
% use median of these estimates to get a noise estimate.
noisevar = median(sigmaest,2).^2;
% Use an adhoc correction to remove the bias in the noise estimate.
% This correction was determined by examination of a large number of
% random samples.
noisevar = noisevar/(1+15*(sx(dim)+1.225)^-1.245);
% The first order difference might be used to guesstimate the
% process noise.
% if nargout>1
%   processvar = max(0,sigmaest(:,1).^2 - noisevar);
% end
% finally, reshape the result to be consistent with the input shape
sx(dim) = 1;
noisevar = reshape(noisevar,sx);
```